# ATTITUDE CONTROL HARDWARE AND SOFTWARE FOR NANOSATELLITES

by

Pawel Grzegorz Lukaszynski

A thesis submitted in conformity with the requirements
for the degree of Master of Applied Science

Graduate Department of Aerospace Engineering
University of Toronto

# Abstract

Attitude Control Hardware and Software for Nanosatellites

Pawel Grzegorz Lukaszynski
Master of Applied Science
Graduate Department of Aerospace Engineering
University of Toronto
2013

The analysis, verification and emulation of attitude control hardware for nanosatellite spacecraft is described. The overall focus is on hardware that pertains to a multitude of missions currently under development at the University of Toronto Institute for Aerospace Studies - Space Flight Laboratory. The requirements for these missions push the boundaries of what is currently the accepted performance level of attitude control hardware. These new performance envelopes demand new acceptance test methods which must verify the performance of the attitude control hardware. In particular, reaction wheel and hysteresis rod actuators are the focus. Results of acceptance testing are further employed in post spacecraft integration for hardware emulation. This provides for a reduced mission cost as a function of reduced spare hardware. The overall approach provides a method of acceptance testing to new performance envelopes with the benefit of cost reduction with hardware emulation for simulations during post integration.

# Dedication

To my Grandfather who had always been there for me, and whom will always be remembered; to my Mom, for the support and guidance; to my brother, the insight and inspiration; to my Grandmother, for her wisdom. You have all been a part of my journey and I am forever thankful.

*Consilio et animis.*

# Acknowledgments

# Table of Contents

# List of Tables

# List of Figures

# Chapter 1

# Introduction

The growing demand for lower cost nanosatellites missions and their expected performance has attracted a viable customer base which today includes academia and the space industry. The focus is on attaining higher performance at a lower cost through the use of Commercial Off-The-Shelf (COTS) technology [1]. Through practice, this approach has attracted a multitude of nanosatellites missions that are currently under commission at the University of Toronto Institute for Aerospace Studies Space Flight Laboratory (*UTIAS/SFL*). These missions include Nanosatellite for Earth Monitoring and Observation (NEMO-AM and NEMO-HD), Canadian Advanced Nanospace eXperiment − 4 and 5 (CanX-4&5), BRIght Target Explorer − Constellation (BRITE-Constellation) and AISSat-2, for which the analysis, verification and emulation of attitude control hardware is presented.

## 1.1 Background

Each of the aforementioned missions has an objective from which system requirements are derived. The objective of NEMO-AM is aerosol monitoring through the use of a multispectral optical instrument [2]. The objective of NEMO-HD is high definition multispectral imaging with pan sharpening along with video capability. The objective of the (CanX-4 & 5) is to demonstrate autonomous formation flight of two nanosatellites [3]. While the objective of the BRITE-Constellation is to provide photometrical measurement of low-level oscillations and temperature variations in stars utilizing six nanosatellites [4]. Finally the objective of AISSat-2 which is a successor to AISSat-1 is to perform maritime vessel monitoring in the Norwegian waters using a Kongsberg Seatex AIS (Automatic Identification System) receiver [5]. All mentioned missions have respective requirements which based on the nanosatellites

size are considered to be high performance and place inherent constraints on the attitude control system.

Hence, the analysis of performance and verification of requirements through acceptance testing of flight hardware is of great importance for the success of these missions. This process begins with the high level system requirements being translated into subsystem requirements through the use of MIRAGE, a high fidelity attitude determination and control system simulator. The output of which provides the requirements that attitude control hardware can be verified against. The performance of the attitude control hardware is then analyzed and verified against the subsystem requirements through the process of acceptance testing. Pending the outcome of verification, the acceptance testing method is revised such that requirements are verified or different hardware needs to be chosen. Post analysis and verification, the attitude control hardware can be integrated into the spacecraft bus. Typically spare hardware is used from this point on in what is termed FlatSat for further hardware testing. The FlatSat is essentially a flat layout of all hardware that will be or was integrated into a spacecraft. This can be composed of spare hardware which typically adds to the cost of a mission but provides an invaluable resource which can allow for further hardware testing.

The hardware emulation is one method of reducing the number of spare hardware and hence reducing the mission cost. This can be accomplished through software modeling of the hardware and usage of the acceptance test data to provide the specific characteristic response of the required hardware. In all, the analysis and verification validate the hardware for the missions and hardware emulation adds the benefit of cost reduction.

## 1.2 Overview of Nanosatellite Technology

The typical spacecraft is composed of a multitude of systems which enable it to perform its function. Each system can break down further into a subsystem or a final hardware/software component. The following subsystems typically exist [6]:

1. Attitude Determination and Control
2. Telemetry, Tracking and Command
3. Command and Data Handling
4. Power
5. Thermal
6. Structures and Mechanisms

7.  Guidance and Navigation

8.  Payload

At the nanosatellite scale the mentioned systems and their inherent required technologies can be a challenge to implement due to mass, size and power availability limitations.  To mediate these challenges the Space Flight Laboratory has developed the Generic Nanosatellite Bus *(GNB)*.  This spacecraft bus is a modular and versatile satellite platform capable of carrying standard suite of flight hardware with adequate volume and mass margin for a science payload.  The GNB bus draws upon proven and robust flight heritage from earlier technology readiness missions such as the CANX-2. The general dimensions of the GNB are $20cm$ by $20cm$ by $20cm$ cube with a weight of $7kg$ [4].  These mass and volumetric limitations place the GNB in the nanosatellite category.  The bus is divided into 3 layers each layer being approximately $6.5cm$ by $20cm$ by $20cm$ [7].  The science payload is sandwiched between the top and bottom layer providing access to four sides of the satellite bus.  Typically the available mass for a science payload can be one third of $7kg$ or more pending mass margins in the mass budget.    The standard suite of attitude flight hardware consists of magnetometers, rate sensors, sun sensors, star trackers, reaction wheels and magnetorquers.  Some hardware maybe excluded pending mission requirements [7]. Refer to Figure 1-1 for a visual representation of the typical composition of the GNB technology.

As an example for the CANX-4 & 5 mission which is based on the GNB bus, the science payload will be a Canadian Nano-satellite Advanced Propulsion System *(CNAPS)* [3].  This propulsion system will provide the on-orbit translational motion and hence be the actuation method that maintains relative distance between the two nanosatellites.  The CNAPS will rely on the attitude control hardware and software to provide large torques of up to $400\mu Nm$ [8] in short time frames such that CNAPS can be actuated in time.

The BRITE-Constellation mission, also using the GNB bus, will carry a small aperture telescope as its science payload [4].  The requirement on flight hardware is to provide arc-minute pointing accuracy for the science payload with a maximum 1-sigma torque control ripple of $1 \times 10^{-6} \, Nm$ at a reaction wheel speed of $100 \, rad/s$ [8].

Although current acceptance testing of attitude control and determination hardware has satisfied requirements on previous missions, this however does not mean that the

test will satisfy requirements on new missions. As such, great care is taken to review the requirements and how the acceptance testing will verify these requirements. More specifically the acceptance testing of reaction wheels and hysteresis rods is reviewed and verified in this thesis. All the described missions utilize a variation of attitude hardware; but typically three reaction wheels are used on each spacecraft. Hysteresis rods on the other hand are used in passive attitude control and typically are not used in combination with reaction wheels. Also, reaction wheels can provide fine pointing whereas the passive magnetic approach can only provide coarse pointing at best. This is important since pointing accuracy on a spacecraft is requirement driven and is a decisive metric in the choice of attitude control hardware. Both attitude control methods have been previously used in the GNB spacecraft bus with flight heritage. The difference in performance between the active attitude control and passive is further described in Chapter 2.

## 1.3   Typical Nanosatellite Spacecraft Composition

The Generic Nanosatellite Bus (GNB) is shown in Figure 1-1 identifying the typical spacecraft composition. Each spacecraft subsystem is incorporated into its unique physical footprint. In a typical design certain subsystem components can be omitted pending requirements.
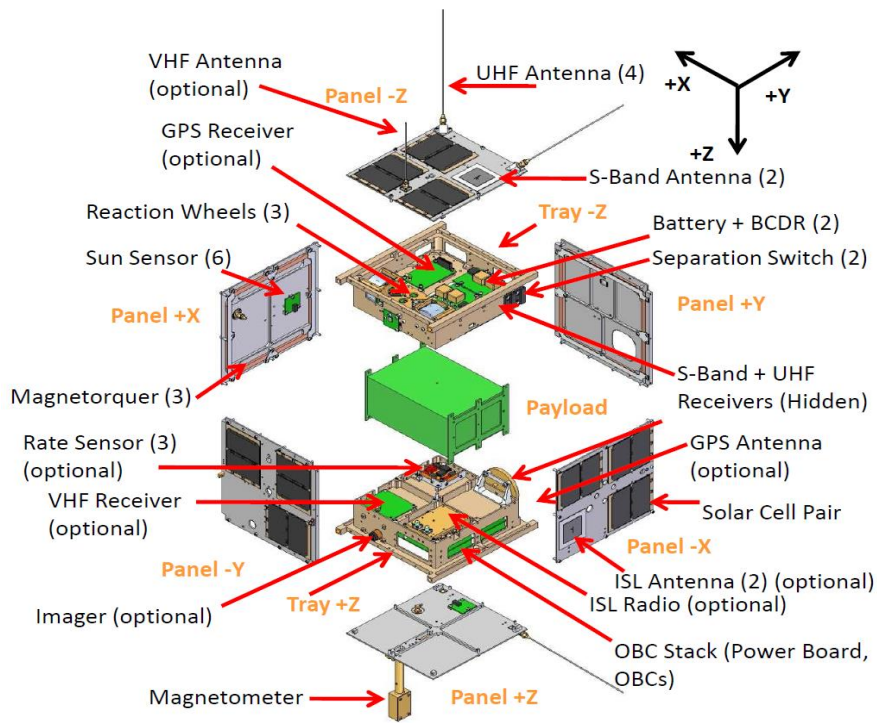


Figure 1-1: Generic Nanosatellite Bus (GNB) Layout

## 1.4   Significance of Attitude Control System

The attitude and determination control system is what makes the knowledge and manipulation of the rotational motion of a spacecraft possible. This system determines the spacecraft orientation in relation to an object and then is able to control or change its orientation with respect to that same object. This can be used for high gain antenna pointing and target tracking as an example. The system can be further divided into the attitude control and attitude determination systems. It is the attitude control system of a spacecraft that is the focus of the authors work. This system is predominantly responsible for actuation or the ability to generate a torque in response to a required attitude orientation change request. The capability of the system and availability are based on flight heritage of the attitude control system hardware and software.

There is a precedent that has been set by earlier missions such as the CanX-2 which has shown some expected performance characteristics of flight hardware [4]. Although this does validate some performance characteristics it does not validate the performance to new and more stringent levels. Current missions have requirements that require fine pointing which has not been required on any previous SFL mission. This requirement on a reaction wheel actuator identifies a torque response that the wheel must attain which is comprised of a torque jitter and torque bias at a particular rotational speed [9]. As for a hysteresis rod, the typical characterization result is the amount of magnetic flux density as a function of magnetic field input that the rod can generate. The change of the input results in damping or removal of rotational energy from a spacecraft. Both control actuators need to be verified against subsystem requirements. This is a crucial step in ensuring the success of current and future missions that require new and higher performance envelopes of attitude control hardware.

As an example both missions, the CANX4&5 and BRITE-Constellation, are based on the GNB bus which has drawn upon its proven and robust flight heritage from earlier technology readiness missions such as the CANX-2. With the exception of difference in payload both missions will utilize attitude control hardware and software as previously used on the GNB but now acceptance tested for new and more rigorous requirements. For CANX-4&5 this means that attitude hardware and software will be capable of making rapid attitude changes such that formation flight can be maintained within the performance envelope. Whereas the BRITE-Constellation will require arc-minute pointing accuracy such that the science mission requirements are satisfied.

As such, the verification of subsystem requirements by the attitude control hardware acceptance testing is the single most important source of focus for the work described in this thesis. Previous work has shown that improvements had to be made to the Test Plan Procedure Analysis and Results (TPPAR) acceptance testing such that subsystem requirements have been met [5]. TPPAR is a standard acceptance testing document at SFL that describes the procedure and verification method of flight hardware performance.

## 1.5   Literature Review

The review of literature has shown that high performance and low cost capabilities of nanosatellites are reshaping the satellite industry. The Air Force Research Laboratory (AFRL) has with great success developed a rapid and scalable deployment of modular nanosatellites. The result is modularity with software and hardware, and the added capability of 'black-box' assembly of a bare nanosatellite within hours [10]. The design provides a fully functional spacecraft with payload capabilities. Surrey Satellite Technology Ltd (SSTL) of Surrey, a UK leader in microsatellites and minisatellites has also been working with their Commercial Off-The-Shelf (COTS) technology since 1980's [1]. It is also shown by Kayser-Threde GmbH [11] that the major limitations of small satellites are governed by physical limitations, where technology may not be available to perform mission objectives of larger satellites. The focus of the international community has been on breaking down technological boundaries [12] by developing small satellite technologies.

The attitude control hardware and software has inherently had limitations on the nanosatellite scale that needed to be overcome. Bingquan Wang of Tsnighua University in China [13] has developed a variable structure controller for reaction wheels that reduces the attitude error $10:1$ when compared to a PID controller. F. Landis Markley of Goddard Space Flight Centre [14] has developed a set of algorithms that model an n-dimensional hypercube (n-wheels). The result of the model shows that 6 reaction wheels can provide a benefit of reducing 25% of maximum wheel momentum or 30% in slew time. Reaction wheel disturbances on spacecraft due to application of torque have been analyzed by Hwa-Suk Oh [15], where the results have shown that acceptance testing and proper modeling of a reaction wheel can provide for better on-spacecraft performance. M. C. Chou [16] was able to improve torque generating capability and power consumption through the use of a varying frequency

current tracking controller under sinusoidal back electromotive force (EMF) disturbance. The current reaction wheels utilized by Space Flight Laboratory utilize a current tracking controller with a back EMF power estimation scheme to improve torque ripple down to $0.5 \times 10^{-6} Nm$ [17].

This review shows methods that had been proposed by others and some are included and developed further in the Test Plan Procedure Analysis and Results (TPPAR) acceptance testing that was conducted. The overall challenge is to not only push the current attitude control hardware to new higher performance levels, but also to ensure that the new performance envelopes do not introduce undesirable effects.

## 1.6 Scope

The work presented in this thesis describes the attitude control system with focus on the reaction wheel actuator and hysteresis rods. The work is extended to the emulation of attitude control hardware in software. A generalized preface is provided to attitude control hardware and what is currently available (Chapter 2) with emphasis on critical performance metrics. The reaction wheel actuator is described from theoretical brushless DC motor design to application and requirement verification (Chapter 3). The hysteresis rod is shown from material selection to an iterative design approach for a specific spacecraft bus with test fixture design and requirement verification (Chapter 4). Then an actuator and a sensor are combined in an emulation environment where their hardware characteristic responses are emulated in software for the purposes of reduced mission cost and post launch analysis capabilities (Chapter 5). Concluding remarks are provided with emphasis on current and future work that has resulted from this thesis (Chapter 6) and how this impacts the attitude control system. The overall emphasis is on analysis, verification of performance against subsystem requirements.

# Chapter 2

# Attitude Control System

In the early days of spacecraft design the attitude control and determination system was a very rudimentary system with no active control [18]. This meant that on a typical mission the form of control was always passive. The design process was to ensure that given the disturbance torques a spacecraft will encounter, it will always stabilize in a certain orientation. This approach worked but was not sufficient to mitigate high pointing requirements or complexities of new missions. Hence the attitude control was developed with an active component. This allowed higher pointing accuracy but also created the added complexity with respect to coupling between spacecraft systems. This complexity had arisen from the fact that the spacecraft could now be pointed with accuracy in any orientation. Systems such as power, navigation, communication and propulsion can affect or be directly affected by the performance of the active attitude control and determination system. Through this added system complexity and pointing requirements it is clear that this system is of great importance for the success of a mission.

The attitude control system provides the necessary torques as to stabilize the spacecraft in a desired orientation. The control authority that this system can provide is typically sized to overcome any disturbances and coupled with the attitude determination system can provide a required pointing accuracy [6]. The attitude determination system provides the state vector of the spacecraft orientation. This can be accomplished through a number of methods, some involving the use of sensors and a Kalman filter [19]. The attitude determination system will not be explored further and is beyond the scope of this thesis.

This chapter will focus on the background of the attitude control system (ACS) with emphasis on the type of hardware that will be presented in later chapters with

more detail. Coupling between spacecraft systems and parameters that are critical for the attitude control system will also be presented as shown in Figure 2-1 [6].

**Mission**

- Earth-Pointing or Inertial Pointing
- Control during $\Delta$V burns
- Accuracy/Stability needs
- Slewing requirements
- Orbit, Autonomy, Mission life, Onboard data requirement

**Propulsion**

- Thruster size
- Propellant load
- Minimum impulse bit

**Power**

- ACS Load
- Special regulation
- Solar array pointing

**Attitude Control System**

- 3-Axis stabilized
- Actuation device selection
- Computational architecture

**Communications**

- Antenna pointing accuracy

**Thermal**

- Special thermal maneuvers

**Structures**

- Centre of mass constraints
- Inertia constraints
- Flexibility constraints
- Thruster location
- Sensor mounting

Figure 2-1: Impact on ACS from System Coupling [6]

## 2.1   Overview of Attitude Control Hardware

The type of attitude control hardware chosen for a particular nanosatellite mission is always a function of the derived subsystem hardware requirements. Although these requirements are instrumental in the design process it is also as important to review bottom-up requirements in terms of what hardware is available and whether it can be utilized for a particular mission. An example of this process is having a particular derived subsystem requirement of torque for a reaction wheel and instead of designing a new reaction wheel using what is already designed and available. This provides a cost reduction but requires careful analysis during hardware acceptance testing such that requirements are satisfied.

To begin the review of the type of control hardware that is available it is important to review how a typical spacecraft control loop is defined and how the system breaks down into its basic components. A simplified block diagram of the attitude determination and control system (ADCS) control loop can be shown by Figure 2-2 [19]. The attitude control system (ACS) is primarily responsible for applying a control torque $T_c$ in response to a disturbance torque $T_D$ which is the induced error provided by the attitude determination system (ADS) [19]. The ACS system design is further divided into attitude stabilization requirements or torque jitter and attitude maneuver control. The second of which pertains to available control authority, overshoot and settling time of control hardware output. These will be verified against requirements with emphasis on some of the performance metrics in Chapter 3, which will provide the details of reaction wheel acceptance testing.
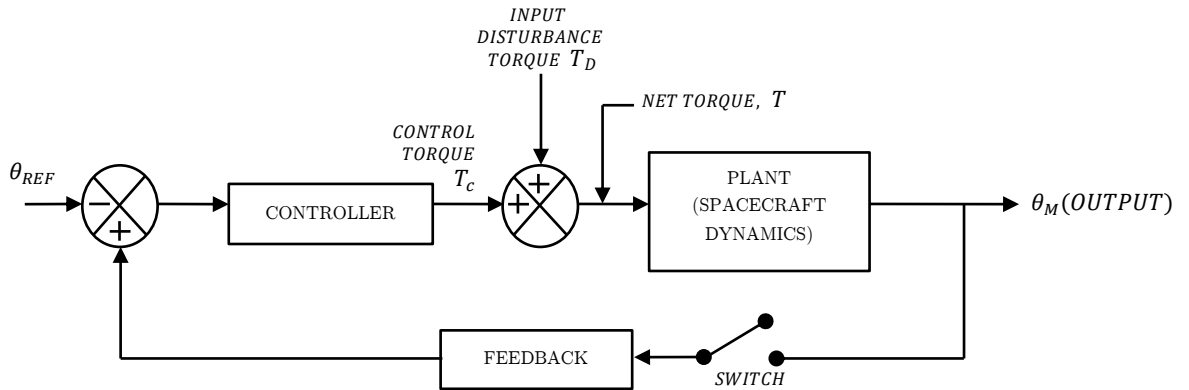


Figure 2-2: Typical Spacecraft Attitude Feedback Control System [19]

It should be noted that the attitude stabilization and maneuver control are performance metrics driven by subsystem requirements that can originate from other system requirements. For example, the power system may require solar array pointing, the thermal system may require special maneuvers to maintain the spacecraft thermal profile, the structure will impose inertia errors and mounting errors of all spacecraft hardware and the payload system may require specific torque jitter requirements for pointing [6]. These and many more constraints that can be placed on the attitude control system which must be captured by its control hardware.

The hardware introduced in this chapter is divided into active and passive control schemes. The active hardware consists of reaction wheel, magnetorquer and thrusters. The passive hardware is a choice of a combination of permanent magnet and hysteresis rods. Of the hardware mentioned the reaction wheel and the hysteresis rod are further analyzed in detail through acceptance testing in Chapter 3 and Chapter 4. The high-level background of attitude control dynamics is presented next to show how the control torques and disturbance torques combine in the spacecraft dynamics.

## 2.2 Spacecraft Attitude Control Dynamics

The spacecraft attitude control dynamics can be described using Euler's equation (2.1) with the assumption of a rigid spacecraft body under the influence of an external torque. Although no general solution exists for an arbitrarily specified torque, specific case scenario solutions can be attained through computer simulations as is typically done [20]. Hence, given a particular disturbance torque, angular rotations and inertia matrix the rate of change of a rigid body angular momentum vector can be determined. This is used extensively in simulations to show how the behavior of the spacecraft angular momentum changes given the external torques it is subjected to. It should be noted that on orbit the change in angular momentum is never zero due to disturbance torques. Examples of possible disturbance torques and what hardware the spacecraft can use to apply torques are described later in this Chapter. In general, the torque is mitigated through the spacecraft attitude control system, which is always balancing the described equation through its control torques. If it is assumed that the disturbance torques are zero than the angular momentum is conserved and its constant for the spacecraft with zero rate of change. This is described by:

$$\left(\frac{d\boldsymbol{H}}{dt}\right)_{body} = \boldsymbol{T} - \boldsymbol{\omega} \times \boldsymbol{I}\boldsymbol{\omega} \tag{2.1}$$

where $\boldsymbol{H}$ = Angular momentum vector

$\boldsymbol{I}$ = Spacecraft inertia matrix

$\boldsymbol{\omega}$ = Angular rotation matrix.

The expansion of Euler's equation into component form is shown in equations (2.2). This provides further insight into how the rate of change of angular momentum is influenced by the spacecraft mass moment of inertia, external torque and angular rotation. Hence, Euler's equation in component form becomes:

$$\dot{H}_1 = I_1\dot{\omega}_1 = T_1 + (I_2 - I_3)\omega_2\omega_3$$

$$\dot{H}_2 = I_2\dot{\omega}_2 = T_2 + (I_3 - I_1)\omega_3\omega_1 \tag{2.2}$$

$$\dot{H}_3 = I_3\dot{\omega}_3 = T_3 + (I_1 - I_2)\omega_1\omega_2$$

As an example, the coupling of an external torque can be described by equations (2.3) and (2.4). When expressed in the spacecraft body frame the equations that describe a single external wheel coupling are [18]:

$$\boldsymbol{H} = \boldsymbol{c}^\times \boldsymbol{v} + \boldsymbol{J}\boldsymbol{\omega} + \boldsymbol{a}I_w\omega_w \tag{2.3}$$

$$H_w = I_w\boldsymbol{a}^T\boldsymbol{\omega} + I_w\omega_w \tag{2.4}$$

where $\boldsymbol{c}$ = First moment of inertia

$\boldsymbol{v}$ = Absolute velocity of spacecraft in spacecraft body frame

$\boldsymbol{a}$ = Rotor spin axis, component of unit vector defining rotation axis

$\boldsymbol{J}$ = Second moment of inertia matrix, not about mass centre in
    spacecraft body frame

$I_w$ = Moment of inertia about the rotor rotational axis

$\omega_w$ = Rotor spin rate relative to spacecraft body

$H_w$ = Magnitude of component of absolute angular momentum about
    rotor spin axis.

The equation (2.5) breaks down the external torque into a control torque and disturbance torque. The relationship between these torques can be seen in Figure 2-2

[19], where the typical feedback control loop is shown for a spacecraft. The spacecraft torque becomes:

$$T = T_D + T_C \qquad (2.5)$$

where $T$ = Net torque

$T_D$ = Disturbance torque

$T_C$ = Control torque.

The control torque is what is applied by the attitude control system. The disturbance torque is a function of the orbit, spacecraft generated disturbances and the environmental conditions that the spacecraft will encounter during its orbital path and throughout its mission lifetime.

## 2.2.1.   Disturbance Torques

The disturbance torque that the spacecraft encounters on-orbit can be defined as torques from its environment and torques generated from on board the spacecraft. The environmental torques can come from a number of sources not limited to aerodynamic, gravity-gradient, solar radiation pressure and magnetic. The disturbance torques that can be generated on-board the spacecraft can come from, but are not limited to the operation of thrusters and/or mechanisms. The environmental torque disturbances are typically captured through mission requirements. The spacecraft generated disturbances are captured through bottom-up system requirements since these are driven by the interaction of various spacecraft systems. Some examples of environmental torques are described below with spacecraft generated torques not shown but typically captured on a case-by-case basis in acceptance testing of hardware as will be shown in Chapter 3

The aerodynamic torque can be described by equation (2.6). This torque comes from the interaction of the spacecraft and the atmosphere in the direction of travel:

$$T_D = r_{cp} \times F_a \qquad (2.6)$$

where $r_{cp}$ is the centre of pressure relative to mass centre vector in body coordinates and $F_a$ is the aerodynamic force described in equation (2.7):

$$F_a = \left(\frac{1}{2}\right)\rho V^2 S C_D \frac{V}{V} \tag{2.7}$$

where $\rho$ = Atmosphere density

$V$ = Spacecraft velocity vector

$V$ = Translational velocity

$S$ = Spacecraft projected area $\perp V$

$C_D$ = Drag coefficient, usually between 1 and 2 for free-molecular flow,

depends on satellite geometry and properties as well.

The gravity-gradient torque for a spacecraft in a near circular orbit with higher order gravitational harmonics neglected can be described by equation (2.8). If the spacecraft mass moment of inertia matrix has more than just the diagonal terms than a variation in gravity or a gravitational gradient can impose a torque. The body coordinates system is referenced in terms of an inertially fixed reference frame:

$$T_D = 3n^2 \hat{r} \times (I \cdot \hat{r}) \tag{2.8}$$

where $\hat{r} = \frac{r}{r}$ = Unit vector from planet to spacecraft

$n^2 = \frac{\mu}{a^3} \cong \frac{\mu}{R^3}$ = Orbital rate

$\mu$ = Gravitational constant

$I$ = Spacecraft moment of inertia tensor.

The solar radiation pressure torque can be described by equation (2.9). This torque is a function of the surface area that is facing the sun and the specific material properties such as emissivity, absorptivity and reflectivity:

$$T_D = r \times F_s \tag{2.9}$$

where $r$ = Body centre of mass to spacecraft optical centre of pressure

$F_s = (1 + K)p_s A_\perp$, is the solar radiation force

$K$ = Spacecraft surface reflectivity, $0 < K < 1$

$A_\perp$ = Spacecraft projected area normal to sun vector

$p_s = I_s/c$

$I_S = 1358 \frac{W}{m^2}$ , represents solar flux which is a function of the orbital

position

$c = 2.9979 \times 10^8 \ m/s.$

The magnetic torque can be described by equation (2.10). It is a function of the Earth magnetic field strength which is different pending orbital position and altitude. A secondary effect that the magnetic field can impose is hysteresis in ferromagnetic materials pending magnetic permeability of a material. This can be a parasitic effect and is further investigated in Chapter 4 with hysteresis rod acceptance testing. The magnetic torque is:

$$\boldsymbol{T}_D = \boldsymbol{M} \times \boldsymbol{B} \tag{2.10}$$

where $\boldsymbol{M}$ = Spacecraft magnetic dipole moment vector

$\boldsymbol{B}$ = Earth magnetic field vector.

## 2.2.2.   Control Torques

The control torque that is available to the spacecraft attitude control subsystem (ACS) is directly a function of the type of attitude control hardware onboard the spacecraft. The control hardware presented in this thesis is the reaction wheel actuator which is described in Chapter 3 and the hysteresis rod which is described in Chapter 4. Both chapters provide the acceptance testing that shows the response and in some cases the control torque that can be expected.

## 2.3   Typical Control Modes and Requirements

In addition to the requirements, the spacecraft operational modes must also be considered since these can limit the availability of certain attitude control hardware. Table 2-1 [6] provides a generalized list of spacecraft modes that can be expected. What is also critical is the coupling of these modes and the effect of this on spacecraft operation. For example, an undesirable effect could be during a slew mode where the spacecraft orientation changes such that the attitude determination system cannot provide a reasonable estimate on attitude error due to the unavailability of a star tracker. This can result in a control torque undershoot or overshoot as a result of larger error. Hence the interaction of spacecraft modes and attitude control availability needs to be well understood. This is important since the external

environmental torque exists during all spacecraft modes and can accumulate if the control is not present to mitigate them. The result of uncompensated disturbance torque may be an undesirable spacecraft orientation or tumbling at undesirable rates.

Table 2-1: Attitude Control Modes [6]

| Mode | Description |
| --- | --- |
| Orbit Insertion | On launch vehicle enroute to orbit insertion point |
| Acquisition | Initial determination of attitude and stabilization of vehicle. |
| Normal, On-Station | Used for majority of mission. |
| Slew | Changing orientation of spacecraft as required. |
| Contingency or Safe | Backup emergency mode in case normal operation mode fails. Could include minimal power usage. |
| Special | Requirement driven, needed previous modes do not satisfy all operational cases. |

In summary, the previous discussions of mission requirements, system coupling and any resultant derived requirements, disturbance torques and attitude control modes result in the subsystem control performance requirements. This result is summarized at a high-level in Table 2-2 [6], and is further used in acceptance testing of attitude control hardware. The testing process uses the performance requirements to verify that in fact the attitude control hardware will meet the requirements.

It is at this point that attitude control hardware can be chosen based on availability and performance specifications. If the requirement falls beyond previously used operational envelopes of control hardware then the acceptance testing must capture this variation and verify that control hardware will still meet requirements. If, as a function of requirements, the new operational envelope changes the behaviour of the control hardware such as power consumption etc., then the derived system requirements might need to be generated for the power system. This is in order to accept any variation of performance. This can be expected as will be shown in Chapter 3 with reaction wheel regeneration which comes as a consequence of higher performance requirements.

Table 2-2: Control Performance Requirements [6]

| Area | Definition |
|---|---|
| Accuracy | How well the vehicle attitude can be controlled with respect to a commanded direction |
| Range | Range of angular motion over which control performance must be met |
| Jitter | A specified angle bound or angular rate limit on short-term, high-frequency motion |
| Drift | A limit on slow, low-frequency vehicle motion. Usually expressed as angle/time |
| Settling Time | Specifies allowed time to recover from maneuvers or upsets. |

## 2.4 Actuator Performance

Given the attitude control requirements it should be understood that there are only certain types of attitude control hardware that are available on the nanosatellite spacecraft scale and that can potentially satisfy these requirements. The performance of available actuators can be further divided into accuracy, lifetime, pointing limitations and attitude manoeuvrability. Table 2-3 summarizes the available types of hardware with some segmentation based on expected performance.

It can be seen from the table that for sub-degree pointing the reaction wheel and thruster are essentially the only available actuator and that there is no passive method available. For greater than a degree pointing accuracy there exist a number of methods, of which some are passive. This is extremely important when considering missions such as BRIght Target Explorer − Constellation (BRITE-Constellation) where sub-degree pointing is a requirement and due to volume constraints the only form of actuation that is available is a reaction wheel. Hence, this generates an overwhelming importance on acceptance testing, which must verify that the limited availability and performance of hardware does verify requirements.

Table 2-3: Types of Attitude Control Hardware [6]

| Type | Pointing Options | Attitude Maneuverability | Typical Accuracy | Lifetime Limits |
|---|---|---|---|---|
| Reaction Wheels | No constraints | No constraints | $+/- 0.001\, deg$ to $+/- 1\, deg$ | Life of sensors and wheel bearings |
| Magnetorquers | North/South only | Very limited | $+/- 5\, deg$ (2 axes) | Power |
| Thrusters | No constraints | No constraints High rates possible | $+/-0.1\, deg$ to $+/-5\, deg$ | Propellant |
| Passive Magnetic | North/South only | Very limited | $+/- 5\, deg$ (2 axes) | None |

## 2.5   Active Attitude Control Actuators

This section will provide a review of the operational principles behind the reaction wheel, magnetorquer, thrusters, permanent magnets and hysteresis rods. The described control hardware is designed based on an operational principle that given a defined input a desired amount of output is generated. This behavior is dependent on the technology behind each type of control hardware. Typically the active control hardware will require a communications interface such as the Nanosatellite Serial Protocol (NSP) developed by Space Flight Laboratory (SFL) and power input. The passive hardware will not consume power and will not require a communication interface. The performance is set during the design phase and is not typically modified on-orbit.

Each technology interfaces with the spacecraft attitude dynamics discussed earlier and it can either add or remove angular momentum from the spacecraft. The active control can adjust the amount of energy removed, whereas the passive control is fixed to remove a predefined amount of energy from the spacecraft. In both cases the result is a modification of the angular momentum the spacecraft has at any given time.

## 2.5.1.   Reaction Wheel

The reaction wheel actuator is an active attitude control hardware and can be used from coarse to fine pointing. A sample reaction wheel that was used on NASA's Lunar Reconnaissance Orbiter (LRO) is shown in Figure 2-3. This type of actuator is limited by the amount of angular momentum it can store and at points in the spacecraft mission it will saturate. At which point it will enter momentum management modes where it will reduce its angular momentum. The amount of torque that it can produce is a function of power availability and motor design. Its operational principle in relation to spacecraft dynamics is coupled through the changing of its own angular momentum which in turn changes the spacecraft angular momentum about that same axis.
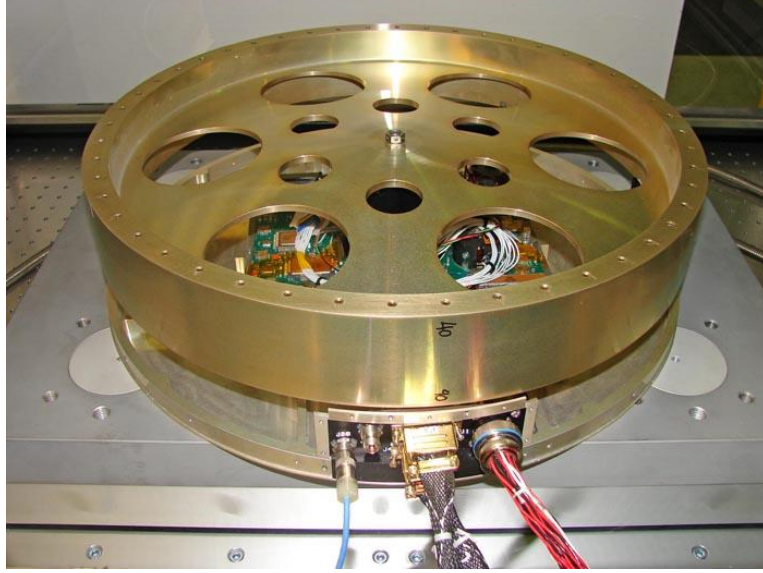


Figure 2-3: Reaction Wheel for NASA Lunar Reconnaissance Orbiter (LRO)

The control torque input to the spacecraft body can be defined as shown in equation (2.11). The output is the product between the rotor mass moment of inertia and angular acceleration generated by the reaction wheel motor in the spacecraft body frame. A further analysis of reaction wheel and acceptance testing is provided in Chapter 3. The torque produced by a reaction wheel can be described by:

$$T_c = I_w \dot{\omega}_w$$

(2.11)

where $I_w$ = Chosen rotor mass moment of inertia

$\dot{\omega}_w$ = Angular acceleration of rotor.

## 2.5.2. Magnetorquer

The magnetorquer is an active attitude control hardware and has only been used in the past for coarse pointing due to its coarse control authority. A sample magnetorquer that had been design by Surrey Satellite Technology Limited (SSTL) can be seen in Figure 2-4. This device works on the principle of generating a magnetic dipole moment by passing a current through a coil. The magnetic dipole applied against the Earth's magnetic field as a function of orbital position generates a torque. The coil in this device can be open to vacuum or wrapped around a hysteresis rod to change the working permeability and hence the resultant generated $B$ field of the device which can increase or decrease its dipole strength. This device is usually used only in low to medium Earth orbit due to the availability of Earth's magnetic field. It is also typically used to perform spacecraft detumbling and momentum reduction in reaction wheels.
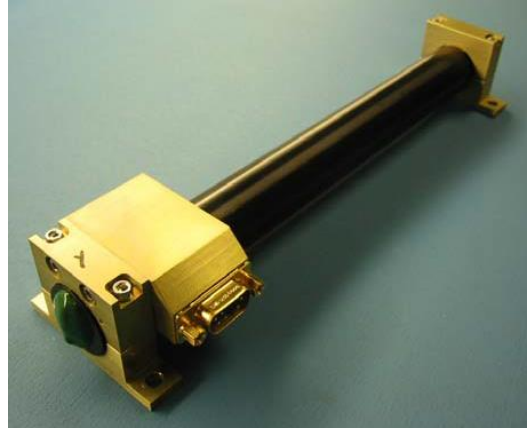


Figure 2-4: Surrey Satellite Technology Limited (SSTL) Magnetorquer

The equation (2.12) provides the relationship between the control torque, Earth's magnetic field and magnetic dipole generated by the spacecraft [18]. The torque generated by a magnetorquer can be described by:

$$\boldsymbol{T}_c = \boldsymbol{M} \times \boldsymbol{B}$$
(2.12)

where $\boldsymbol{M}$ = Spacecraft magnetic dipole moment

$\boldsymbol{B}$ = Earth magnetic field.

### 2.5.3.    Thrusters

The thruster is an active attitude control hardware which can be used from coarse to fine pointing pending implementation. The device operates on a principle of expelling propellant through a nozzle which in turn generates thrust. This thrust or force at a moment arm from the mass centre of the spacecraft generates a torque. This actuator works in pairs, meaning two are required at any time to generate a balanced moment about the centre of a spacecraft, this is as to ensure that only rotational motion is generated and the translational motion is minimized when thrusters are used only for attitude control. It is limited by the amount of propellant and power available on board the spacecraft. At the time of writing this thesis no information has been found by the author that this technology has ever been used for attitude control on a nanosatellite scale. A sample thruster designed by SSTL is shown in Figure 2-5.
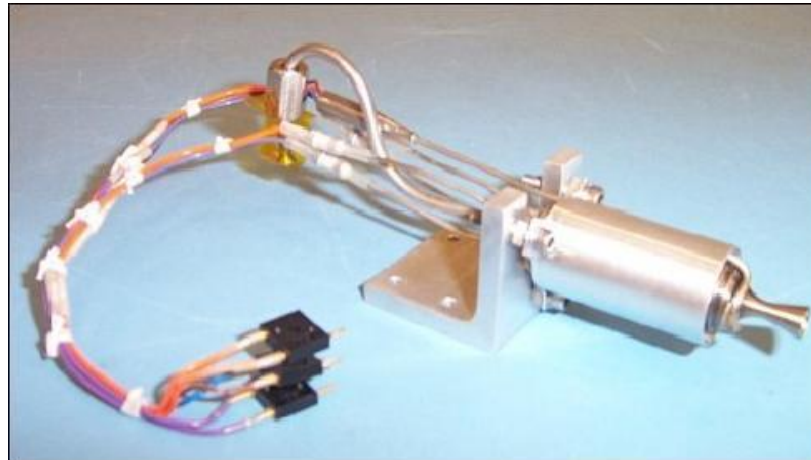


Figure 2-5:  SSTL Resistojet Thruster

## 2.6   Passive Attitude Control Actuators

The passive attitude control actuators are actuators that provide restoring torques and can remove angular momentum from spacecraft body without the need for active control. It should be noted that some cases exist where the passive attitude control will in fact add angular momentum to the spacecraft. Overall this provides for a very rudimentary system with only coarse pointing at best. In the past the passive control technique utilized on nanosatellite spacecraft was a combination of hysteresis rods and permanent magnets.

The hysteresis rods provide damping which essentially removes angular momentum from the spacecraft for as long as the spacecraft has any residual rotation. The

permanent magnets provide a permanent dipole on the spacecraft which will provide stabilization about only two axes. A third axis will typically result with a residual uncontrolled spin.

## 2.6.1. Hysteresis Rod

The hysteresis rod is a piece of ferromagnetic material with specific properties that has been designed to a particular geometry. The coupling between the geometry and choice in material provide for a final magnetic permeability which is the relationship between the magnetic field strength input (Earth magnetic field) and magnetic flux density (rod magnetic flux density output). The principal of operation is that as the magnetic field strength input varies due to the spacecraft rotation and orbital position the rod as a function of magnetic permeability absorbs this field and generates a magnetic flux density. This process absorbs the energy from the spacecraft angular momentum and reduces it over time. A sample hysteresis rod designed by the Space Flight Laboratory (SFL) can be seen in Figure 2-6. More detailed analysis and acceptance testing of a hysteresis rod is provided in Chapter 4.



Figure 2-6: Space Flight Laboratory (SFL) Hysteresis Rod

## 2.6.2. Permanent Magnets

The permanent magnet is typically part of a passive attitude control scheme described at the beginning of this section. It provides a permanent dipole on board the spacecraft. The limitation is that it can only stabilize a spacecraft about two axes. It can also add undesired parasitic hysteresis in any ferromagnetic materials that are in proximity to the dipole on board the spacecraft. This is an effect that is closely monitored and is minimized in the design process. Part of the work in the hysteresis rod design is to minimize the effect of the permanent magnet on the hysteresis rods. A sample permanent magnet can be seen in Figure 2-7. These can be purchased in many shapes and sizes and have been used quite extensively on nanosatellites.
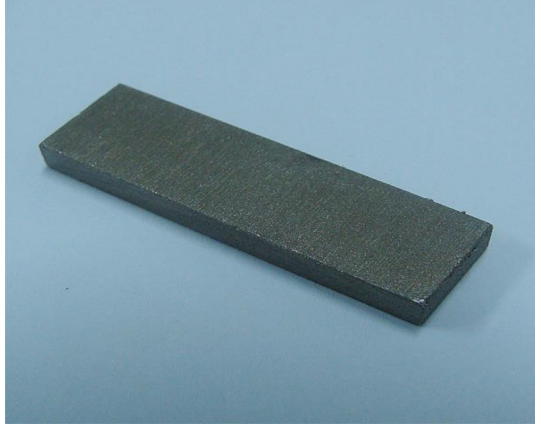
Figure 2-7: Permanent Magnet

## 2.7   Acceptance Testing

This chapter has provided the basic foundation on the type of attitude control hardware that is available for nanosatellite scale of spacecraft and the inherent limitations. It is important to understand that the acceptance testing process in the next two chapters provides the link between the requirements and what works in application (hardware and software). This link corresponds to the gap that must be crossed in order to verify that the attitude control hardware actually does behave as required and does so within a certain tolerance. Hence the acceptance testing is crucial in establishing the foundation of what can be accomplished and what the limits are in attitude control hardware.

# Chapter 3

# Reaction Wheel Actuator

The reaction wheel actuator at the nanosatellite scale employs a unique design that balances power consumption, volume, mass and torque output. The two models of actuators for which the analysis and acceptance testing is shown in this Chapter are the RW0.03 and RW0.06 reaction wheels. These reaction wheels were developed jointly between Space Flight Laboratory (SFL) and Sinclair Interplanetary. The hardware design of these reaction wheels has had previous flight heritage on SFL missions such as CanX-2 and AISSat-1 [4]. Since their inception the requirements imposed on these actuators have become more demanding and as such the purpose of this chapter is to ensure that the most stringent of requirements are met by these actuators. Hence, the characterization of a reaction wheel, experimental validation of performance and acceptance testing is presented.

## 3.1 Principal of Operation

The close examination of a reaction wheel actuator reveals that it is in fact an electric motor with an oversized rotor. The motor component is essentially a device that translates the electromotive force (EMF) to a magnetomotive force (MMF) which acting on permanent magnets embedded in the rotor produce a rotation. This rotation can be controlled to maintain a state (angular speed) or produce a change in state (angular acceleration). In a spacecraft, given a particular mass moment of inertia of a rotor the device will produce a torque about the mass centre when commanded to produce angular acceleration. This becomes the main linkage between motor design and attitude control dynamics discussed in Chapter 2.

The motor design can be based on a direct current (DC) or alternating current (AC) design. The choice is typically DC since the availability of AC power on board a

spacecraft is non-existent and would require conversion which has inherent losses. This intrinsic choice is important since a DC design has an extra benefit in that it can be designed in such a way that the current consumed is proportional to the torque output of the device [21]. This is extremely beneficial, since given a conversion factor and through simple current measurements the actuator torque output can be estimated. Also simplified is the control since the system tends to have a linear response. The boundaries of this linear response and the inherent non-linearities that are introduced as a consequence of control and motor design are the focus of this chapter.

## 3.2  Reaction Wheel Specifications

The reaction wheels that were analyzed can be viewed on Figure 3-1, where the relative size of the wheels can be seen. The RW0.03 can be seen on the left and RW0.06 can be seen on the right of the figure. These reaction wheels differ in their dimensions, mass and power consumption as shown by Table 3-1, which provides the specification for these reaction wheels. The similarities are in the DC motor design and controller behaviour which will be shown in later sections.
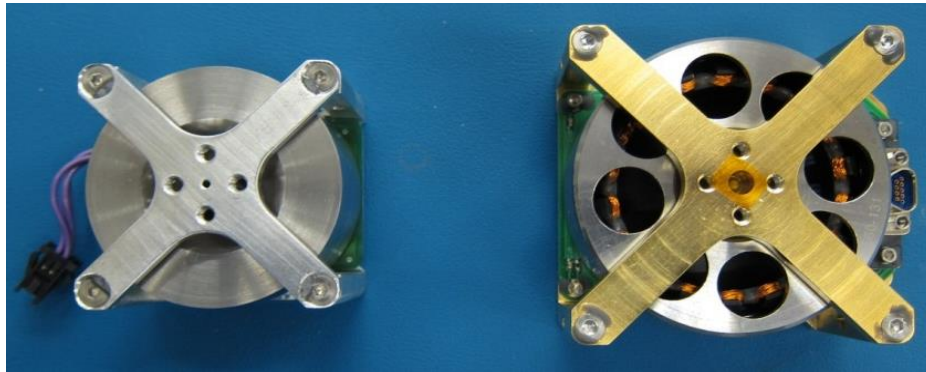


Figure 3-1: SFL-Sinclair Interplanetary Reaction Wheels

As shown by the specification contained in Table 3-1, these reaction wheels are rated based on momentum storage and nominal torque output. For the purposes of this chapter the focus will be on the supply voltage and power consumption which as it will be shown inherently influence the control torque output. This will become clear in the next section.

Table 3-1: SFL-Sinclair Interplanetary Reaction Wheel Specifications

| Parameters | RW-0.03 | RW0.06 |
|---|---|---|
| Nominal Momentum | $3 \times 10^{-2}\ Nms$ @5600$RPM$ | $6 \times 10^{-2}\ Nms$ @ 6500$RPM$ |
| Nominal Torque | $2 \times 10^{-3}\ Nm$ | $5 \times 10^{-3}\ Nm$ @ 28 $VDC$ |
| Control Mode | Speed or Torque | |
| Command/Telemetry | NSP over UART | NSP over UART, RS-485 |
| Mechanical | $50x50x40\ (mm), 185g$ | $75x65x38\ (mm), 225g$ |
| Supply Voltage | $3.4\ to\ 6.0VDC$ | $7.5\ to\ 35VDC$ |
| Supply Power | $1.5W\ max$ | $7.0W\ max$ |
| Environment | $-40ºC\ to\ +\ 70ºC$ Operating temperature | |
| Reliability | Diamond coated hybrid ball bearings Redundant motor windings, radiation lot screened parts | |

## 3.3   Reaction Wheel Characterization

Prior to actual testing of the RW0.03 and RW0.06 reaction wheels an analytical approach was taken to predict the performance envelope that could be attained from each type of wheel. This was done in an effort to better understand what the performance limits could be and if any undesirable behaviour could exist within the operating ranges. This type of analysis, as will be shown, also provided the relationship between power consumption, torque output and speed as a function of operating at a particular voltage and current.

### 3.3.1.   Performance Assumptions

The performance assumptions that were used in the initial analysis were as shown in Table 3-1 and the Interface Control Document (ICD) for RW0.03 and RW0.06 which is readily available and kept current on the Sinclair Interplanetary website. The purpose of obtaining the specifications and limits was as to estimate the DC motor performance envelope. It should be understood that this design of a reaction wheel is essentially a DC motor with an oversized rotor, which focuses the analysis on the DC motor which is based on electrical and mechanical design.

The list of the assumptions was as follows for both reaction wheels:

- Maximum speed, software limited for both

- Maximum torque output

- DC Motor Kt and Ke estimate

- Winding resistance estimate

- Hardware DC current limits

- Voltage limits

- Rundown data

These were the main performance parameter assumptions into an analytical model which was then used to generate a performance contour plot as will be shown in later sections.

## 3.3.2.   DC Motor Characterization

The reaction wheels were based on a Brushless DC Motor (BLDC) design which posed certain challenges when characterizing these motors. Through detailed analysis of the BLDC design some limitations were discovered and resultant simplifications had to be taken in order to provide an accurate characterization. The type of a BLDC design used was a 3 phase AC motor winding setup coupled with a DC motor control. This type of a setup can be modelled as a typical DC motor with current telemetry for each winding. The complication was that only a single current sensor was used to control the output to the windings which discounted any possibility of current telemetry per phase. This in turn limited the model of the BLDC motor from a 3 phase to a single phase model which is the only model that could be experimentally verified and as will be shown has limitations in the validity of the motor specific constants.

The single phase DC motor model was chosen with the assumption that all three phases behaved as one and as a result the current and voltage to all phases was the same due to the single current sensor design. This assumption allowed the use of equation (3.1) as a DC motor model [22]. This equation allows the representation of the basic relationship between the voltage, torque, motor constants and motor speed. The relationships between the described parameters are then used to generate an analytical power contour plot which predicts the performance envelope of the DC motor.

It should be noted that given the availability of current telemetry per phase higher-order models could have been used providing a more detailed and more accurate characterization. The motor constants for a single phase model will not be directly representative of the actual 3 phase motor model constants. Again the single phase motor model is as follows:

$$V = L_a \frac{dl_a}{d_t} + RI_a + K_E \omega \qquad (3.1)$$

where $V$ = Voltage applied to the motor windings

$L_a \frac{dl_a}{d_t}$ = Variation of inductance due to moving coil

$R$ = Winding resistance

$I_a$ = Current consumed by motor

$K_E$ = Motor speed constant

$\omega$ = Motor angular speed.

Assuming a uniform magnetic field within the motor, the relationship between the current and torque becomes proportional as per equation (3.2):

$$T_g = K_T I_a \qquad (3.2)$$

where $T_g$ = Internal motor torque

$K_T$ = Motor torque constant

$I_a$ = Current consumed by motor.

The relationship between torque and angular speed becomes as shown by equation (3.3), where the torque is comprised of an angular acceleration term and a term due to friction. This can be described as follows:

$$T_g = J_L \frac{d\omega}{d_t} + T_m \qquad (3.3)$$

where $J_L$ = Mass moment of inertia of motor and load

$\frac{d\omega}{d_t}$ = Angular acceleration of rotor

$T_m$ = Opposing torque in motor.

The opposing torque in motor can be described as shown in equation (3.4):

$$T_m = D\omega + T_f + T_L \tag{3.4}$$

where $D\omega$ = Viscous friction torque which is angular speed dependent

$T_f$ = Constant friction of the motor

$T_L$ = Constant friction of any external load connected to the motor.

Under the assumption of steady state condition with current constant, the equations (3.1) and (3.2) can be combined to form equation (3.5).

$$V = \frac{T_g R}{K_T} + K_E \omega \tag{3.5}$$

Given the steady state conditions of equation (3.5), when applied torque approaches zero then the no load velocity becomes as shown in equation (3.6). Consequently the zero speed stall torque is shown in equation (3.7). These two equations become the intercept points on a torque-speed curve which shows the relationship between the speed of the motor and torque. This relationship also shows that the ultimate limit on speed and torque of the motor is the available voltage:

$$\omega_{NL} = \frac{V}{K_E} \tag{3.6}$$

and

$$T_{gs} = \frac{V K_T}{R} \tag{3.7}$$

where $T_{gs}$ = Internal motor stall torque

$\omega_{NL}$ = Motor angular speed.

The limiting applied voltage in equation (3.6) and (3.7) provides a relationship between angular speed and torque which is described by equations (3.8) and (3.9). The speed regulation constant is the slope at the maximum speed that can be attained given a requested torque. The slope of this line is bounded on one end by the maximum theoretical speed provided by equation (3.6):

$$\omega = \omega_{NL} - R_m T_g \tag{3.8}$$

$$R_m = \frac{R}{K_T K_E} \tag{3.9}$$

where $R_m$ = Speed regulation constant.

The single phase DC motor equations described thus far pertain to the dynamics of the motor and provide a variety of relationships which in conjunction with the next section will be used to provide the analytical power contour plot for the reaction wheel motor. This is important since this will provide a map of the theoretical performance that can be obtained from a reaction wheel, which in later work will be validated given experimental results.

### 3.3.3.   Power Dissipation of DC Motors

The Brushless DC Motor (BLDC) used in the reaction wheel can be considered to be an energy converter. It converts electrical power to mechanical during any acceleration or steady state conditions and back to electrical during any deceleration conditions [22]. Hence, the behaviour of power consumption and dissipation is coupled with torque and speed and needs to be described in conjunction to the relationships presented in the previous section. This has obvious implications to a spacecraft power system where it is important to know how much power the reaction wheel might demand under required torques and again how much power it might regenerate.

The power conversion and inherent losses in a BLDC motor can be visualized by Figure 3-2, which shows a flow chart of how the power losses are coupled, where during the power conversion the motor will have load and speed sensitive losses.

In order to define power consumption we begin with the input power to the motor which can be described by equation (3.10). One main assumption is that the motor behaves as a linear resistive load:

$$P_i = V I_a \tag{3.10}$$

where $P_i$ = Power input to the motor.
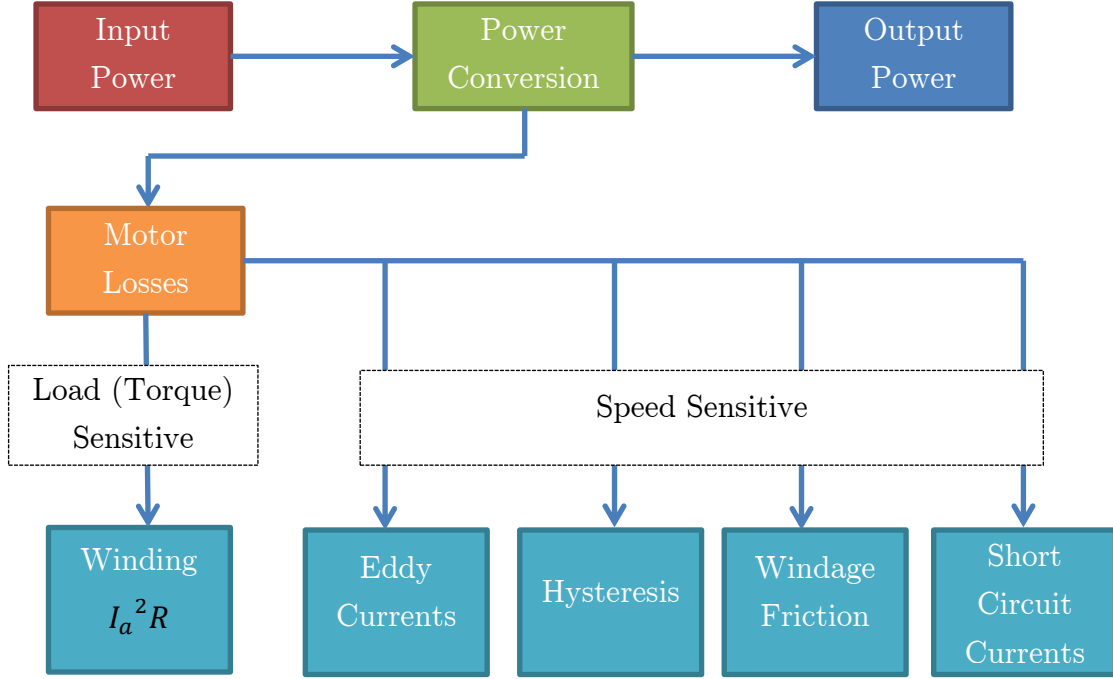
Figure 3-2: Power Losses in Brushless DC Motor (BLDC) Design

Assuming steady state conditions and substituting equation (3.1) into (3.10), we get input power as a function of motor losses shown in equation (3.11):

$$P_i = I_a{}^2 R + I_a K_E \omega \qquad (3.11)$$

Combining (3.2), (3.3), (3.4) and (3.11) with the exclusion of $T_L$ which corresponds to losses due to mechanical coupling between motor and an external load, we get equation (3.12). The result describes in a general sense the instantaneous power dissipation given a torque load and motor losses of a BLDC motor. The motor frictional losses can be quantified through further friction modelling. Hence the instantaneous dissipative power can be described by:

$$P_L = I_a{}^2 R + \frac{K_E \omega T_f}{K_T} + \frac{K_E D \omega^2}{K_T} \qquad (3.12)$$

### 3.3.4.   Modeling Friction

The losses due to friction in a BLDC motor as shown in equation (3.4) can be rewritten without $T_L$ and as a function of constant and speed sensitive losses as shown in (3.13). As mentioned earlier the $T_L$ component is being omitted since the reaction wheel is not coupled mechanically to any external loads. This result is a polynomial which can be extracted through a curve fit of the motor free-spinning spin down. Hence the opposing torque can be described by:

$$T_m = D\omega + T_f$$

(3.13)

The modelling of friction was accomplished using previously recorded reaction wheel speed rundown data as a function of time. The reaction wheel started the rundown at an approximate speed of $+/-\sim700\ rad/s$. Data in the negative and positive rundown profiles was curve fit using a polynomial function. The terms in the resultant polynomial are a representation of the opposing torque described by equation (3.13). An example of the opposing friction is provided in the Section 3.4 of this chapter.

### 3.3.5.   Analytical Dissipative Power Contour Plot

The initial dissipative power contour plot is based on the single phase DC motor model, power dissipative model and friction approximation from past reaction wheel data as previously described. This plot provides the power consumption of the reaction wheel given a torque and speed state. The plot is generated using equations (3.5) and (3.12), which describe the relationships between power, current, voltage, speed and torque. The initial plots can be seen in Figure 3-3 for the RW0.03 reaction wheel and Figure 3-4 for the RW0.06 reaction wheel.

These plots show the speed of the reaction wheel on the x-axis, the torque on the y-axis and the coloured contours correspond to consumed or regenerated power. The positive contours represent power consumed and the negative contours represent power regenerated. Also the lines that appear in parallel show the limits as a function of voltage and current, where the current limits the maximum torque that can be obtained and the voltage limits the maximum speed. Plotted is the rundown data that had been used for modelling friction, which also shows the power, torque and speed envelopes within which the wheel has previously operated. The area on the plot where the rundown data is parallel to the voltage lines corresponds to the speed

regulation constant as described by equation (3.9). This was the initial attempt to estimate BLDC motor performance.
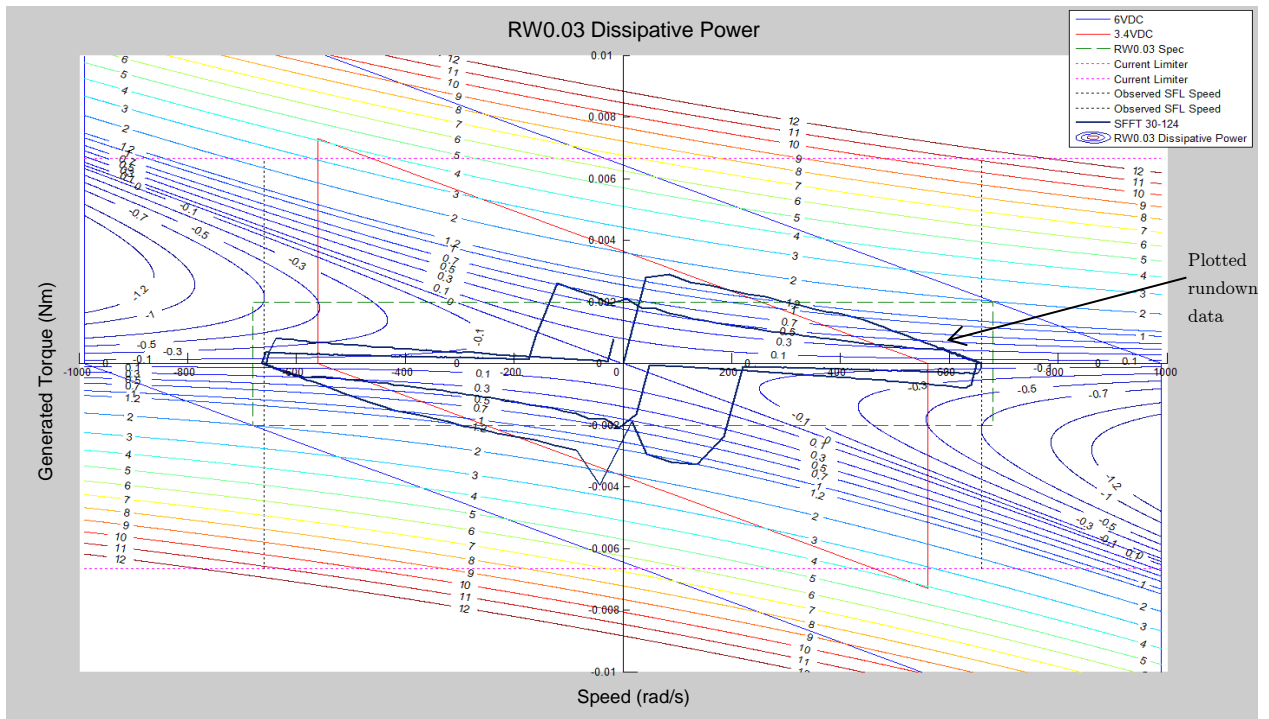


Figure 3-3: RW0.03 Analytical Power Contour Estimate
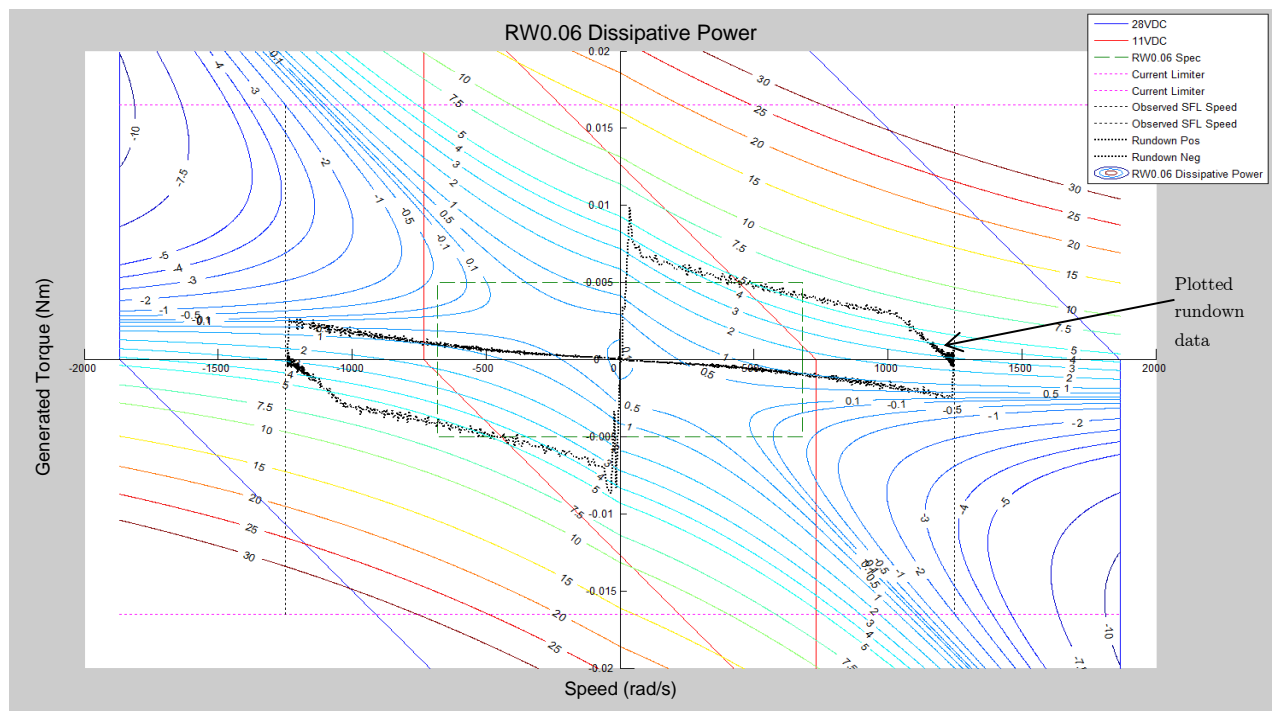


Figure 3-4: RW0.06 Analytical Power Contour Estimate

Detailed analysis of these plots has shown that the following limitations exist with the current reaction wheels:

- RW0.03 Estimates
    - Peak power consumption of 1.5W
    - Peak regeneration of 1W
    - Maximum speed of 970 rad/s at 6VDC
- RW0.06 Estimates
    - Peak power consumption of 7W
    - Peak regeneration could be 4W
    - Maximum speed of +1600 rad/s at 28VDC
- Both reaction wheels showed large torque overshoot during zero crossings

The above information was instrumental in providing direction for further experimental testing of reaction wheels.  The power peak consumption was confirmed against reaction wheel specifications shown earlier in Table 3-1.  It can be seen that these were reasonable.  The estimates of the regeneration zones of the DC motor were apparently being avoided through the use of a power controller in the reaction wheel software.  The concern was still present that the reaction wheel motor could regenerate and as such a shunt resistor was chosen to protect the DC motor.  It is important to protect against regeneration since a DC motor is the only path of resistance and the regeneration can short out through the motor causing damage.  Further discussion on shunt resistor sizing and reaction wheel safety is provided in Section 3.7.  Finally the torque performance, speed limits and overshoot behaviour was chosen to be verified.

The analytical power contour estimate provided the following key aspects of the RW0.03 and RW0.06 reaction wheel DC motors that needed to be verified prior to the commencement of acceptance testing:

- Peak power consumption
- Peak regeneration
- Maximum speeds at operating voltage
- Overshoot behaviour at zero crossings
- Torque response

## 3.4   Experimental Verification of Model

The experimental verification of the reaction wheel DC motor model was completed to calibrate and verify the analytical results shown in the previous section. This is important since the characterization map can be used to choose performance envelopes in acceptance testing such that requirements are met. The testing was performed using RW0.03 and RW0.06 reaction wheels.

### 3.4.1.   Test Methodology

The test methodology consisted of operating each type of reaction wheel through speed, torque and digital to analog converter (DAC) profiles. These profiles were termed speed box, torque box and DAC box. In addition, rundown data was to be captured, providing an update to the opposing friction estimate. In an effort to ensure maximum data resolution and correct time stamping the data acquisition process was reviewed, and best practice was established.

The speed box profile commanded the reaction wheel from its most negative speed to its most positive speed and back again. The telemetry that was polled was speed and time. This provided for a confirmation of the maximum speed envelope at incremental voltages that were to be required for acceptance testing. The overall response of the speed controller was measured through this profile.

The torque box profile commanded the reaction wheel through steps of torque. Each torque was applied at the maximum opposing speed providing a torque response map in all four motor quadrants. It was determined early in testing that the torque telemetry from the reaction wheel was too noisy and would not provide meaningful results. The data polled ended up being speed and time and in post processing the incremental torque was determined. This profile captured the overall response of the torque controller.

The digital to analog converter is an open loop command to set a duty cycle for the motor output to the windings. This profile sets the duty cycle output in increments and polls the current with time as telemetry. This was an attempt to measure the maximum possible regeneration that the motor could encounter.

All testing for both the RW0.03 and RW0.06 was completed using a shunt resistor as defined in Section 3.7. In addition to the reaction wheel telemetry, external current was recorded throughout all testing to measure and confirm externally the dissipative power behaviour of the reaction wheel.

### 3.4.2.    System Limitations

The testing was limited by a number of factors which were inherent to the design of the reaction wheel. Some observed notable limits were:

- Only 1 parameter can be polled at a time

- Resolution of the reaction wheel data is limited by the data communication interface

- External current measurements were limited to $1kHz$

- Application interface to the reaction wheel was on a Microsoft Windows platform which added complexity as shown in Section 3.4.4

### 3.4.3.    Test Setup

The primary concern during testing was the safety of the reaction wheels actuator since some were intended for flight. For this reason the reaction wheels were mounted in a protective enclosure with a dedicated harness routed to each reaction wheel. This allowed for the device to be fully isolated and safe for bench top testing. Below Figure 3-5 shows four RW0.06 reaction wheels in an enclosure.
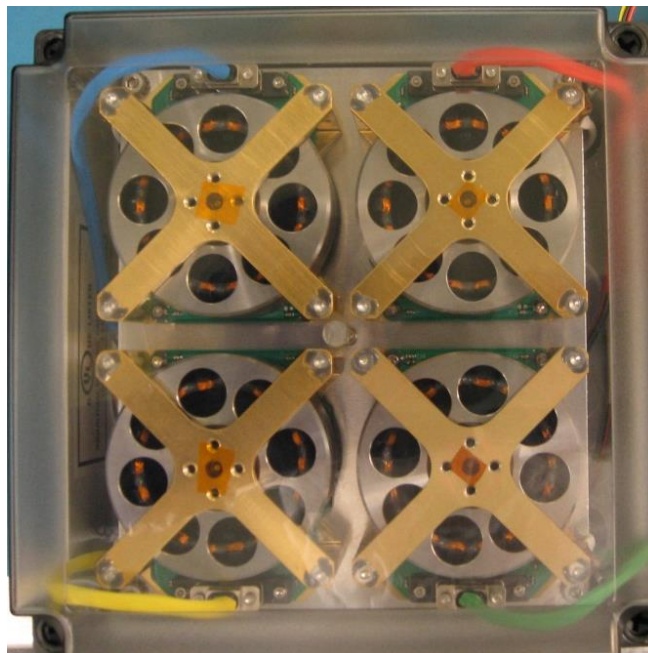


Figure 3-5: RW0.06 Reaction Wheel Enclosure

The interface between the reaction wheel and the control software is shown by Figure 3-6. The test setup consisted of the following items:

- Reaction wheel enclosure with reaction wheels

- Isolated variable DC power supply rated for the operating voltage of the reaction wheels

- Shunt resistor rated for estimated regeneration of reaction wheels with a safety margin

- Communication converter for signal levels

- PC with Microsoft Windows XP and a free communication port capable of 57,600 and 115,200 baud rates

- Wheelterm interface application
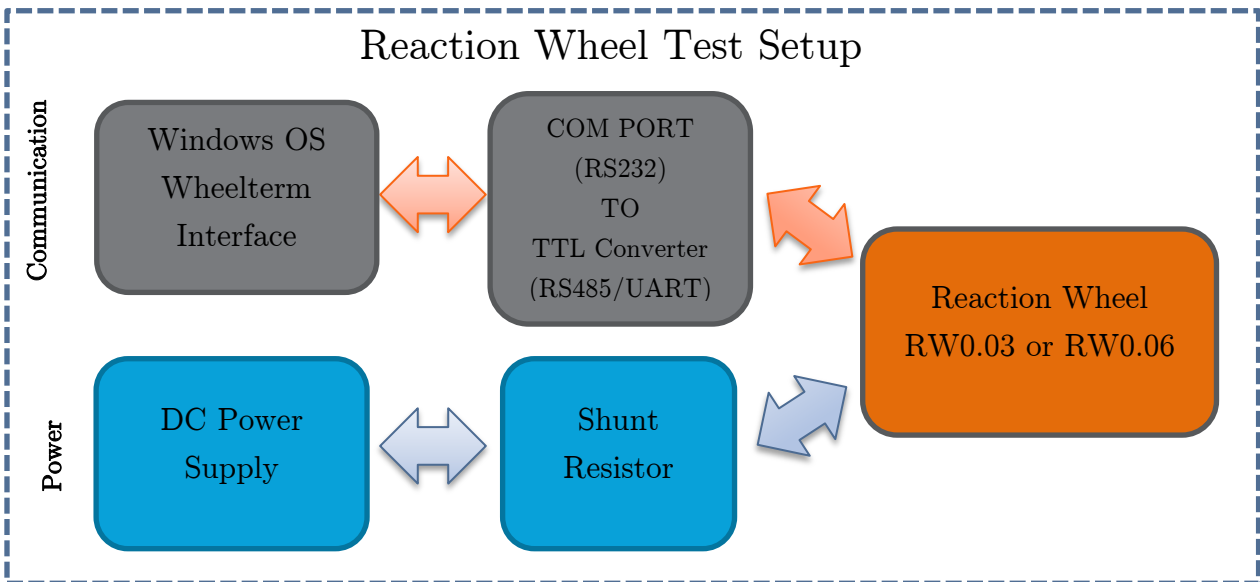


Figure 3-6: Reaction Wheel Test Setup

### 3.4.4. Acquisition of Data

Prior to any testing it was critical to identify the maximum reliable data polling rates that could be obtained for the RW0.03 and RW0.06 reaction wheels. Two requirements had to be met: first, correct time stamping had to be implemented, and second, there was not to be any packet loss while maximizing the polling rate. Using an oscilloscope a test was performed measuring the lag of the wheel response. This was in an effort as to determine the limiting factor in communications. It was measured that the reaction wheel interface response to a telemetry packet request had

a maximum of $2ms$ of delay, while the lag of Wheelterm (interface application) sending the next command was $16ms$. The wheel packet response lag to a packet request can be seen on Figure 3-7, where the wheel response is only $2ms$ behind the wheel command. Based on the limiting $16ms$ latency it was determined that the maximum polling rate of the interface to the reaction wheel could not exceed $60Hz$. The next step was to determine at what polling frequencies of equal to or less than the maximum can the data with no packet loss and correct time stamp be acquired.
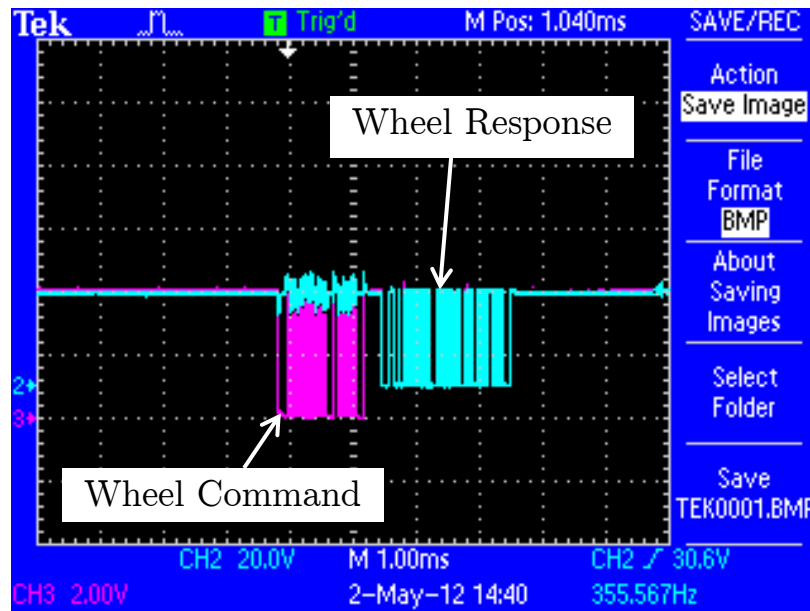


Figure 3-7: RW0.03 Communication Interface

Testing was performed on $21$ RW0.03 and 4 RW0.06 reaction wheels. The results showed that consistent time stamps and no packet loss could only be acquired during $62Hz$ and $21Hz$ polling rates. Figure 3-8 shows the results for RW0.03 data time stamp and packet loss, where the correct torque jitter of less that $1.2 \times 10^{-6}\,Nm$ identifies valid polling results. It should be noted that up to this point the polling rates that had be used were less than $20Hz$ with some packet loss. Some adjustments had to be made during the RW0.06 testing which included a longer than typical communication cable as a consequence of the enclosure. The longer cable caused some packet loss initially but was remedied by adding a termination resistor which is required by the RS485 standard.

Through all the testing there was no difference in the results obtained between the RW0.06 and RW0.03, which also supported that the limiting factor in the current test scheme is the Windows environment.  It is speculated that the Windows kernel is limited to a $16ms$ scan cycle of the communication port which cannot be changed. Future considerations were to utilize an embedded test platform or a Linux based system in an effort to reduce latency.  This work established best practice for communication interfacing during testing of reaction wheels.
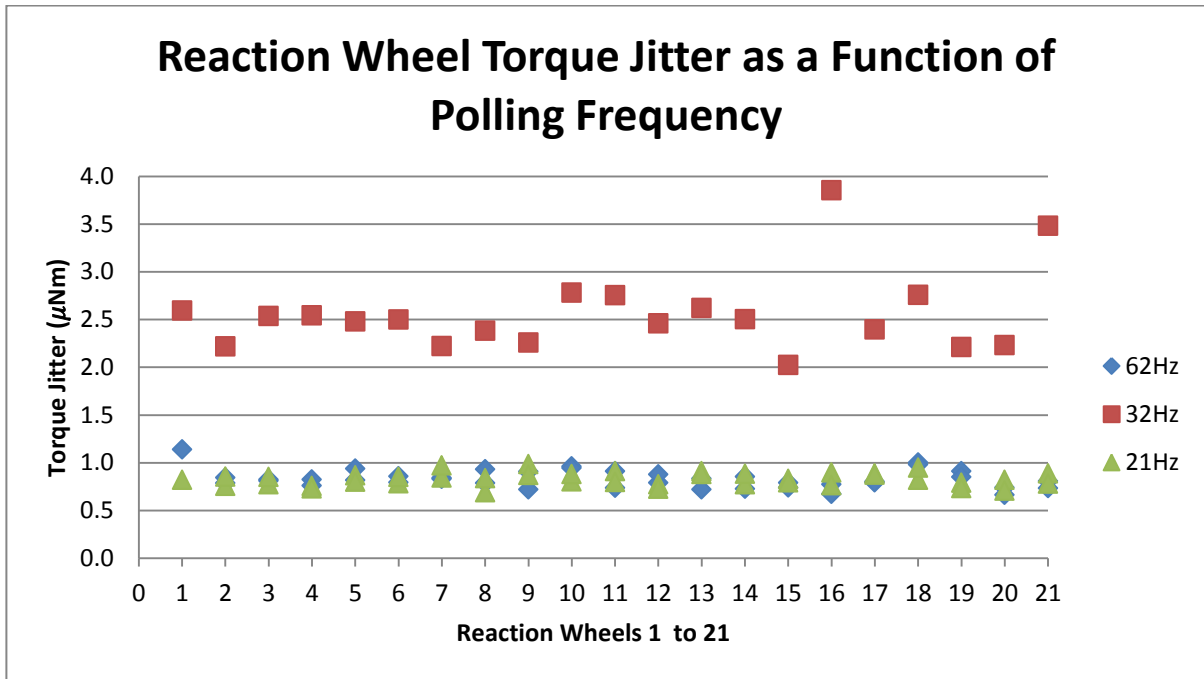


Figure 3-8: RW0.03 Data Polling Frequency Comparison

### 3.4.5.  Verification of Friction Estimate

Given the verified data acquisition interface, confirmation of reaction wheel friction was obtained.  This estimate was done to confirm the friction estimate that was derived from past reaction wheel rundown data as discussed in Section 3.3.4.  The secondary benefit of this estimate confirmation was that the new set of data provided the friction estimate with a higher resolution.  The data for both RW0.03 and RW0.06 was fitted using a second order polynomial to ensure that the first two terms of friction are captured according to (3.13).  The results for the RW0.03 reaction wheel are shown in Figure 3-9, and for RW0.06 reaction wheel in Figure 3-10.  These results were implemented in the power contour map for the reaction wheels as is shown in the next section.
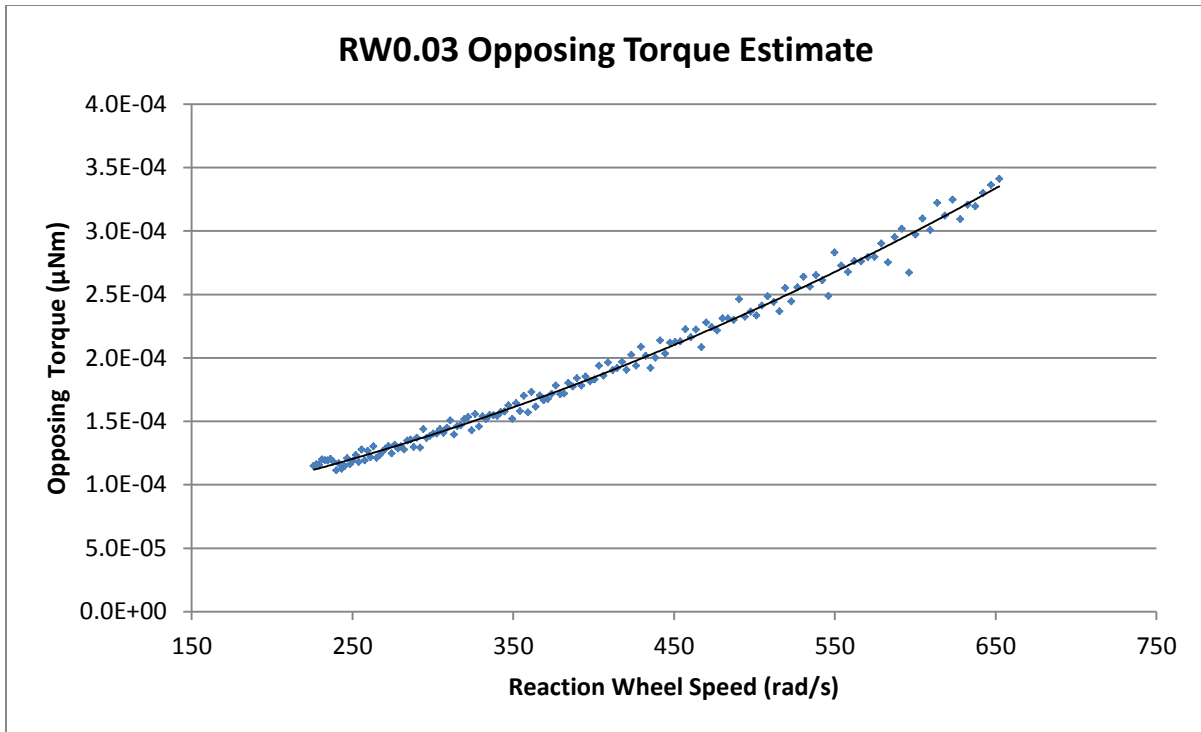
Figure 3-9: RW0.03 Opposing Torque Estimate
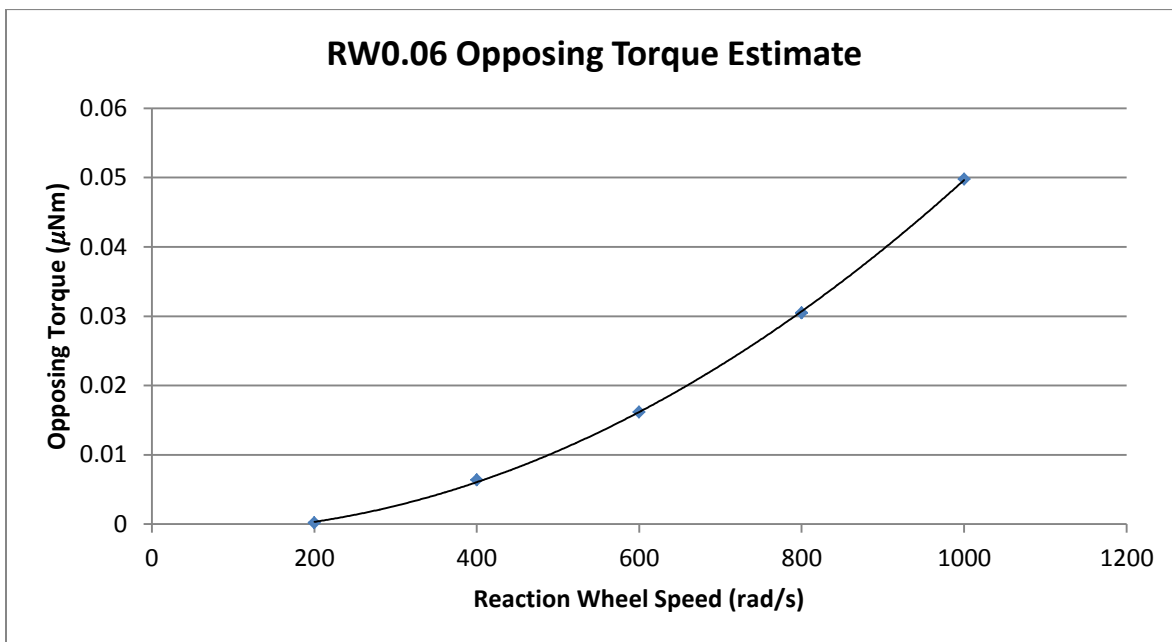


Figure 3-10: RW0.06 Opposing Torque Estimate

## 3.4.6. DAC Box

The Digital to Analog Converter (DAC) Box is a test where the wheel controller actuates its drive stages to the motor windings in open loop. This is essentially the final output where the digital to analog conversion is performed between the microcontroller and an analog output signal to the drive stages. The test actuates a set of open loop DAC commands which drive the reaction wheel motor at a maximum and only hardware limited output. The result is a torque response versus the speed at different voltage levels against a power contour plot.

The RW0.03 reaction wheel was tested showing the results in Figure 3-11. The results showed a very clear behaviour in the second and fourth quadrant where the motor did not enter the regenerative zones. This had also been confirmed by external current measurements showing no regeneration. The plot also showed the maximum power consumed across the speed envelope given a constant voltage and power tracking in first and third quadrant. This test confirmed the power contour plot and the underlying estimated motor parameters. It also confirmed that during DAC commands the motor will not enter into regeneration. Although DAC mode will not be used on board the spacecraft, it is an important step in verifying the characterization through open loop control and before closed loop control is tested.
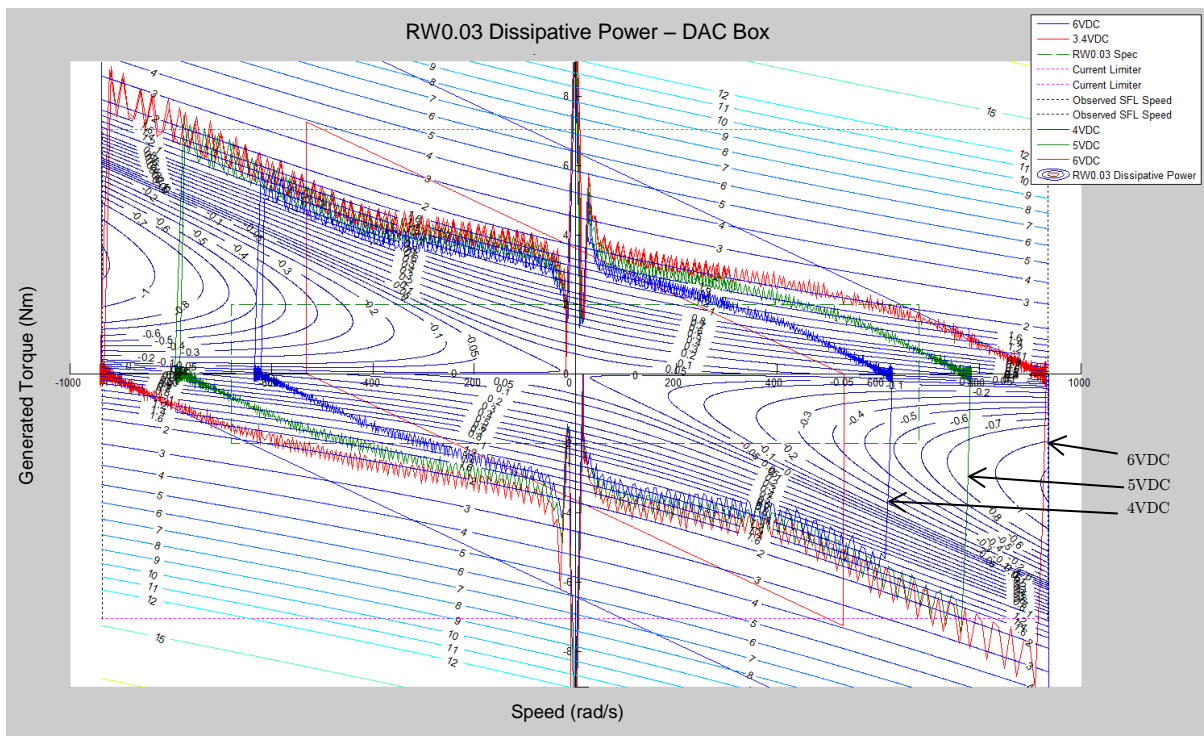


Figure 3-11: RW0.03 DAC Box Results

The RW0.06 reaction wheel DAC test results can be viewed on Figure 3-12. These results are only shown for the regenerative quadrant which is the second or fourth quadrant. The results do not differ between the described quadrants hence only one quadrant is shown. Given the DAC commands the motor does enter regenerations of almost $5W$ and at a DAC command of $0.3$. This shows that the previously described assumption that no regeneration will occur has been invalidated and the motor will show regeneration. The power tracking as with the RW0.03 was also confirmed with external current telemetry validating the characterization. The areas of interest from this test were the regeneration and increased torque jitter during regeneration.

The regeneration is of concern since it may exist during closed-loop control in the Speed and Torque Box tests. This behaviour would impact the spacecraft power system and/or reaction wheel if an appropriate shunt load is not integrated. The excessive torque jitter can provide diminished performance pending the operating speed of the reaction wheel during spacecraft operations. Further testing provided more detail on both behaviours in closed loop form which is the operating mode on board spacecraft.
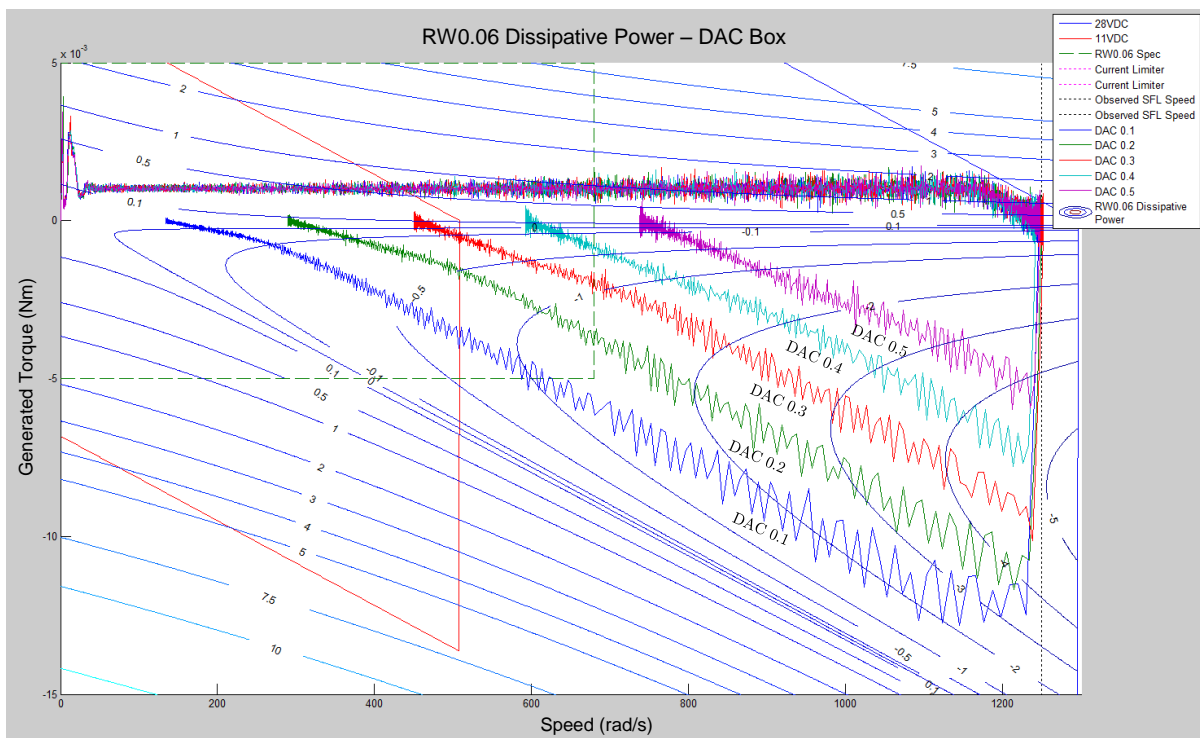


Figure 3-12: RW0.06 DAC Box Results

### 3.4.7.   Speed Box

The Speed Box test provided the first closed loop response in comparison to the DAC Box test. This test uses a dual loop control with two PID controllers. The reaction wheel operates a speed control loop at an approximate rate of $90Hz$ and a second power tracking control loop in the range of $190kHz$. These loops are controlled through user defined set points. The speed control loop set point commands the reaction wheel speed and the power control loop set point commands the maximum power the reaction wheel can consume in the first or third quadrant. This test shows the coupled behaviour between both controllers. The control mode can be used on board the spacecraft and is the next logical step from the DAC open loop control.

The RW0.03 reaction wheel results can be seen in Figure 3-13. Where again as with the DAC Box results there was no regeneration shown. Although there was a progressively worse torque jitter behaviour in the regenerative quadrants and a poor zero crossing behaviour. The power tracker can be seen tracking $0.7W$ in both the first and third quadrants which validates both the estimated motor parameters and the friction estimate. The validation comes from the measured response which is the plotted data matching the predicted power contour lines, voltage, torque and speed.



Figure 3-13: RW0.03 Speed Box Results
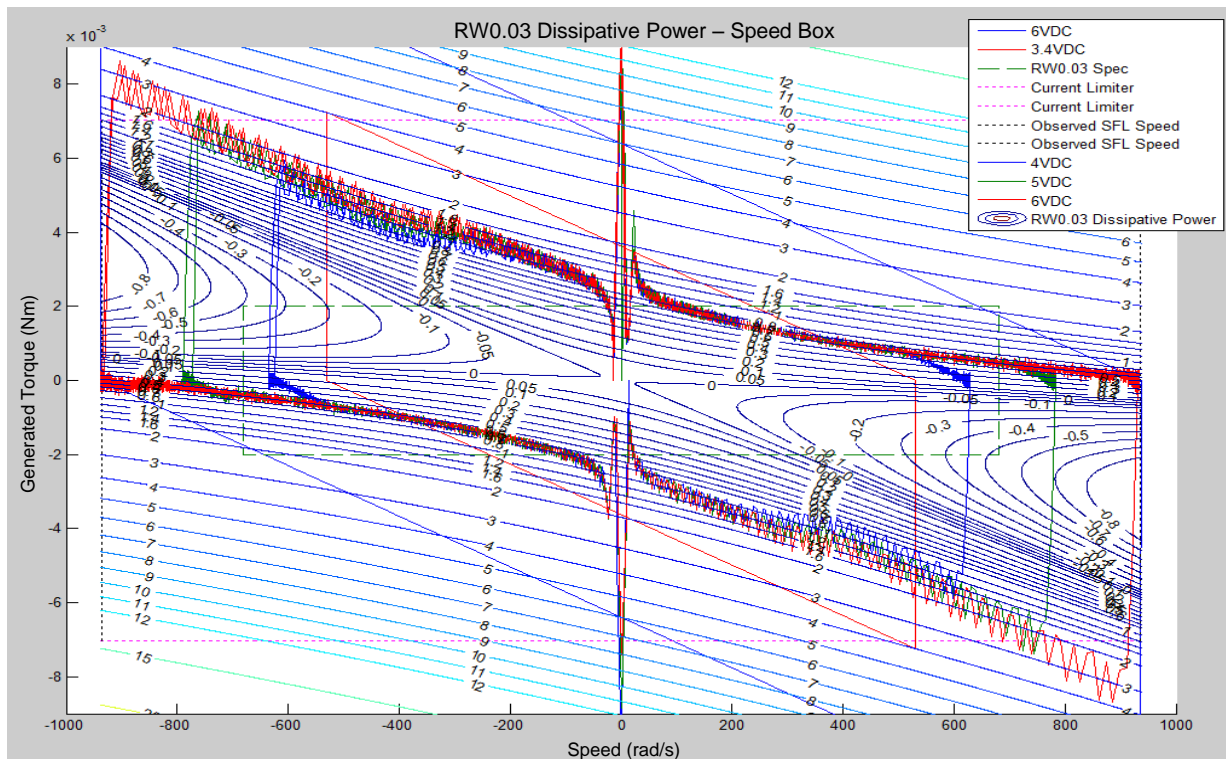
The RW0.06 as with the RW0.03 uses the same control loops. In fact both reaction wheels have identical microprocessors and only differ in the final MOSFET drive stages. Figure 3-14 shows results for RW0.06, which showed regeneration of almost $5W$, increased torque jitter in regenerative zones and large torque overshoot during zero crossings. The power controller can be seen tracking approximately $5W$ in the first and third quadrant which is as expected. The characterization was confirmed by matching power contour lines, voltage torque and speed response.
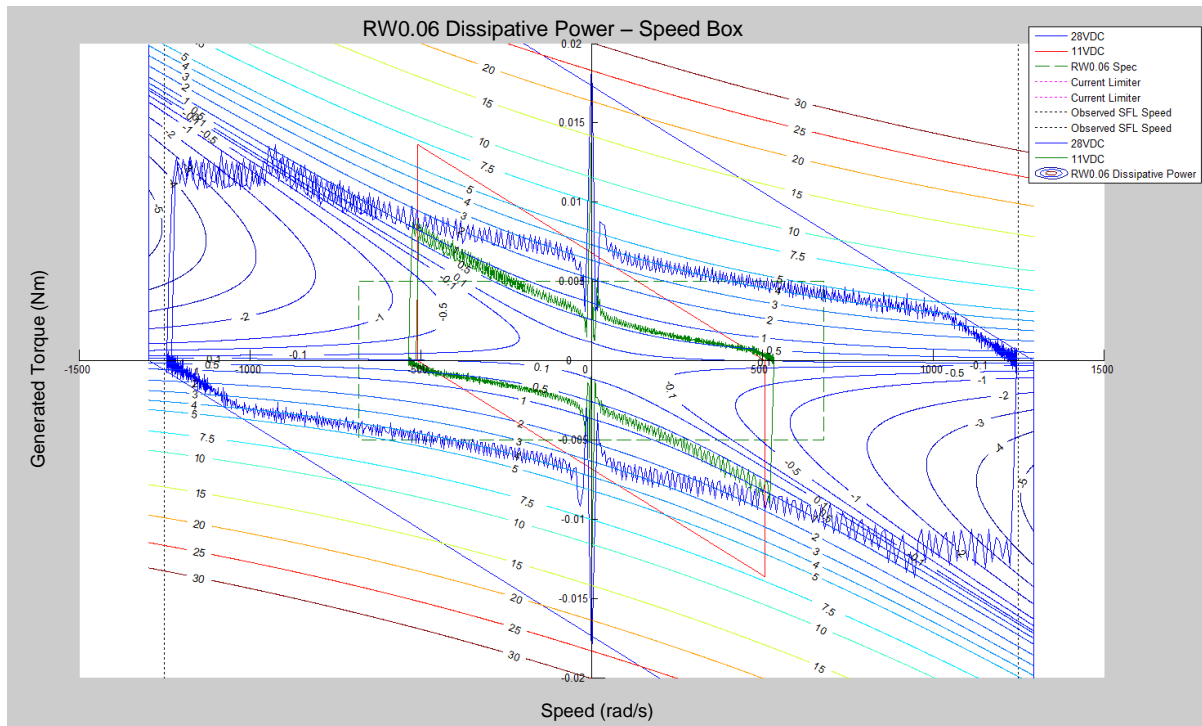


Figure 3-14: RW0.06 Speed Box Results

## 3.4.8.  Torque Box

The Torque Box provides a final result of the torque closed loop controller coupled with the power tracking controller given a variation in torque commands. This control mode is the same control mode that is used on-board the spacecraft. The controller essentially tracks an angular acceleration up to the maximum speed. The regenerative zones and torque behaviour across the reaction wheel speed range is of importance in this final confirmation of characterization.

The RW0.03 results can be seen in Figure 3-15. The results show clear regeneration during torque commands as opposed to no regeneration shown by the previous two tests. This regeneration was also confirmed with external current telemetry showing a

peak of $1.07W$. There is also an increase in torque jitter more than seen with the Speed Box during speed control in the regeneration zones. The zero crossing torque jitter has also increased. Overall the characterization had been confirmed and a regenerative behaviour of the RW0.03 had been discovered.
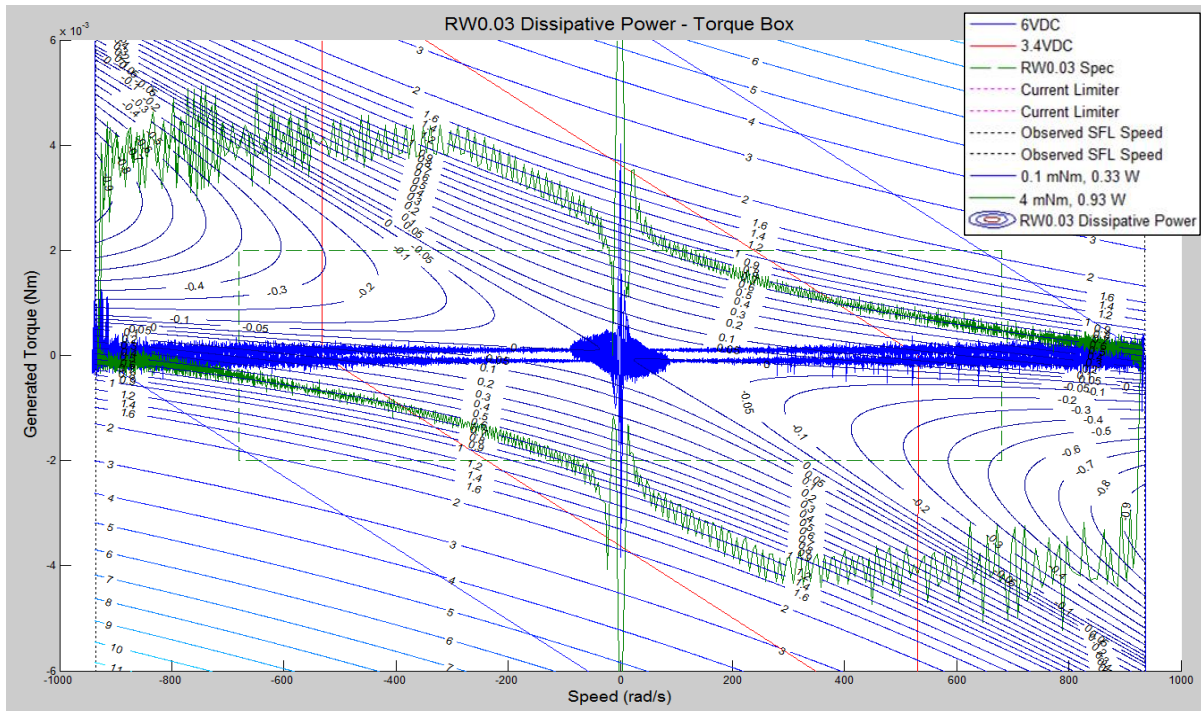


Figure 3-15: RW0.03 Torque Box Results

The RW0.06 reaction wheel Torque Box results can be seen in Figure 3-16. Where the same behaviour is seen with the regeneration and torque jitter as seen in two previous tests. Regeneration of a maximum of $4.5W$ was detected at the highest torques that would be expected on orbit. The characterization had been confirmed against the measured response of the reaction wheel.

The testing of both of the reaction wheel actuators had confirmed the following behavioural areas that need to be considered for acceptance testing:

- Regeneration impact on reaction wheel and/or power system
- Zero crossing torque response
- Torque jitter in regenerative zones
- Best operating zones for minimal torque jitter

The identified concerns are further investigated in later sections.
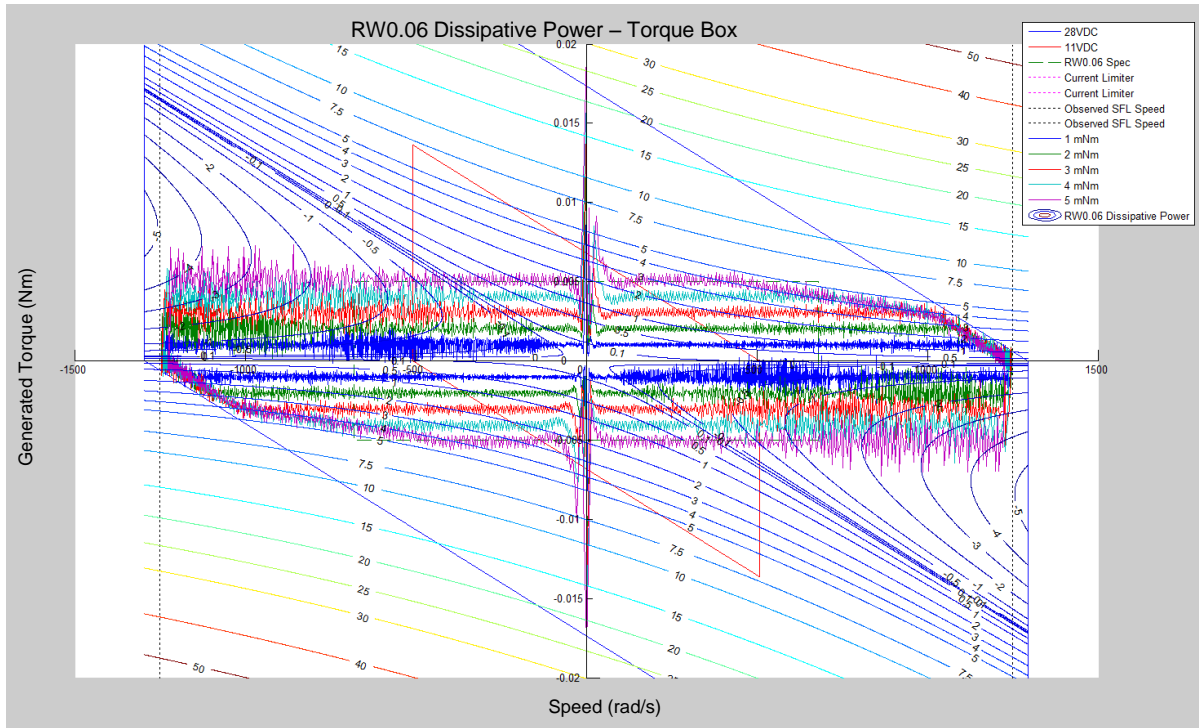
Figure 3-16: RW0.06 Torque Box Results

## 3.4.9.   Estimating Kt, Ke and R

During characterization of the reaction wheels the motor parameters were estimated and updated incrementally. As each test progressed from DAC Box to Torque Box the parameters received an update fine tuning the response. The relationship that provided for a quick determination of the parameters was the speed regulation constant discussed in Section 3.3.2. Anytime the DC motor was operating in the first or third quadrant and the speed increased to a point where the torque response was following the voltage limit line a line of constant slope was reached. This line typically continues to the speed axis intercept point which is at the maximum theoretical speed. The slope of this line is the speed regulation constant, where an example can be shown for RW0.03 in Figure 3-17. The results were obtained using the same method for RW0.06 and are not shown to minimize duplicity and are not shown.

The complete estimated parameters that define the characterization of the reaction wheel motors are provided in Table 3-2. These results are valid for all wheels since the motor design does not vary between the wheels. It should be noted that although these parameters provide an accurate representation of the motor behaviour these do

not represent the motor design parameters since the model used to describe the motor is single phase and not a 3 phase model as described in Section 3.3.2.
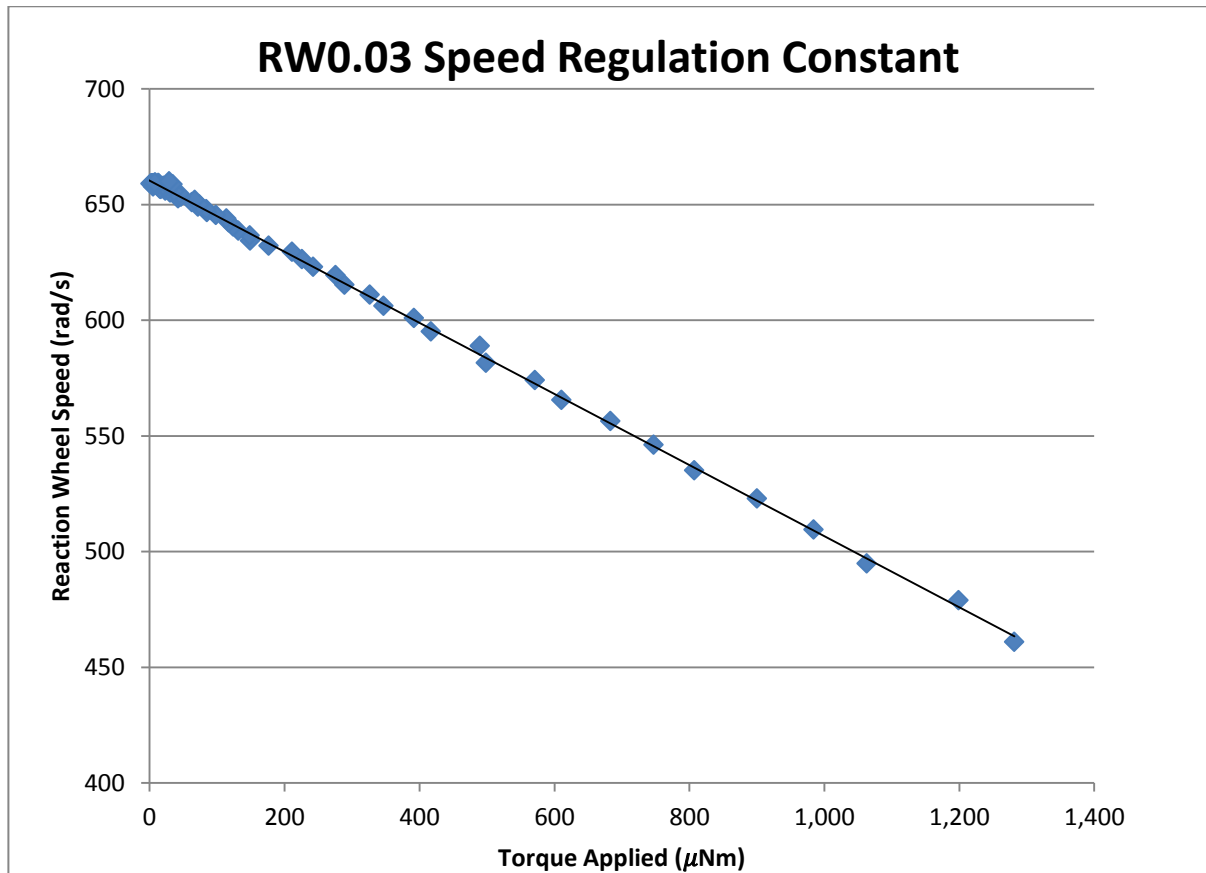


Figure 3-17: RW0.03 Regulation Speed Constant

Table 3-2: Reaction Wheel DC Motor Parameter Estimates

| Parameters | RW0.03 | RW0.06 |
|---|---|---|
| Voltage (VDC) | 3.5 | 28 |
| Duty Cycle (%) | 0.9 | 0.89 |
| Kt (Nm/A) | $5.3 \times 10^{-3}$ | 0.013 |
| Ke (Vs/rad) | $5.3 \times 10^{-3}$ | 0.013 |
| Max. Speed (rad/s) | 659.95 | 1247.6 |
| Winding Resistance ($\Omega$) | 4.32 | 13.02 |
| Speed Regulation Constant | $1.53 \times 10^5$ | $7.03 \times 10^4$ |

## 3.5    Torque Controller Improvement

The characterization of the reaction wheel motor showed that regeneration is present during torque operation of the both the RW0.03 and RW0.06 reaction wheels. The data also showed an increase in torque jitter. This section provides a more in-depth look at the torque jitter during regeneration and identifies actions that had been taken to remedy jitter increase.

### 3.5.1.    Torque and Speed Controller Comparison

The torque and speed controller responses were compared to shed light on the increased torque jitter behaviour during closed loop torque control mode. The results for the RW0.06 can be seen as an example in Figure 3-18. Where on the left is the speed controller showing regeneration and on the right is the torque controller in regeneration showing increased torque jitter and poor zero crossings. Similar behaviour was found in the RW0.03 reaction wheel with the exception of no regeneration in DAC and speed control mode.
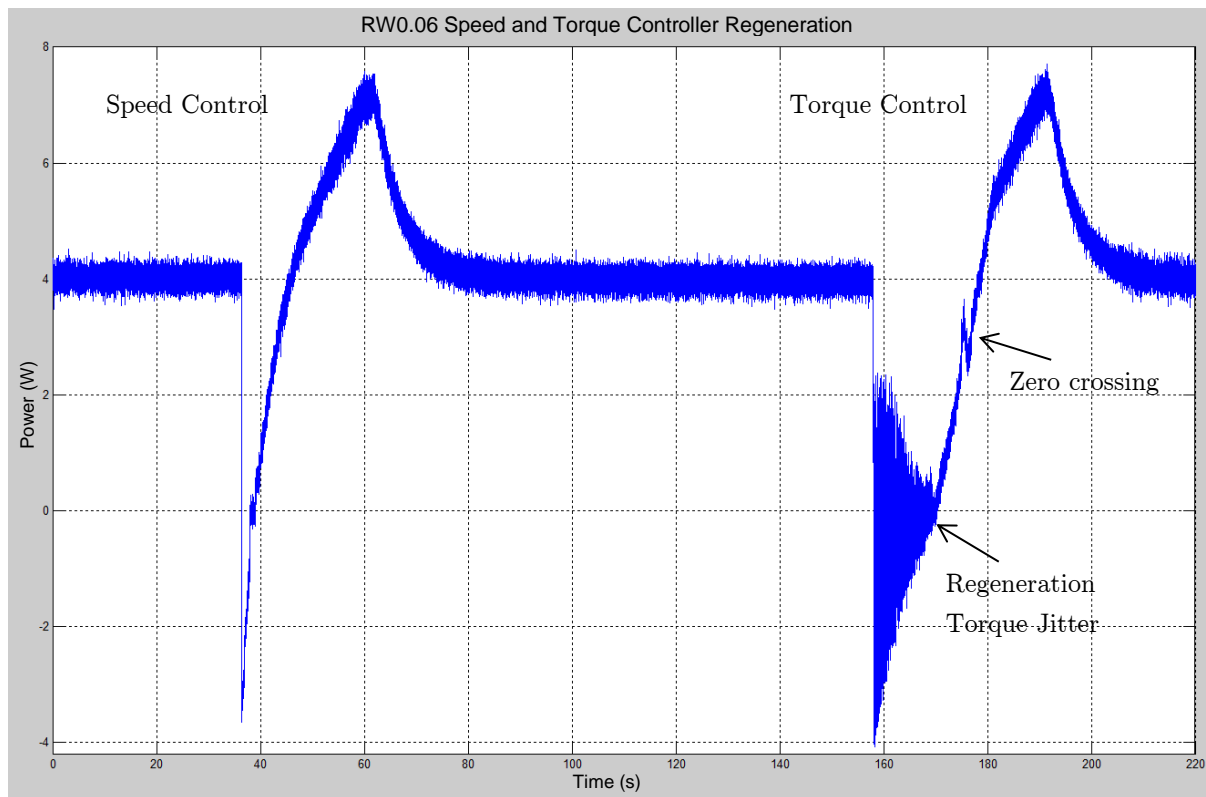


Figure 3-18: RW0.06 Torque and Speed Controller Comparison

A closer look at the torque jitter during torque control regeneration for RW0.03 can be seen in Figure 3-19, where a periodic pattern can be seen which suggests a control scheme used in the software of the reaction wheel. The reaction wheel does enter regeneration and seems to attempt to recover from regeneration.
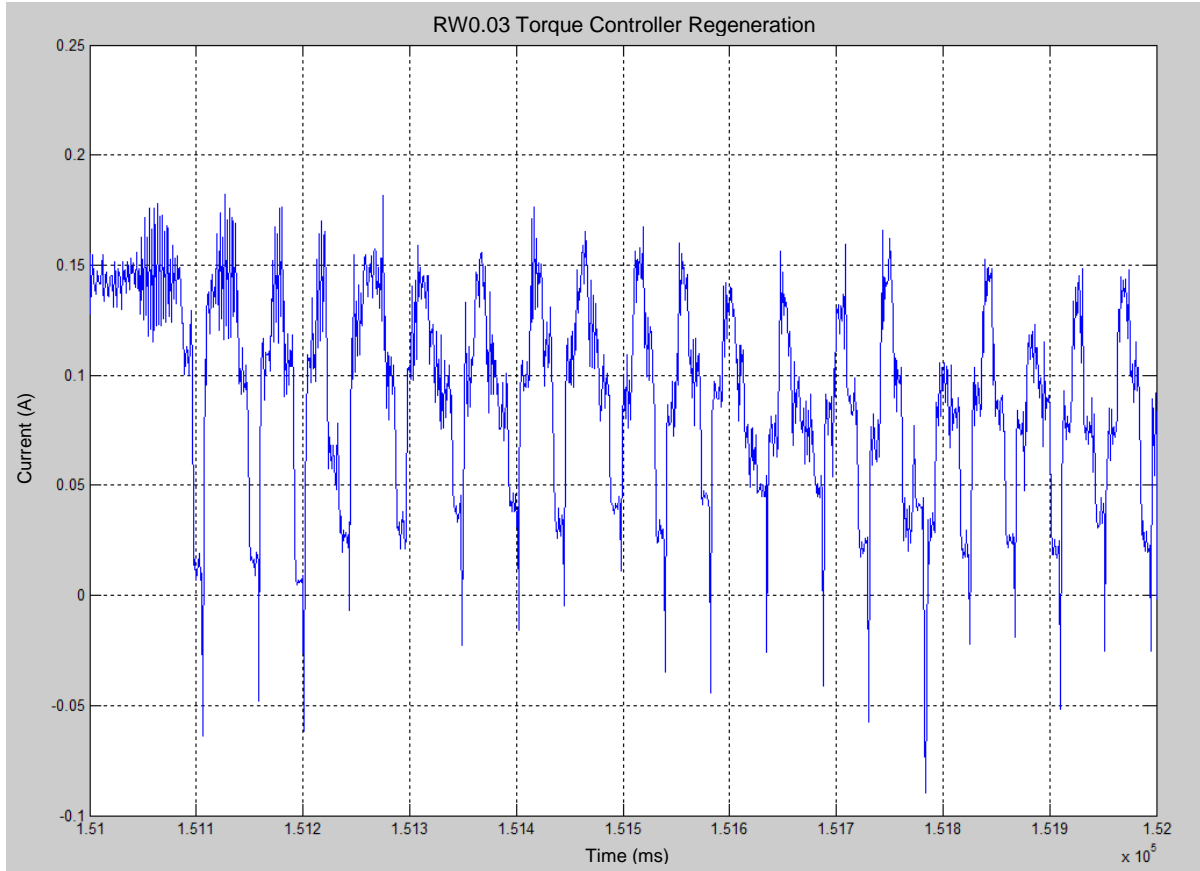


Figure 3-19: RW0.03 Regeneration During Torque Command

The RW0.06 reaction wheel result can be seen in Figure 3-20, showing similar behaviour to the RW0.03. Through further analysis of the reaction wheel software and hardware it was determined that the software invokes a regeneration control. This control behaviour is the resultant controller regeneration shown for RW0.03 and RW0.06 where the controller attempts to jump across the regeneration zone but fails during part of the cycle. This behaviour had been confirmed during testing with a variation of torques with external current measurements at $1kHz$.

The analysis also revealed that the zero crossings have poor performance due to the hall effect sensor speed estimation scheme used in the reaction wheels. The speed estimation essentially determines the time from one hall effect sensor to the next. As the motor approaches a zero crossing the time between sensor counts increases and the

state of the reaction wheel becomes undetermined. The PID responsible for controlling the torque begins to overshoot as the time between sensor counts increases. The torque controller undershoots once the zero point has been crossed and the time between the sensor counts decreases. Hence, the analysis thus far suggests that the zero crossings and increased torque jitter could be improved through a reaction wheel control software update. The degree of improvement and timeline of when it will be done had not been determined at the time of writing this thesis.
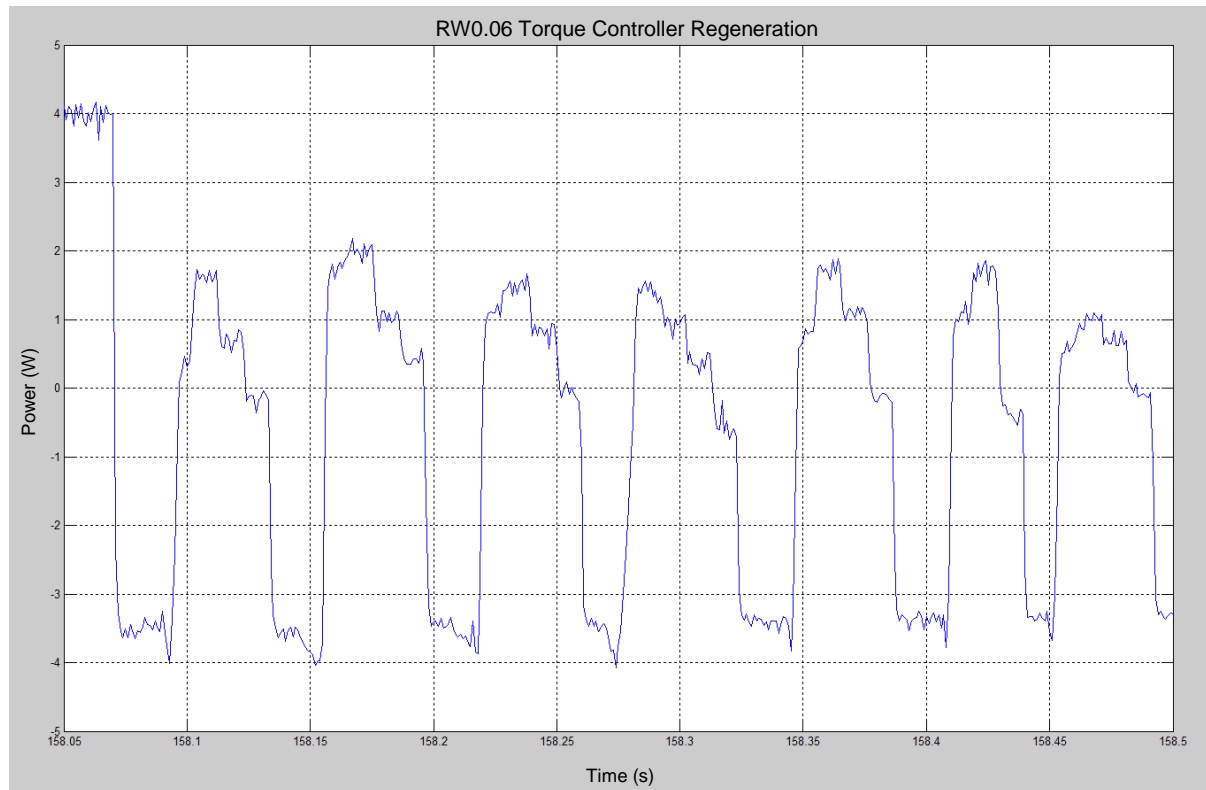


Figure 3-20: RW0.06 Regeneration During Torque Command

## 3.5.2.   Software Modification for Improved Torque Performance

Given the torque jitter during regeneration and zero crossing response a software update was in the works at the time of writing this thesis. This software update would provide an improved reaction wheel zero crossing response through the use of a new speed estimation scheme. The regeneration control would also be either removed or improved on. The reaction wheels used for characterization and acceptance testing in this thesis did not use this software update.

## 3.6    Regeneration Effect on Spacecraft Power Board

The characterization results predicted and verified the regenerative behaviour of the RW0.03 and RW0.06 reaction wheels. This result showed that if regeneration is invoked on-orbit during spacecraft operations the power bus of the spacecraft must absorb this regeneration safely. When considering the spacecraft power bus, two requirements were derived. The first requirement was in regards to the shunt size that would absorb the regeneration. The second was the requirement of the power switch for the reaction wheel being able to handle the regenerative current in the off state.

Through testing and not part of this thesis, it was verified that the spacecraft battery will adequately behave as a shunt and absorb the assumed maximum of $5W$ for the RW0.06 reaction wheel and $1W$ for RW0.03 reaction wheel. This analysis verified the first requirement.

The second requirement was verified against the operation of the power switch for the reaction wheel. Details of the setup and analysis are further described in the sections that follow.

### 3.6.1.    Power Board Principle of Operation

The spacecraft power board is responsible for all power generation, supply and storage on board the spacecraft. This system manages the battery and solar cell power generation through what is called a Battery Charge and Discharge Regulator using high efficiency methods for peak power tracking [23]. It also manages power consumption by devices and is capable of intelligently switching off loads in case of over current or to simply cycle power on a device. The overall implication is that for the spacecraft to be successful it must stay power positive and this system does just that. Hence, the importance of verifying requirements imposed by other systems becomes crucial for the success of the mission.

### 3.6.2.    Actuator Integration

Both types of reaction wheels tested in this thesis use a single port for combined power and communications. This port is typically connected directly to the power board which separates the power feed to the connector from the communication feed. The power feed is then connected to a dedicated switch on the power board. This switch can be a simple MOSFET or it could be more complex with added circuitry of over current protection [23]. The power board has the ability to switch the device on and

measure its power consumption. It is important to realise that past the on/off switch for a reaction wheel, all devices connected to the power bus share that power. The implication is that if a device produces noise all other devices must be able to mitigate this noise.

### 3.6.3.   Regeneration Test Setup

The test was performed using a sample spacecraft power board in a configuration with the reaction wheel as would be integrated on board spacecraft. A DC power supply was used to supply a bus voltage. Current readings were obtained through telemetry from the reaction wheel and the power board. The test setup consisted of the RW0.03 and RW0.06 reaction wheel, shunt resistors, power board, DC power supply, windows PC and oscilloscope.

The reaction wheel was placed into a state from which once power cycled would produce maximum regeneration. This typically meant spinning up the reaction wheel to a maximum speed and applying a reverse torque at which point the power board switch was turned off. Throughout the test, the current and voltage telemetry was being recorded

### 3.6.4.   Regeneration Results

The results can be broken down into three individual events which can be seen on Figure 3-21. Each event is composed of a voltage and current. The current can be either flowing to or from the reaction wheel. The state of the wheel is determined as a function of voltage and current. The reaction wheel is commanded by a DAC command of 0.3 which was previously shown in Section 3.4.6 to produce maximum regeneration. Only reaction wheel RW0.06 results are shown since this reaction wheel produced the most regeneration and represented the worst case scenario.

The first event shows the command sent to the reaction wheel and then the power switch turned off. The rise in voltage (yellow line) above the initial voltage and the negative spike in current (pink line) show that the regenerated current was flowing across the body diode of the switch (MOSFET) to the spacecraft bus. This continued until the reaction wheel generated voltage dropped back down to the magnitude of the initial bus voltage.

The second event is the voltage continuing to drop below bus voltage and until the microprocessor loses power at $4VDC$. The current shows regeneration that is decreasing progressively. The current is being sunk by a local zener diode that is part

of the local switch circuitry. This generated a requirement for the zener diode to ensure that it can handle the amount of power in this configuration. Testing of zener diode and verification against manufacturers specifications showed that the power levels are well within tolerance for nominal operation.

The third and last event shows that the voltage has diminished to almost zero and that the opposing torque is greater than any regenerated current. In this event the reaction wheel microprocessor is unpowered and the reaction wheel is coasting down under its own friction.
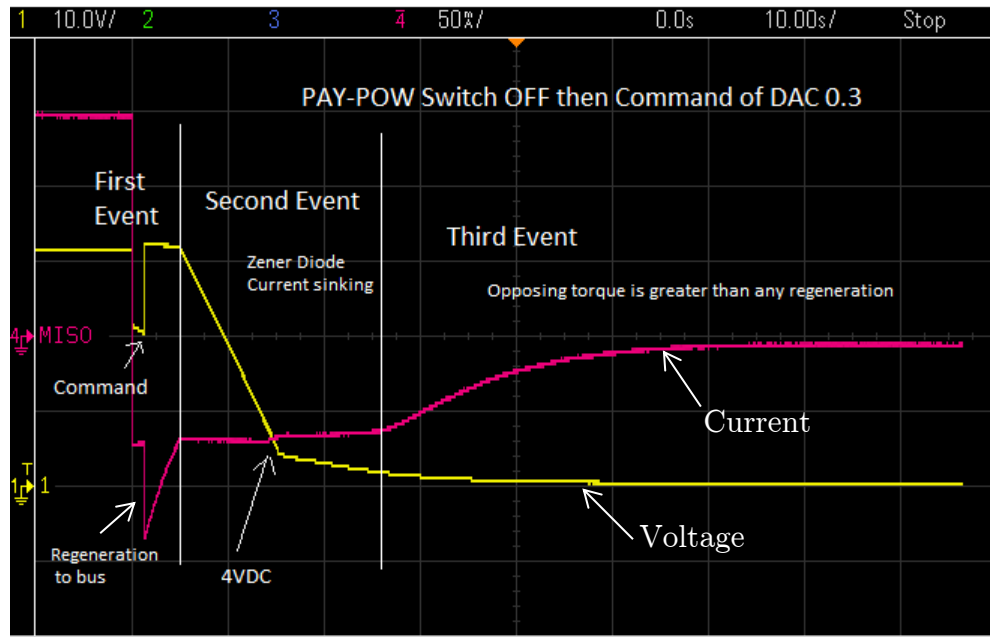


Figure 3-21: Reaction Wheel Power Switch Test

### 3.6.5. Summary of Results

In summary, the analysis of the test results had shown that the power board can absorb the worst case regeneration of approximately $5W$. This was confirmed with the reaction wheel power switch on and off. No additional shunt resistor was required in addition to the battery during regeneration. The impact of the regeneration that was identified in motor characterization has been assessed and retired through testing.

## 3.7   Safe Operation

The operation of the reaction wheel needs to be safely performed on board the spacecraft and during testing. In the previous section the safe operation of the reaction wheel on board spacecraft was confirmed with the testing of the power board. This section describes a safe method that was used for all ground testing of the reaction wheels.

### 3.7.1.   DC Motor Regeneration

The regeneration that is generated from a reaction wheel must be externally absorbed such that the regenerative current does not flow back into the reaction wheel. This is critical since the reaction wheels drive stages can be easily damaged if enough reverse current is absorbed. This damage may not be immediate and it could become evident through diminished performance on one of the drive stages. The overall effect would be a drastic reduction in torque control performance. Hence, it is best practice to avoid regeneration through the use of an external shunt. The regeneration that the shunt must be rated for is:

- $1W$ for RW0.03
- $5W$ for RW0.06

### 3.7.2.   Shunt Resistor Sizing

The shunt resistor is sized for the peak regenerative power of the device. In addition, a consideration had to be given if more than one reaction wheel would be tested at a time. Due to power supply limitations and communication interface best practice described in Section 3.4.4 a single wheel test was deemed adequate. This meant that each wheel would have its own shunt resistor with its own communication interface operating at the $60Hz$ polling frequency. This configuration would in effect maximize protection against regeneration and maximize the communication bandwidth.

The selection of shunt resistors for the RW0.03 reaction wheel is shown in Table 3-3, while the selection of shunt resistors for RW0.06 reaction wheels is shown in Table 3-4. The final chosen resistor configuration was:

- RW0.03: $10\,Ohm$ resistor with a $5W$ rating for 1 wheel
- RW0.06 $20\,Ohm$ Resistor with $50W$ rating for 1 wheel

More specifically, the values of resistance and power rating were obtained by comparing the amount of regenerative current at different voltages that a resistor

would have to absorb as shown by the shunt resistor sizing tables. In addition the configuration of multiple and single wheels on the same bus was compared. For both the RW0.03 and RW0.06 the critical metric that must have been met was that the power supply current must be greater than the regeneration current. The final resistor choice was based on power supply availability and a ~15% safety margin which accounted for the regenerative current as can be seen in the provided results.
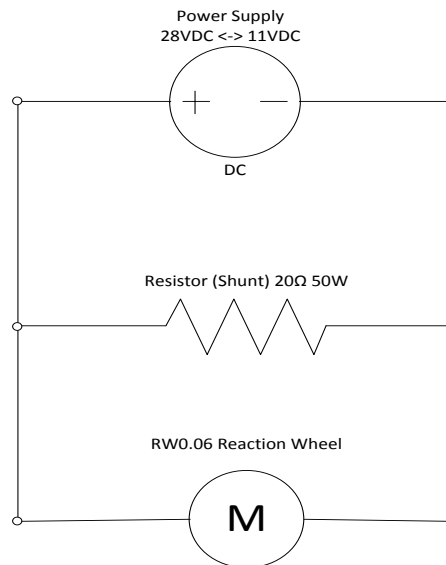


Figure 3-22:  Reaction Wheel Safe Setup Example

The shunt resistor connection is in parallel to the reaction wheel and DC power supply. Figure 3-22 shows the configuration for the RW0.06 reaction wheel. The RW0.03 reaction wheel has the same configuration except for the DC power supply and shunt resistor rating being as per Table 3-3.

Table 3-3: RW0.03 Shunt Resistor Sizing

| RW0.03 Reaction Wheel Shunt Resistor Sizing | | | | |
|---|---|---|---|---|
| Parameters | 1 - Reaction Wheel | | 6-Reaction Wheels | |
| Regeneration Power (W) | 1 | | 6 | |
| Operating Voltage (VDC) | 3.4 | 6 | 3.4 | 6 |
| Regeneration Current (A) | 0.29 | 0.17 | 1.76 | 1.00 |
| Required Resistance (Ohm) | 11.56 | 36.00 | 1.93 | 6.00 |
| Chosen Resistor (Ohm) | 10 | 10 | 1.5 | 1.5 |
| Power Supply Current for Resistor (A) | 0.34 | 0.60 | 2.27 | 4.00 |
| Power Rating for Resistor (W) | 1.16 | 3.60 | 7.71 | 24.00 |

Table 3-4: RW0.06 Shunt Resistor Sizing

| RW0.06 Reaction Wheel Shunt Resistor Sizing | | | | |
|---|---|---|---|---|
| Parameters | 1 - Reaction Wheel | | 4-Reaction Wheels | |
| Regeneration Power (W) | 5 | | 20 | |
| Operating Voltage (VDC) | 11 | 28 | 11 | 28 |
| Regeneration Current (A) | 0.45 | 0.18 | 1.82 | 0.71 |
| Required Resistance (Ohm) | 24.2 | 156.8 | 6.05 | 39.2 |
| Chosen Resistor (Ohm) | 20 | 20 | 5 | 5 |
| Power Supply Current for Resistor (A) | 0.55 | 1.40 | 2.20 | 5.60 |
| Power Rating for Resistor (W) | 6.05 | 39.2 | 24.2 | 156.8 |

### 3.7.3.   Verification of Safe Operation

The operation of the reaction wheel with the shunt resistor had been verified with external current measurements. The current flow was confirmed to always be away from the reaction wheel, which meant that the path of lowest resistance was the shunt. This configuration was also monitored for temperature as to make sure that excessive heating is not generated. This work established a verified method of safely ground testing of reaction wheels.

## 3.8   Typical Acceptance Test

All analysis shown up to this point of this chapter has provided for the foundation necessary to perform acceptance testing. The reaction wheel motor characterization has established at what speeds the reaction wheel can attain minimum torque jitter. The communication interface analysis has provided the highest and most reliable data polling frequency providing for maximum data resolution. The regeneration analysis has ensured safe testing of reaction wheels. In summary, this section will provide an overview of the acceptance test plan and sample results for the RW0.03 and RW0.06 reaction wheels.

The acceptance testing was performed for a number of missions under development at the Space Flight Laboratory. These missions were BRITE-Canada, AISSat-2, CanX-4/-5 and NEMO-AM. In total 21 RW0.03 and 4 RW0.06 reaction wheels were tested and verified against requirements. Typically the acceptance test is catered towards the requirements of a particular mission.

The acceptance testing is divided into three sections: nominal performance, torque performance, and operation over temperature. The nominal performance section verifies that the reaction wheel is in fact operating as it should in terms of the standard parameters such as speed noise, power consumption and damping coefficient. This section is composed of the following tests:

- Burn-in
- Short Form Functional Fest (SFFT)
- Speed Noise Test
- Power consumption

The torque performance section is comprised of a variety of torques tests. These tests are established as a function of requirements. The input is the different speeds from which the reaction wheel will be applying a torque. The output is a number of torque metrics including torque jitter. The operation over temperature uses tests from previous two sections at different temperature plateaus. The next section will begin with a description of the tests in a sequential order with sample results.

## 3.8.1.   Burn-in

The burn-in is a method of breaking-in the reaction wheel. This is performed initially upon the receipt of the reaction wheel and prior to any actual testing. The burn-in is comprised of a cycling of speed between the positive and negative speed envelopes over a period of $24\ hours$. The intent is to break-in the bearing and grease of the reaction wheel. This is intended to reduce the initial friction to a lower and more constant friction response which is seen in post burn-in.

## 3.8.2.   Short Form Functional Test

The Short Form Functional Test (SFFT) actuates the reaction wheel through a set of commands and measures the response. This response is then compared against typical operational ranges. The test ensures that the reaction wheel is performing nominally as compared to accepted values. The test is comprised of the following sequence of commands:

- Maximum positive and negative speed with no power limiter
- Maximum positive and negative speed with power limiter
- Speed steps

- Torque steps

The data is collected and parsed using MATLAB. The typical results can be seen in Figure 3-23 for the RW0.03 and Figure 3-24 for the RW0.06 reaction wheel. In addition to the power, speed and torque comparison the MATLAB parser also determines the viscous damping coefficient using equation (3.14) which is derived from rundown data. The output either shows parameter checks passed or a fail if one or more parameters did not meets specifications. The damping coefficient is determined using:

$$B = \ln\left(\frac{\omega_2}{\omega_1}\right)\frac{-I}{t_2 - t_1} \tag{3.14}$$

where $B = $ Is the damping coefficient

$\omega_1, \omega_2 = $ Is the speed telemetry at two different data points

$I = $ Is the mass moment of inertia of rotor

$t_1, t_2 = $ Is the time stamp telemetry for the speed.
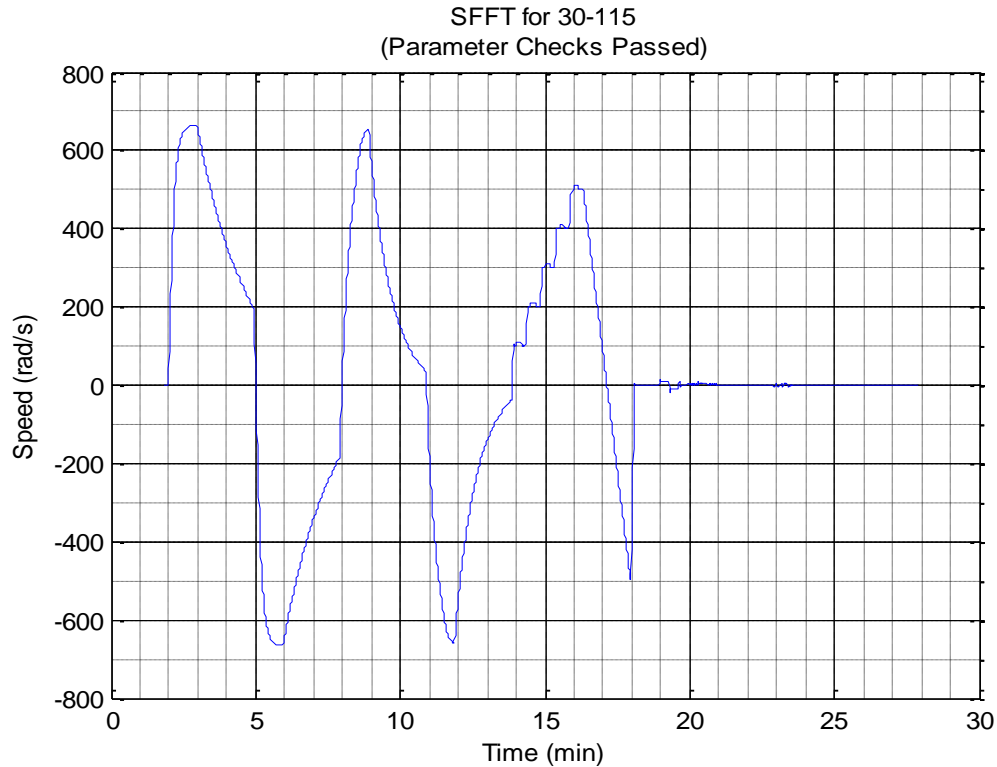


Figure 3-23: RW0.03 Short Form Functional Test
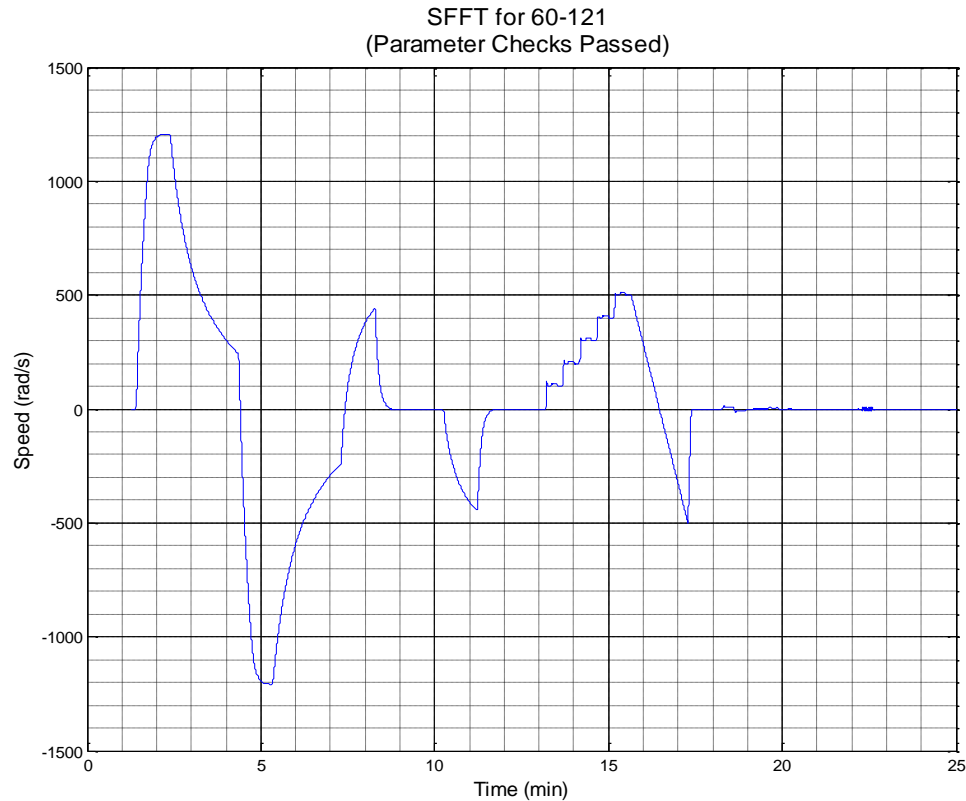
Figure 3-24: RW0.06 Short Form Functional Test

### 3.8.3.  Speed Noise and Power Test

The speed noise and power test provide the response of how well the speed controller is tracking the commanded speed and how much power it is consuming while operating at a particular speed. The commanded speed steps for each test are the same and are comprised of $100 \, rad/s$ increments. The speed noise test typically has a linear response for the positive and negative envelopes, while the power test has a quadratic response.

The captured test data is parsed using MATLAB which as with the SFFT flags any failed parameter checks. The expected results from the speed noise (standard deviation) test are a speed noise of less than $0.08 \, rad/s$ at the maximum speed of $+/- 500 \, rad/s$ for RW0.03 and $0.16 \, rad/s$ for the RW0.06 at a maximum speed of $+/- 1000 \, rad/s$. The results for both reaction wheels can be viewed in Figure 3-25 and Figure 3-27. A failed response can be seen in Figure 3-26 for a RW0.03 reaction wheel, where in post-test analysis it was determined that an unusual bias in a current sensor was causing abnormal behaviour.
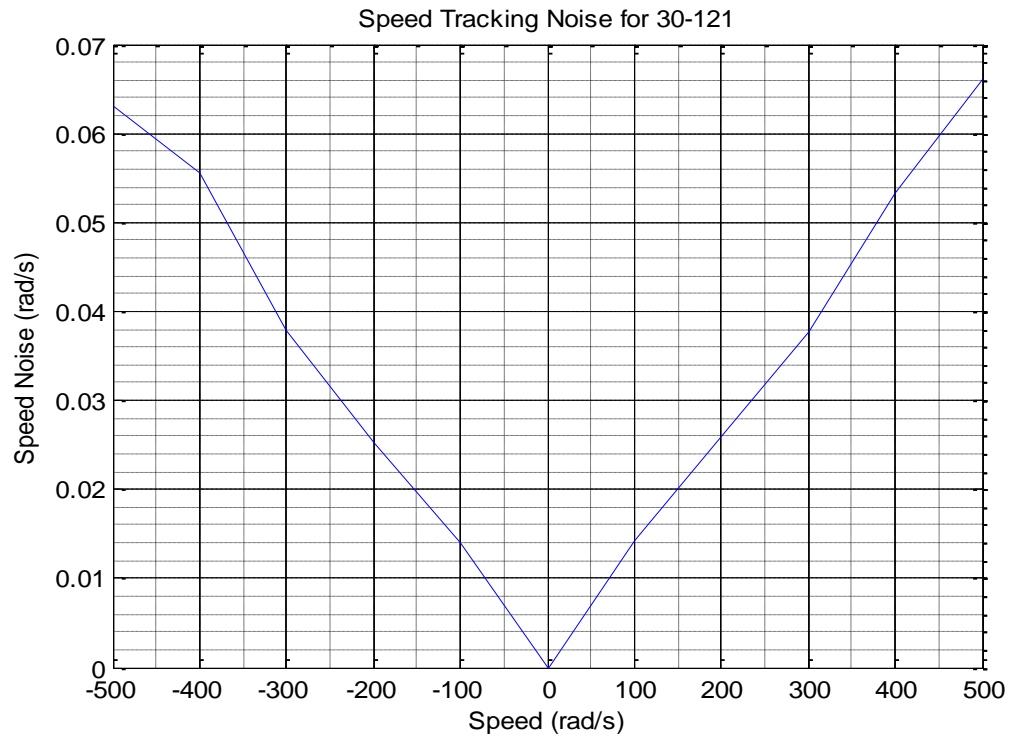
Figure 3-25: RW0.03 Reaction Wheel Speed Noise Results
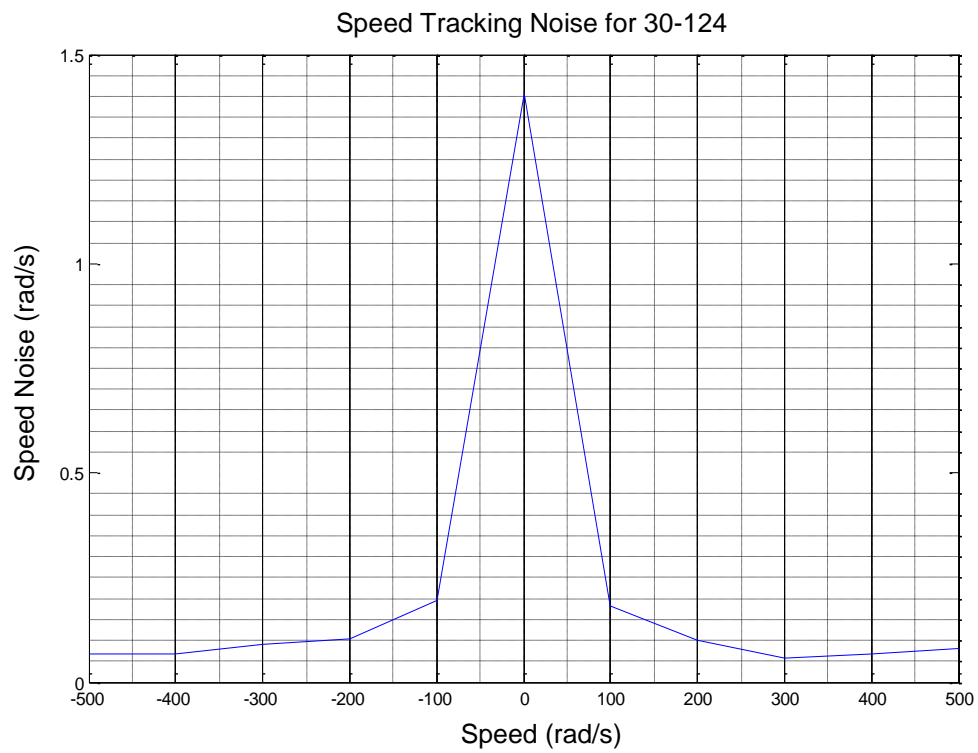


Figure 3-26: RW0.03 Reaction Wheel Speed Noise Results with Bias
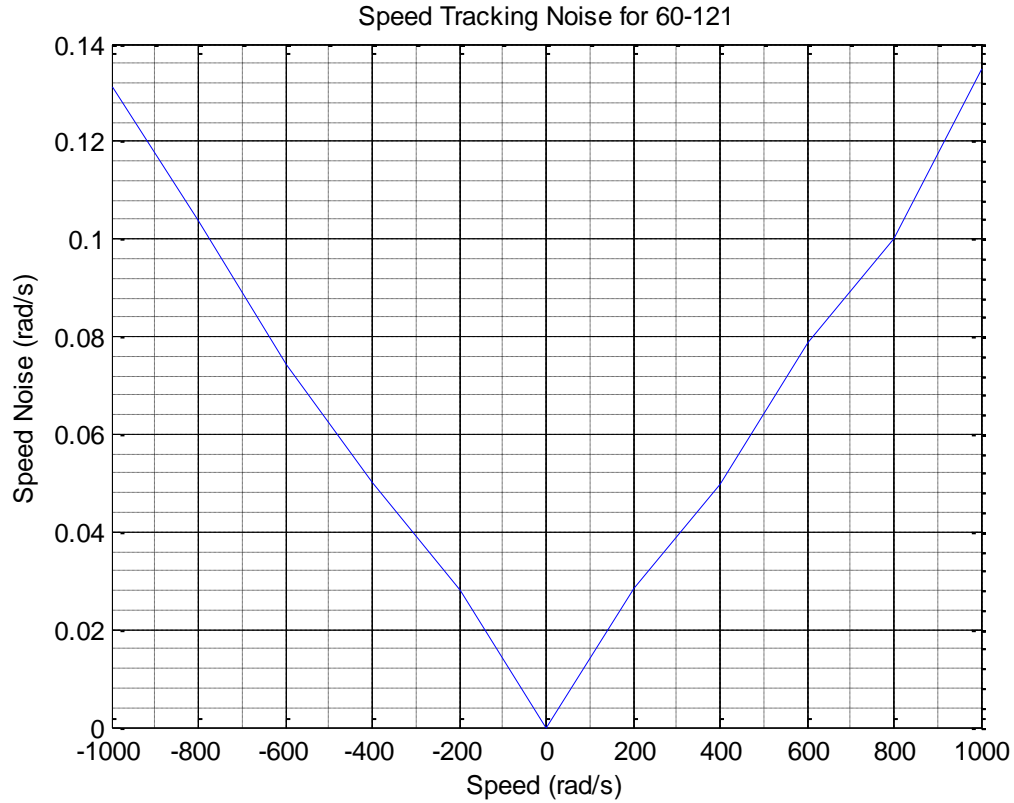
Figure 3-27: RW0.06 Reaction Wheel Speed Noise Results

The expected results of the power test are a power usage of less than $350mW$ at $+/-500\,rad/s$ for the RW0.03 and less than $2.5W$ at $+/-1000\,rad/s$ for the RW0.06. In addition, the nominal power consumption at zero speed and at no active control is also compared ensuring that the reaction wheel is not exhibiting abnormal power draws in its most basic operational states. Power consumption is also compared at a number of other speeds to ensure compliance. The results can be viewed in Figure 3-28 and Figure 3-29, both tests show valid results with the quadratic response.

It should be noted that when operating the reaction wheels in the safe configuration as described in Section 3.7, the power supply current will always show a current consumption equivalent to the consumption of the shunt and the reaction wheel together. The current consumption will increase anytime the reaction wheel DC motor is operating in the first or third quadrant and decrease if the DC motor is operating in the second or fourth quadrant (regenerating).
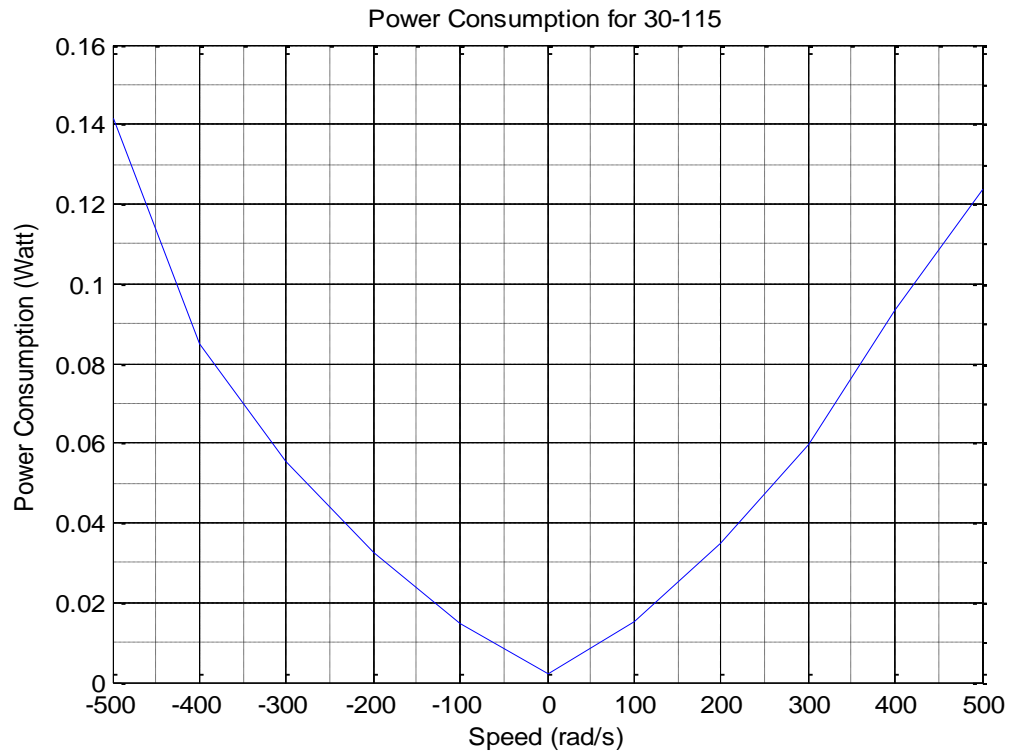
Figure 3-28: RW0.03 Reaction Wheel Power Consumption Results
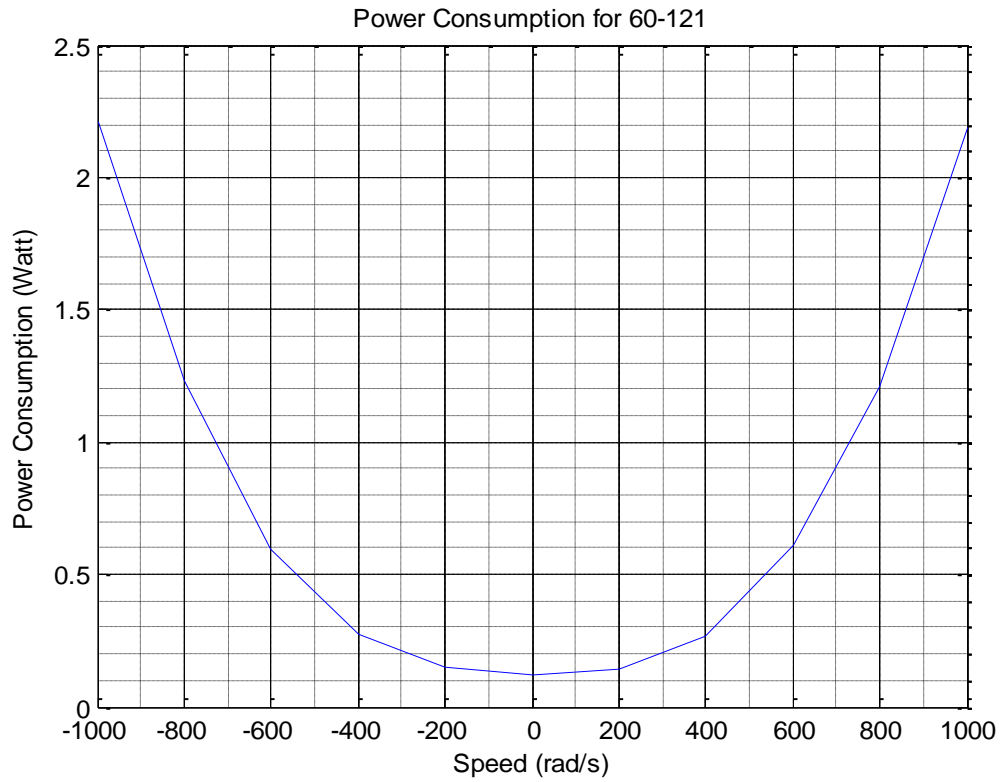


Figure 3-29: RW0.06 Reaction Wheel Power Consumption Results

### 3.8.4.    Nominal Performance Summary

The summary of the results obtained during the nominal performance section of the acceptance testing can be seen in the Table 3-5 for the RW0.03 reaction wheel and Table 3-6 for the RW0.06 reaction wheel.  The results show key metrics that are compared from each test between reaction wheels.  The expected values are the nominal operating ranges for the given test.  All tested reaction wheels passed the nominal test performance benchmark, with the only variation being a current sensor bias that was adjusted through a hardware replacement of the sensor.

Table 3-5: RW0.03 Nominal Performance

|  | Wheel 1 | Wheel 2 | Wheel 3 | Expected Values |
|---|---|---|---|---|
| Mass [g] | 181 | 181 | 181 | $185 \pm 10g$ |
| Damping Coefficient [Nms] | $6.36 \times 10^{-7}$ | $8.48 \times 10^{-7}$ | $5.34 \times 10^{-7}$ | $\sim 4 \times 10^{-7}$ to $3 \times 10^{-6}$ |
| Maximum Speed  at 4V [rad/s] | 652.83 | 623.59 | 634.14 | >600 |
| Power at 300 rad/s [mW] | 73.24 | 87.07 | 62.25 | < 120 |
| Max Power  Over Speed [mW] | 141.29 | 208.67 | 137.56 | < 350 |
| Noise @ 300rad/s     1-$\sigma$ [rad/s] | $3.79 \times 10^{-2}$ | $3.26 \times 10^{-2}$ | $3.57 \times 10^{-2}$ | $< 4 \times 10^{-2}$ |

Table 3-6: RW0.06 Nominal Performance

|  | Wheel 1 | Wheel 2 | Wheel 3 | Expected Values |
|---|---|---|---|---|
| Mass [g] | 230 | 231 | 232 | $225 \pm 10g$ |
| Damping Coefficient [Nms] | $1.23 \times 10^{-6}$ | $1.25 \times 10^{-6}$ | $1.35 \times 10^{-6}$ | $< 2.0 \times 10^{-6}$ |
| Maximum Speed  at 28V[rad/s] | 1100.8 | 1209.24 | 1235.08 | > 1100 |
| Maximum Speed  at 0.5W [rad/s] | 486.91 | 443.17 | 467.19 | > 300 |
| Max Power at 600 rad/s [mW] | 613 | 706 | 559 | < 800 |
| Noise @ 600rad/s  1-$\sigma$  [rad/s] | 0.075 | 0.079 | 0.074 | < 0.08 |

### 3.8.5. Torque Performance

This torque performance section of the acceptance testing provides torque results based on requirements. The test is defined by initial speeds and torques that the reaction wheels must apply. The initial speeds can be chosen from a requirement which is the case for this acceptance testing. Alternatively the initial speeds can also be chosen based on the reaction wheel DC motor characterization which shows the minimum torque jitter zones as a function of speed. In either case the applied torques must verify the provided requirements. Given the inputs, the test is then constructed such that the response is measured given the speeds and torques. The measured results are the torque bias, torque jitter mean, torque jitter standard deviation, torque jitter standard deviation of mean, FFT peak amplitude and FFT peak frequency. The described measured results are generated for each torque that is applied at a corresponding speed.

The torque bias ($\epsilon$) is a measure of how much the controller overshoots or undershoots the commanded torque. The torque jitter mean is the mean of the error in applied torque($\alpha$). Torque jitter standard deviation is the standard deviation of the torque jitter in applied torque($\beta$). The torque jitter standard deviation of mean ($\gamma$) is the standard deviation of the mean taken at one second intervals of the dataset, this is done since the controller on-board the spacecraft will only sample the telemetry at one second intervals. The FFT results provide a $30Hz$ bandwidth measurement with a peak amplitude ($\delta$) and frequency ($\varepsilon$) of the torque jitter response.

Table 3-7: RW0.03 Torque Results

| Torque ($\mu$Nm) | Initial Speed (rad/s) | $\epsilon$ ($\mu$Nm) | $\alpha$ ($\mu$Nm) | $\beta$ ($\mu$Nm) | $\gamma$ ($\mu$Nm) | $\delta$ ($\mu$Nm) | $\varepsilon$ (Hz) |
|---|---|---|---|---|---|---|---|
| 2 | 100 | 0.021 | -0.003 | 44.4 | 0.892 | 4.66 | 31.8 |
| 400 | 100 | 4.54 | 1.28 | 218 | 4.59 | 151 | 30.5 |
| -2 | -100 | -0.022 | 0.023 | 43.6 | 0.894 | 5.3 | 22.4 |
| -400 | -100 | -4.52 | -1.28 | 224 | 4.78 | 120 | 30.5 |
| 2 | 300 | 0.013 | 0.129 | 153 | 2.98 | 18.1 | 27.2 |
| 400 | 300 | -83.6 | -27.7 | 320 | 159 | 204 | 0.02 |
| -2 | -300 | -0.016 | 0.08 | 149 | 2.88 | 16.7 | 26 |
| -400 | -300 | 82 | 27 | 317 | 155 | 199 | 0.02 |

Typical results are shown in Table 3-7 for the RW0.03 and Table 3-8 for the RW0.06 reaction wheels. Both tables show the torque response of the reaction wheels based on input speed and torque. Where for the RW0.03 reaction wheel the requirement was set on the torque jitter standard deviation of mean ($\gamma$) to be less than $1\,\mu Nm$ at an applied torque of $2\,\mu Nm$ and reaction wheel speed of $+/- 100\,rad/s$. For the RW0.06 reaction wheel the requirements were still being revised at the time of writing this thesis and hence the results were based on the preliminary test cases. The results did provide the torque jitter that can be obtained given the speed of $50\,rad/s$ and $300\,rad/s$ with torques of $+/- 60\,\mu Nm$ and $+/- 10\,\mu Nm$ to be acceptable.

Table 3-8: RW0.06 Torque Results

| Torque ($\mu$Nm) | Initial Speed (rad/s) | $\epsilon$ ($\mu$Nm) | $\alpha$ ($\mu$Nm) | $\beta$ ($\mu$Nm) | $\gamma$ ($\mu$Nm) | $\delta$ ($\mu$Nm) | $\varepsilon$ (Hz) |
|---|---|---|---|---|---|---|---|
| 10 | 50 | 0.214 | 0.554 | 121 | 10.1 | 27.7 | 3.23 |
| 60 | 50 | 1.18 | 0.562 | 129 | 8.3 | 23.2 | 3.83 |
| -10 | 50 | -0.186 | 0.222 | 95.7 | 11.4 | 27.7 | 2.49 |
| -60 | 50 | -1.15 | 0.509 | 68.3 | 14.7 | 17.8 | 0.56 |
| 10 | 300 | 0.172 | 0.437 | 283 | 9.51 | 27.7 | 26.3 |
| 60 | 300 | 1.15 | 0.358 | 276 | 6.63 | 27.3 | 30.4 |
| -10 | 300 | -0.221 | 0.021 | 281 | 6.58 | 30.6 | 22.6 |
| -60 | 300 | -1.19 | -0.185 | 251 | 4.98 | 31.5 | 30.9 |

## 3.8.6.   Operational Over Temperature

This part of the acceptance testing is composed of performing the nominal test and torque performance test at defined operational temperatures. The temperature profile is typically defined as the following temperature plateaus in sequence:

- Room temperature
- Hot temperature (Survival and Operational)
- Cold temperature (Survival and Operational)
- Cyclical between hot and cold temperature operational
- Room temperature

The test is performed to ensure that the nominal and torque performance are not significantly affected by temperature variations. All reaction wheels tested met the requirements outlined earlier through the complete temperature profile.

## 3.9  Summary of Contribution

The RW0.03 and RW0.06 reaction wheels are high-performance active attitude control actuators which are becoming more crucial for nanosatellite missions. Given the pointing requirements for recent missions this is the only type of actuator available that can provide fine pointing capability for the nanosatellite bus. The author's contribution with regard to this type of actuator was:

- Reaction wheel DC motor analysis, verification and characterization
- Communication interface characterization and verification
- Analysis of regeneration impact on spacecraft power system
- Reaction wheel safe operation due to regeneration
- Design of acceptance test plan for reaction wheels
- Detection of a current bias in RW0.03 reaction wheels
- Reaction wheel enclosure and communication harness design and implementation
- Acceptance testing of 25 reaction wheels with verification of requirements

### 3.9.1.  Future Work

It is envisioned that the future acceptance testing of the reaction wheel actuator will involve an external measurement of torque jitter. This is due to the current limitation which pertains to the telemetry being only representative of the controller response and not accounting for external sources of torque jitter. The reaction wheel torque disturbances can be broken down into the following categories:

- Mechanical disturbance
  - Rotor and Cage mass imbalance
  - Ball bearing sizing error
  - Bearing misalignment

- Control disturbance
    - Constant speed
    - Change in speed (Torque)

The current acceptance testing has provided a measure of the control disturbance as a measurement of torque jitter. Below Figure 3-30 shows an alternative method of measuring disturbances generated by the reaction wheel. This method consists of mounting a reaction wheel on a fixture that through the use of load cells is capable of resolving the generated reaction wheel disturbances in terms of torques and forces. The main advantage of this method is that it provides an external spectral measurement of the torques and forces generated by the reaction wheel. This type of acceptance testing has been previously used on NASA's Hubble Space Telescope reaction wheels [24]. The challenges of this type of method are that initial calibration is required to account for resonance and damping which can be difficult and time consuming to determine.
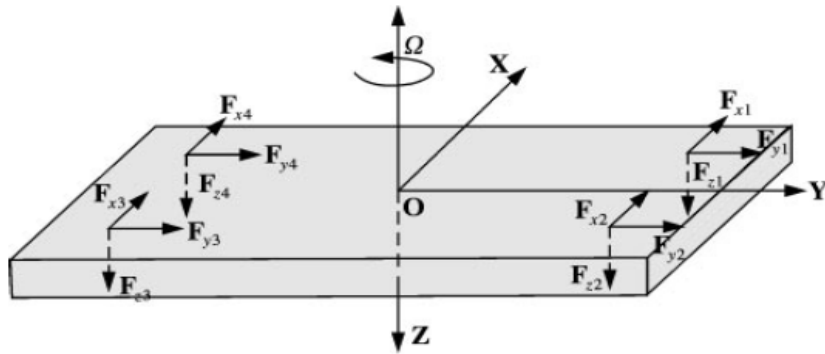


Figure 3-30: External Disturbance Measurement [25]

The results from the external disturbance measurement are shown on a Power Spectral Density plot (PSD). An example plot is shown in Figure 3-31, where the disturbance is shown as a function of reaction wheel speed and frequency. The response on the plot can provide insight into the following mechanical disturbance sources:

- Radial Translation
    - Rotor and cage mass imbalance
    - Bearing misalignment
- Radial Rocking
    - Ball sizing error
    - Bearing misalignment
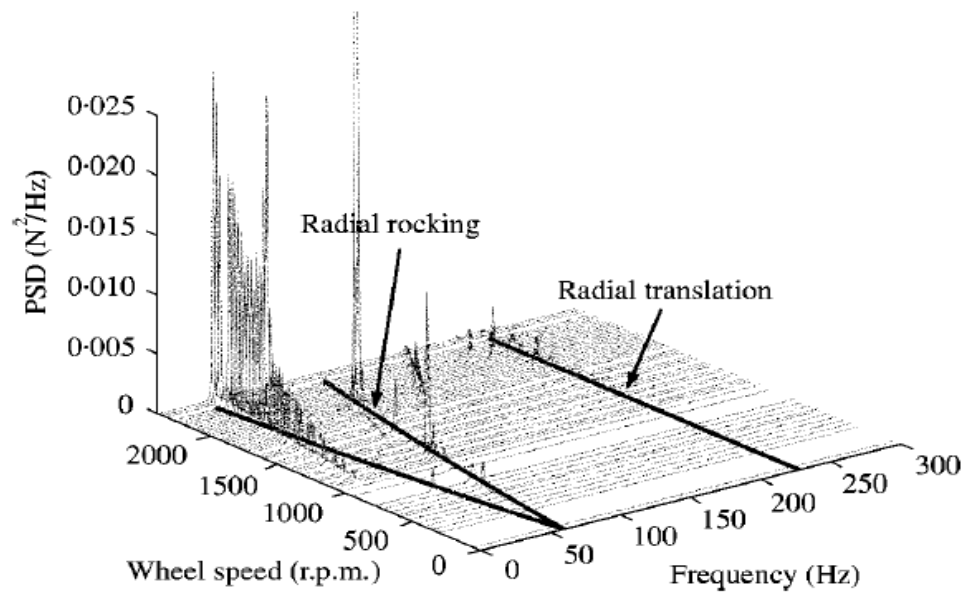
Figure 3-31: Possible External Disturbance Results [25]

Using a single axis accelerometer and measuring the disturbance generated from a RW0.03 reaction wheel has generated the results shown in Figure 3-32, which is an uncompensated result. This means that the measurement is not calibrated for resonance and damping.
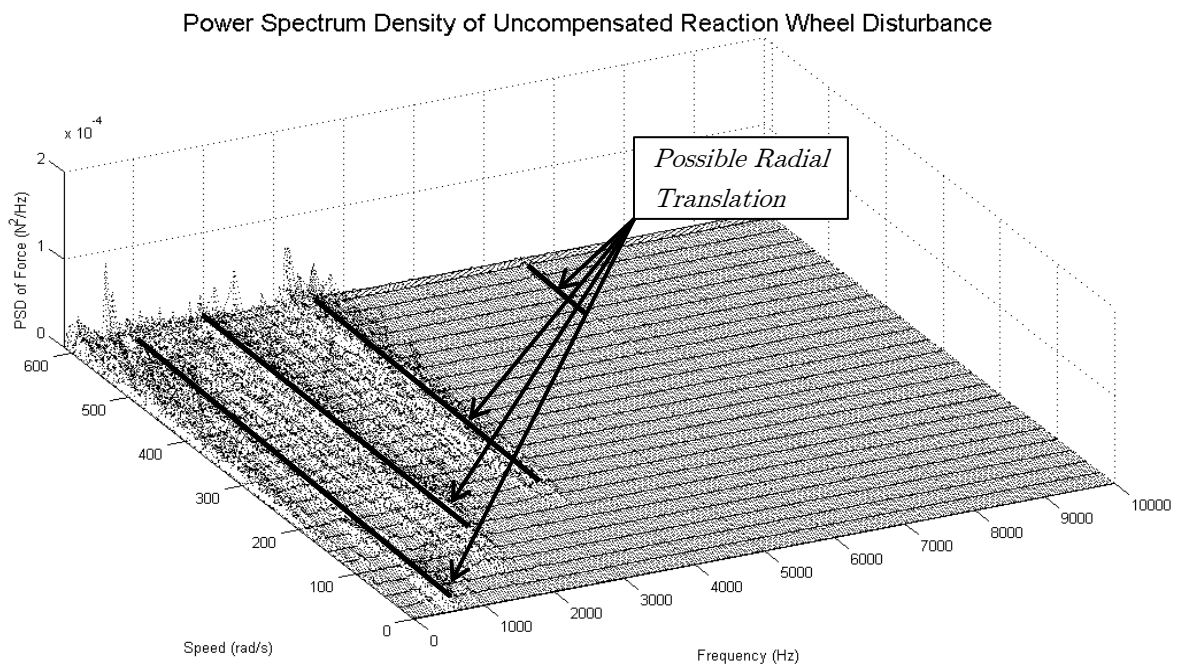


Figure 3-32: Power Spectrum Density Uncompensated Experimental Results

It can be suggested that the RW0.03 reaction wheel could have contributing mechanical disturbance due to radial translation which could indicate a rotor and cage mass imbalance and or bearing misalignment. It should be noted that the data was obtained using an uncompensated test setup which does not validate the magnitudes of the disturbance but does indicate that there could be external disturbances present.

The impact of these results on the spacecraft are that a reaction wheel acceptance testing might not capture all contributing torque jitter sources and hence the torque jitter obtained during acceptance testing may not be representative of the actual torque jitter. In an effort to mediate this it can be further suggested that the spacecraft should have a frequency based torque jitter requirement. This would aid in only measuring disturbances at frequencies that can impact the spacecraft bus and would also provide a complete external torque and force measurement of the reaction wheel actuator.

# Chapter 4

# Passive Magnetic Actuator

The passive magnetic actuator described in this chapter is a hysteresis rod. This type of actuator provides damping of spacecraft angular rotations which reduces the angular momentum of a spacecraft. The removal of energy from the spacecraft is possible due to a hysteresis effect of a ferromagnetic material. This chapter is broken down into two sections: the design process and acceptance testing of hysteresis rods. The design process is based on what was done for the Munin Nanosatellite [26] and the Nanosatellite Tracking Ships (NTS) [27]. The hysteresis rod acceptance testing is based on acceptance testing performed for the Munin Nanosatellite but adapted to NTS type missions at the Space Flight Laboratory (SFL). This provides a generic example of the design and testing of hysteresis rods for the Generic Nanosatellite Bus (GNB) type of spacecraft.

## 4.1 Magnetic Hysteresis Background

In magnetic hysteresis there are a number of relationships that are used to describe the overall behaviour of the material response or magnetic flux density $B$ to a magnetic field strength input $H$. The overall relationship is shown by the following equation (4.1):

$$B = \mu H \tag{4.1}$$

where $B =$ Magnetic flux density with units in $T$

$\quad\quad \mu =$ Magnetic permeability of a material with units in $\frac{Tm}{A}$

$\quad\quad H =$ Magnetic field strength input with units in $\frac{A}{m}$.

Where, $\mu$ is the magnetic permeability of a material and has a non-linear behaviour as a function of $H$ or magnetic field strength input as shown in Figure 4-1, where the nonlinear behaviour of magnetic permeability is shown.



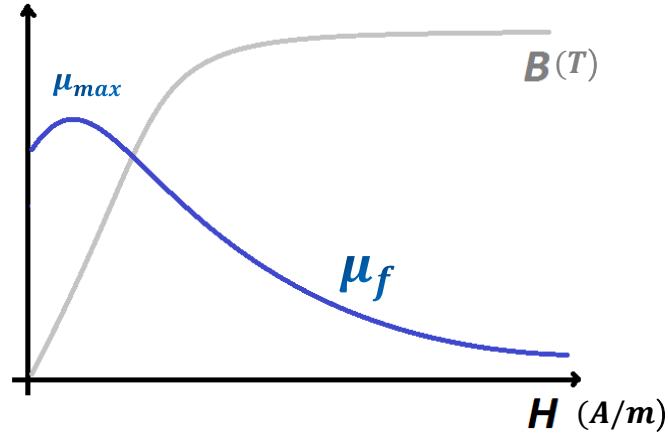Figure 4-1: Permeability of a Ferromagnetic Material

It is very important to realise that the magnetic field strength $(H)$ is the input into the system and that the chosen medium provides the particular permeability $(\mu)$ which yields a specific magnetic flux density $(B)$ or output. This is shown in Figure 4-2, where a sample $B - H$ response for a material is plotted.
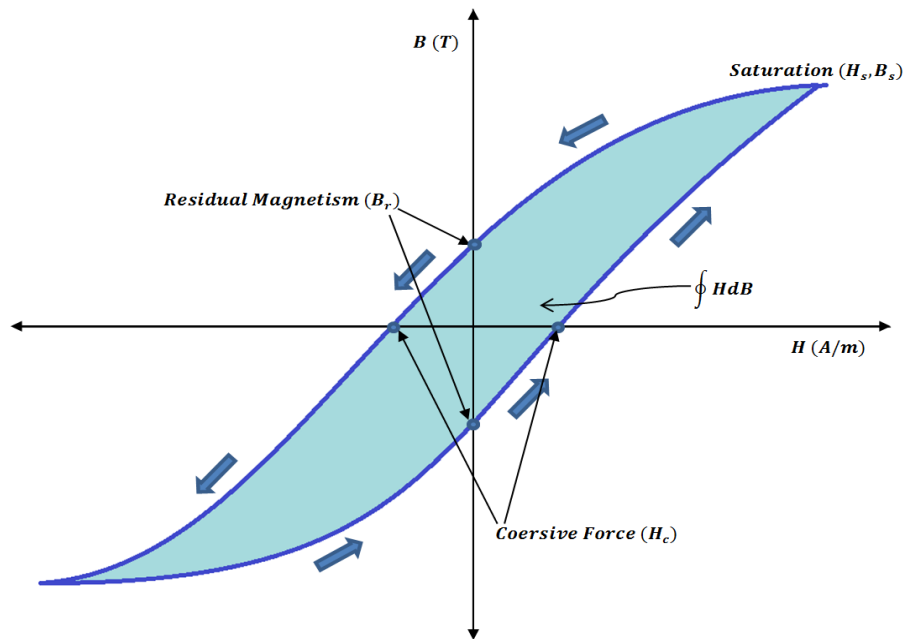


Figure 4-2: Magnetic Hysteresis Response

Explanation of key parameters that have been identified in Figure 4-2 are as follows:

- $H_c$ is the coercive force, which is the minimum magnetic field strength input needed to reduce the residual $B$ field to zero after input field is removed and the material was at saturation

- $B_r$ is the residual magnetic flux density after the $H$ input is removed

- $H_s$ is the magnetic field strength needed to bring the material $B$ to saturation

- $B_s$ is the maximum magnetic flux density that the material can maintain as a function of $H$ input

- $\oint H dB$ is the area under the curve which corresponds to the amount of energy absorbed by the material through a hysteresis cycle

## 4.2   Design of Hysteresis Rods

The design process begins with a review of spacecraft that have utilized hysteresis rods and leads into a top down/bottom up requirement driven design. The review of previous spacecraft provides a baseline check of hysteresis rod parameters. The top down requirements are a function of the type of orbit that the spacecraft will be in and hence the magnetic field strength that the hysteresis rods will be saturated in. The bottom up requirements are a function of maximizing the distance of the hysteresis rods from an on-board permanent magnet, maintaining a perpendicular orientation of the rods to the magnet and sizing the rods as a function of relative position between the rods constrained by the spacecraft bus size.

The following Table 4-1 shows the spacecraft and hysteresis parameters that had been considered for Nanosatellite Tracking Ships (NTS):

Table 4-1: Design Points for NTS Based on Mission Scaling [27]

| Mission | Scaled dipole for NTS $Am^2$ | Scaled rod volume for NTS $x10^{-7} m^3$ |
|---------|------------------------------|------------------------------------------|
| Sapphire | 1.55 | 7.15 |
| Munin | 0.42 | 1.32 |
| LatinSat | 4.96 | 24.54 |

The following Table 4-2 shows the spacecraft and hysteresis rod parameters that were considered for the Munin spacecraft:

Table 4-2: Parameters of Hysteresis Rods of Various Satellites [26]

| Satellite | Total volume of rods, cm$^3$ | Rod material | Number of rods |
|---|---|---|---|
| Transit-1B | 200 | AEM 4750 | 8 |
| Transit-2A | 50 | AEM 4750 | 8 |
| Injun-3 | 50 | Permalloy | 22 |
| ESRO-1 | 12 | PERMENORM-5000 | 20 |
| Azur | – | – | 8 |
| TTS | 2.5 | AEM 4750 | 20 |

Hysteresis rod design captures the following parameters that affect the damping produced by the hysteresis rods:

1. Material properties and heat treatment
2. Volume
3. Arrangement on spacecraft bus
4. Elongation (L/D)

## 4.2.1. Material Properties and Heat Treatment

As previously mentioned the top down requirement is typically the magnetic field strength that the hysteresis rods would be exposed to. As an example for Munin the field strength was estimated to be $18.1\,A/m$ at the equator and up to $36.2\,A/m$ at the poles for a $700\,km$ orbit. Based on this information a material selection was made such that the coercive field is minimized while the area under the $B - H$ curve is maximized. This provided for maximum damping given the availability of a material. For an accurate estimate of the area under the curve the material would be tested ($B - H$ curve) at the magnetic field strength expected on-orbit. Below are shown the selections of materials for the Munin and NTS spacecraft.

Material properties that were chosen for NTS are shown in Table 4-3, showing a Nickel-Iron alloy. This is the same material that had been previously used by the Sapphire spacecraft shown in Table 4-1.

Table 4-3: Parameters of Nickel-Iron Alloy

| Initial Magnetic Permeability $\mu_{in}$ | Maximum Magnetic Permeability $\mu_{max}$ | Coercive Field $H_c$ (A/m) | Residual Flux $B_r$ (T) | Saturation Flux Density $B_s$ (T) | Saturation Field $H_s$ (A/m) |
|---|---|---|---|---|---|
| 12100 | 124000 | 2.86 | 0.96 | 1.49 | 795.77 |

Material properties that were chosen for Munin are shown in Table 4-4, showing a Molybdenum permalloy as the chosen material. The Munin spacecraft is of interest for NTS since its bus size and performance metrics are similar.

Table 4-4: Parameters of Molybdenum Permalloy of the 79NM sort [26]

| Initial magnetic permeability $\mu_{r\,in}$ | Maximum magnetic permeability $\mu_{r\,max}$ | Coercive force $H_c$, A/m | Saturation induction $B_s$, T |
|---|---|---|---|
| 60000 | 164000 | 0.96 | 0.74 |

The material properties can be altered through a heat treatment process which may improve the hysteresis response. Typically this is done in the form of annealing by the supplier during the manufacturing process. Annealing is applied to the ferromagnetic material in order to soften the material and reduce the saturation induction and coercive force. This essentially produces a narrower hysteresis loop. If heat treatment is applied to harden the material then comparably the hysteresis loop will be wider. Materials should be tested in final configuration such that the desired hysteresis loop is confirmed.

## 4.2.2.   Volume of Hysteresis Rods

The following two equations provide the required volume of material that should be present on-board the spacecraft such that a reduction of spin occurs in a define period of time. The estimate does not compensate for magnetic dipole that could be present on-board the spacecraft from other sources. Typically the performance will be lower than the calculated estimate.

The relationship between spacecraft rotation and energy absorbed by spacecraft can be
defined by the following approximation (4.2):

$$B \frac{d\omega}{dt} = -\frac{1}{2\pi} (\oint H dB)$$

(4.2)

Rewriting the above and introducing initial angular rotation we get equation (4.3):

$$\omega(t) = \omega(0) - \frac{V_{rod}(\oint H dB)}{2\pi B} t$$

(4.3)

where $\omega(0)$ = The initial angular speed of spacecraft about an axis

$\omega(t)$ = The final angular speed of spacecraft about an axis

$V_{rod}$ = The estimated volume of rod that will be used on the spacecraft

$\oint H dB$ = The surface area on the B-H curve which can be estimated from a
mathematical model or actual measured B-H curve of material at the
expected magnetic field strength $(H)$

$B$ = The magnetic flux density of the hysteresis rod at the magnetic field
strength input $(H)$

$t$ = The required spin down time for the spacecraft about an axis.

The equation (4.4) can be rewritten providing the time it takes for the rotational
speed to be damped:

$$t_{fin} = \frac{2\pi B \omega(0)}{V_{rod}(\oint H dB)}$$

(4.4)

It should be noted that a mathematical model developed by NASA (N95-27801) can be
used to predict the hysteresis $B - H$ curve [28].  This model was developed as a
function of the material data that was supplied to NASA and is an approximation to
that data (hysteresis $B - H$ curve).  The inputs into the model are the parameters
shown in Figure 4-2.  Sample output of this model can be seen in Figure 4-3.
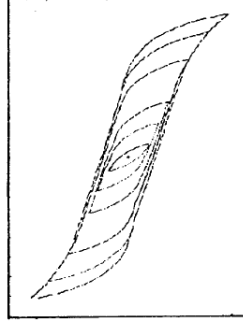
Figure 4-3: NASA- Magnetic Hysteresis Model Ouput [28]

## 4.2.3.   Arrangement on Spacecraft Bus

The arrangement of the hysteresis rods on the spacecraft must meet a number of conditions which ensure the maximum damping can be attained from the rods. These conditions are as follows:

a) The rods must be arranged in relation to the permanent magnet such that they are in plane that is perpendicular to the axis of the permanent magnet and pass through its centre, refer to Figure 4-4

b) Through experimental results it has been shown that the identical rods in a parallel configuration should be separated by $30 - 40\%$ of their length as to minimize mutual demagnetization, which lowers the resultant damping produced by the hysteresis rods

c) The influence of the permanent magnet or other sources of dipole must be quantified and related to the performance of the hysteresis rods. The effects of a dipole are quantified through the use of the following equation (4.5):

$$H_{s\tau} = \frac{3msl_t}{4\pi(l^2{}_s + l^2{}_t)^{5/2}} \tag{4.5}$$

where $H_{s\tau}$ = The estimated magnetic field strength at the rod for a spacecraft
  body defined as a cube

$l_s, l_t, s$ = Please refer to Figure 4-4: Calculation of the component $\text{H}_{s\tau}$ of
  vector $\text{H}_s$ along the hysteresis rod displacement from the plane P

$m$ = The magnetic dipole of the permanent magnet.
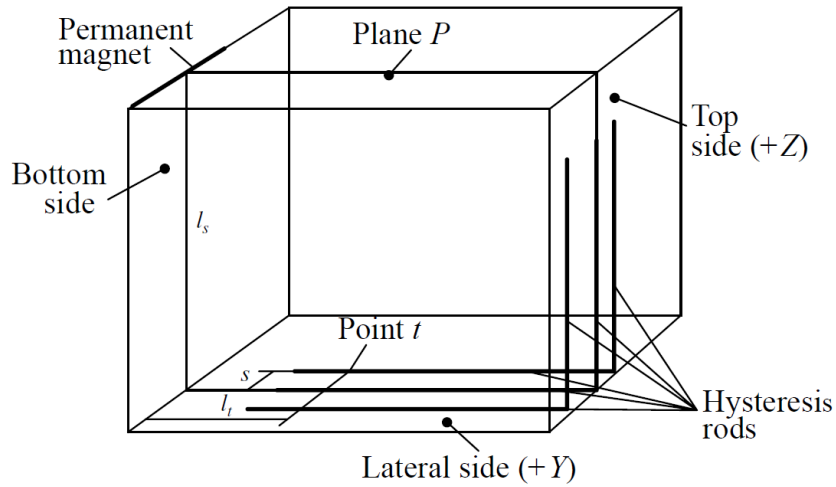
Figure 4-4: Calculation of the component $H_{s\tau}$ of vector $H_s$ along the hysteresis rod displacement from the plane $P$ [26]

The arrangement of the hysteresis rods on the Munin spacecraft can be seen in Figure 4-4 with the generalized distribution and position is shown. The arrangement in the NTS spacecraft can be seen in Figure 4-5.
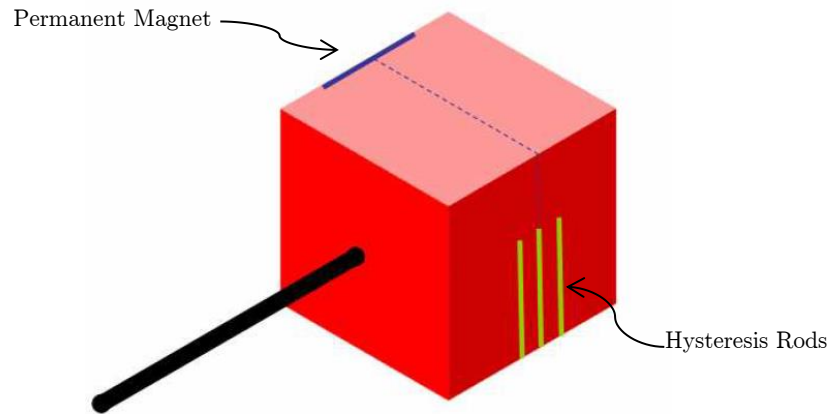


Figure 4-5: NTS Attitude Subsystem Component Placement [27]

## 4.2.4.   Elongation (L/D)

The geometry of the hysteresis rod is an iterative process between this Section 4.2.4 and Section 4.2.3. The rod size is constrained by the availability of space and arrangement of rods on spacecraft. At this point of the design process the material and volume for the hysteresis has already been determined in Sections 4.2.1 and 4.2.2.

The typical optimal range for hysteresis rod elongation ($p$) is $200 - 300$. The elongation that was used on NTS was $\sim24$ and the elongation that was used on Munin was $\sim155$. Coefficient of demagnetization can be determined through the following approximation (4.6):

$$N = \frac{\ln(1.2p - 1)}{p^2} \tag{4.6}$$

where $N =$ Demagnetization coefficient

$\quad$ $p =$ Elongation parameter defined as length/diameter.

The magnetic permeability of the rod $\mu_r$ is dependent on the material permeability $\mu$ through the following approximation (4.7):

$$\mu_r = \frac{\mu}{(1 + N\mu)} \tag{4.7}$$

The above equation shows that the change in rod permeability as a function of material permeability can be reduced by adjusting the elongation parameter. Since the variation of rod material permeability ($\mu$) as a function of its length is small, the mean of the rod permeability ($\mu_r$) can be used instead. This provides an approximation of a constant permeability that can be used for a hysteresis rod.

## 4.2.5. Verification of Design

The verification of the hysteresis rod design process is divided into two phases. The first phase is the simulation of the spin down performance. The second phase is the simulation of steady state behaviour. Typically this can result in adjustments in hysteresis rod design given the simulation results.

In more detail the spin down behaviour is simulated using the developed spacecraft equations of motion which should capture the following hysteresis rod parameters:

- Constant magnetic permeability derived in Section 4.2.4
- Parasitic magnetic field strength that exists in spacecraft body from Section 4.2.3 c), also becomes the magnetic field bias that the rod will be exposed to
- Magnetic field strength input from a geomagnetic field model

The steady state behaviour simulation shows the minimum response that the hysteresis rods will provide in terms of damping. This simulation must account for the following:

- Constant magnetic permeability derived in Section 4.2.4

- Parasitic magnetic field strength that exists in spacecraft body from Section 4.2.3 c), this provides an offset bias that the rods will be exposed to

- Residual spacecraft rotation and the resultant change in field strength input from a geomagnetic model

- Comparison between the field strength input and coercive force of rod material *shows the limiting hysteresis loop* which provides insight into the steady state behaviour of the spacecraft

- Magnetic field strength input from a geomagnetic field model

Hysteresis rods may go through further redesign pending on whether the results of this section satisfy spacecraft top down requirements.

## 4.3   Hysteresis Rod Acceptance Testing

The current acceptance test plan of hysteresis rods consists of confirmation that the hysteresis rods are showing a hysteresis phase lag and that a resultant magnetic field flux is being generated as shown by a hysteresis response. This acceptance test is not mission requirement driven. The phase lag is verified through the results shown in Figure 4-6, showing the input signal and the lagging output signal which is a function of the magnetic flux density generated by the hysteresis rod.
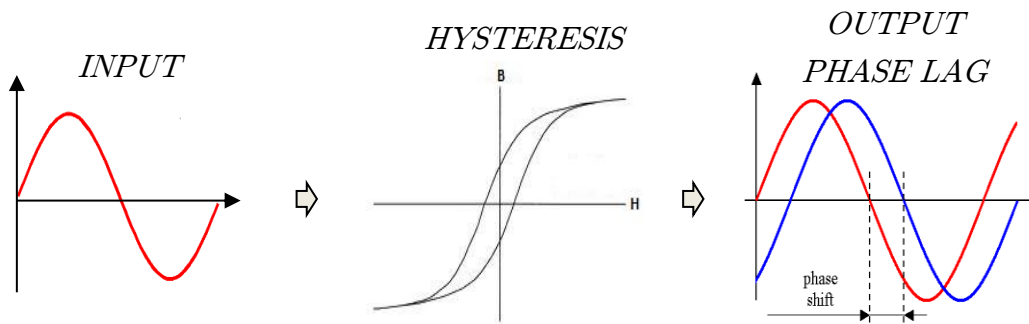


Figure 4-6: Hysteresis Phase Lag

The resultant magnetic field flux is then confirmed as a function of position along rod. These results are shown in Figure 4-7, where a confirmation is made that the response is similar from rod to rod and that the maximum response is in the middle of the rod and minimum at the extremities.
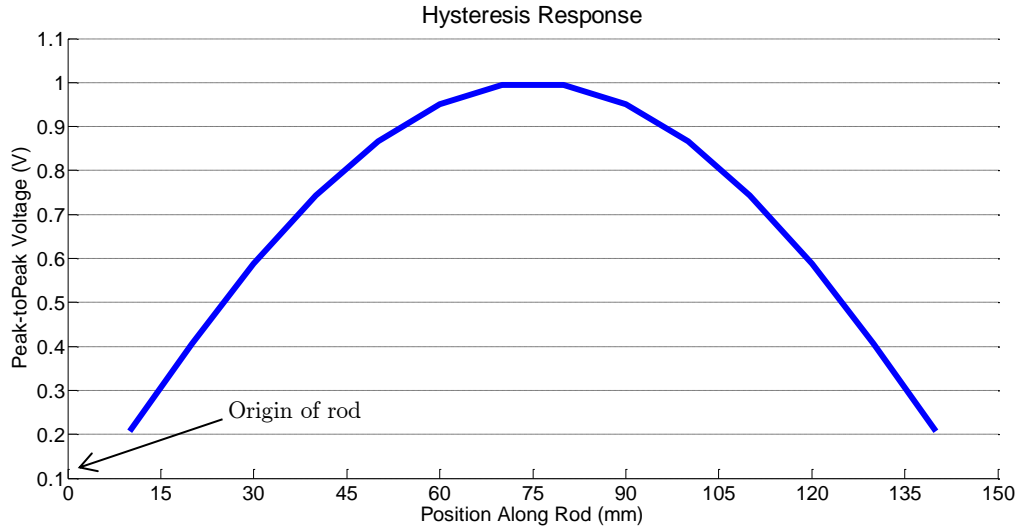


Figure 4-7: Hysteresis Response - Position along Rod

## 4.3.1.   Acceptance Testing - Test Fixture

The test fixture provides the capability of immersing the hysteresis rod in a chosen magnetic field strength and then measuring the magnetic flux density through a sensing coil. The fixture can be seen in Figure 4-8, where the use of Coil-1 is for the magnetic field strength input and Coil-2 is a sensing coil for the magnetic flux density feedback.

The operation of the fixture begins with insertion of the hysteresis rod into Coil-1. The magnetic field strength input to Coil-1 is then adjusted using the provided potentiometers. During the adjustment process a multimeter can provide a measure of the current to the coil which is directly proportional to the magnetic field strength input.

The Coil-2 or sensing coil is then used to measure the magnetic flux density. The coil provides its feedback in terms of voltage. The sensing coil can then be moved across the length of the rod in Coil-1 to measure the voltage response as a function of position along rod as described by Figure 4-7. The phase lag measurement is taken at a particular position along rod and it is the lag between Coil-1 and Coil-2 signal. Typically an oscilloscope is used to simultaneously display the voltage response and

phase lag during testing. Expected sensing voltage at a magnetic field strength is a function of material properties and hysteresis rod design.
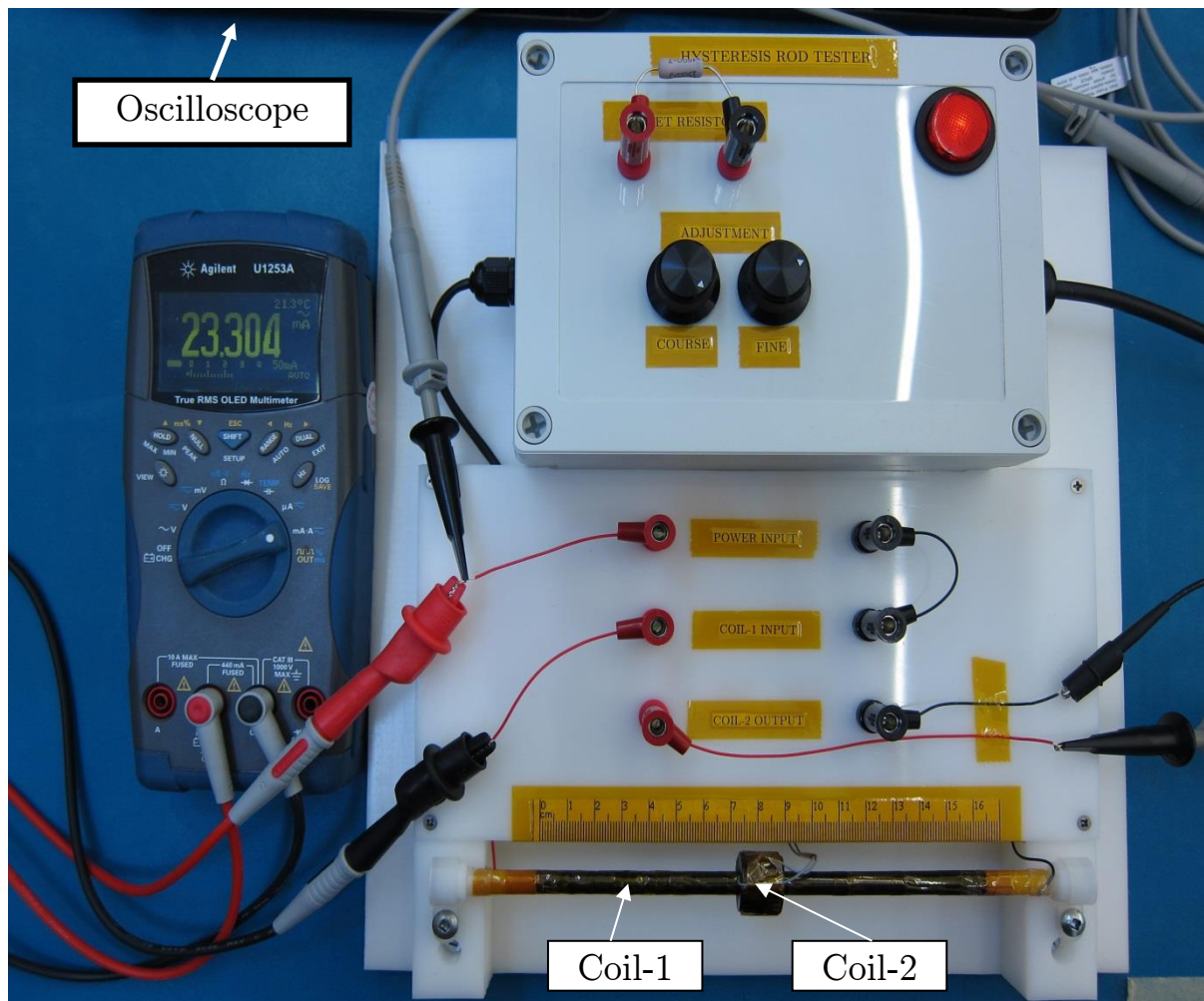


Figure 4-8: Hysteresis Rod Test Fixture

## 4.3.2.   Acceptance Test Plan

As mentioned earlier the acceptance test plan is not mission requirement driven, it is simply a verification of hysteresis response as a function of position along rod and phase lag. The testing is comprised of setting a magnetic field strength input in increments up to material saturation. A sample test plan is provided in Table 4-5. Each test is broken down to voltage and phase lag measurements at positions along rod. These positions are a function of rod length and sensing coil size.

Table 4-5: Hysteresis Rod Test Plan

| HYSTERESIS ROD TEST PLAN | | | | | | |
|---|---|---|---|---|---|---|
| Test | $V_{coil-1}$ (VAC) | $i_{coil-1}$ (A) | $H_{coil-1}$ (A/m) | $B_{coil-1}$ (mT) | Noise ($V_{Pk-Pk}$) | Verified |
| A | 0.3 | 0.0024 | 26.92 | 33.8 | 0.032 | YES |
| B | 0.5 | 0.0039 | 44.86 | 56.3 | 0.032 | YES |
| C | 1 | 0.0078 | 89.73 | 113 | 0.032 | YES |
| D | 2 | 0.0157 | 179.45 | 225 | 0.032 | YES |
| E | 5 | 0.0392 | 448.63 | 563 | 0.032 | YES |
| F | 10 | 0.0784 | 897.25 | 1130 | 0.032 | YES |

### 4.3.3. Acceptance Test Results

The acceptance test was completed for 12 hysteresis rods using the described test fixture. The expected result for sensing voltage at rod centre and material saturation is at least $32VAC$, with a minimum at the extremities of the plot, while the phase lag response was expected to be between $130º$ to $150º$ as the position along the rod changes.



Figure 4-9: Phase Lag for $90\ A/m$ Magnetic Field Strength

The result for phase lag of a rod at a magnetic field strength input of $90\ A/m$ can be seen in Figure 4-9. This is a valid response showing lag of the green wave corresponding to Coil-2 behind the blue waveform which is Coil-1. The irregularities seen at the peaks of the green waveform are a function of nonlinearities and are washed away as the input approaches material saturation. The following are some of the sources of non-linearity:

- Magnetic permeability
    - Type of material
    - As a function of magnetic field strength input
- Geometry of rod
    - Elongation (L≫D)
    - Volume
- Manufacturing process
    - Heat treatment
    - Cutting process
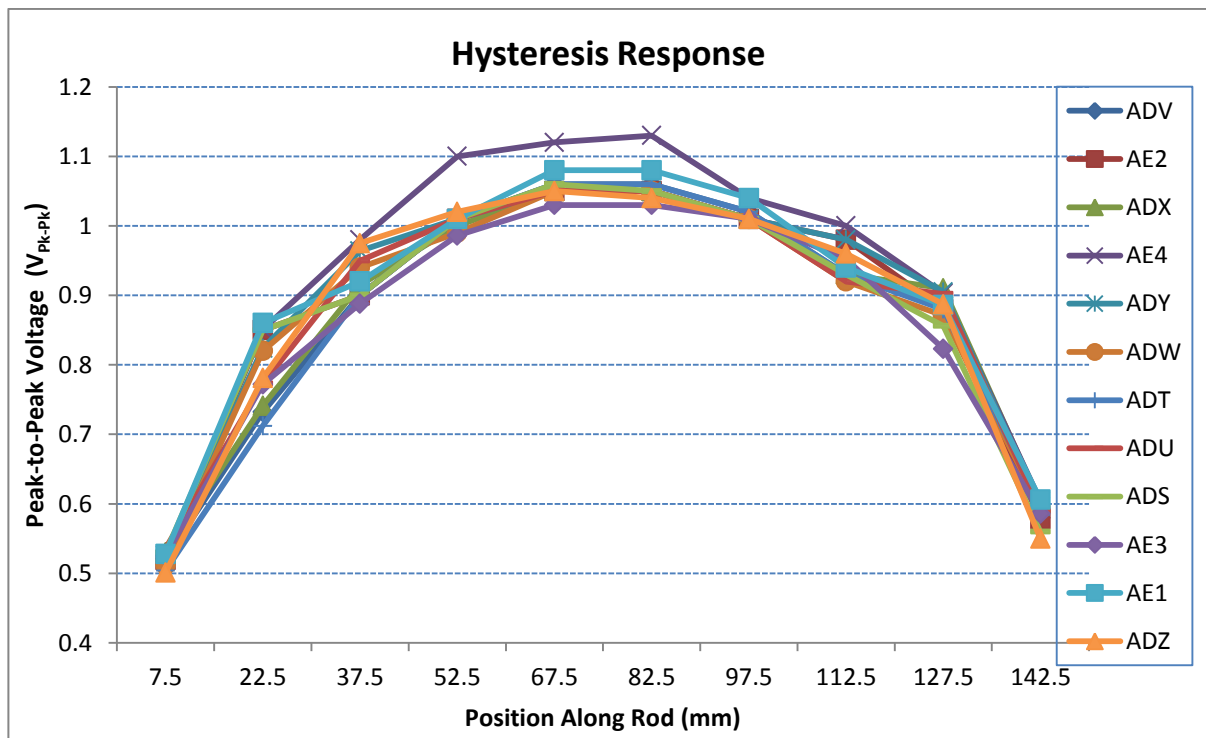


Figure 4-10: Hysteresis Response for $90\ A/m$ Magnetic Field Strength

The hysteresis response from sensing Coil-2 at a magnetic field strength input of
90 $A/m$ can be seen in Figure 4-10. The legend identifies the 12 hysteresis rods being
tested with corresponding serial number names. Each plot on this Figure corresponds
to a particular hysteresis rod. This is a valid response with all 12 hysteresis rods
showing a similar concave down response with a peak of just over $1VAC$. It is very
important to understand that hysteresis is a very complex behaviour which is
influenced by the non-linearities mentioned earlier. The response that is measured
here is not only the voltage but also the overall visual plot which must be concave
down and relatively similar between rods of the same design.
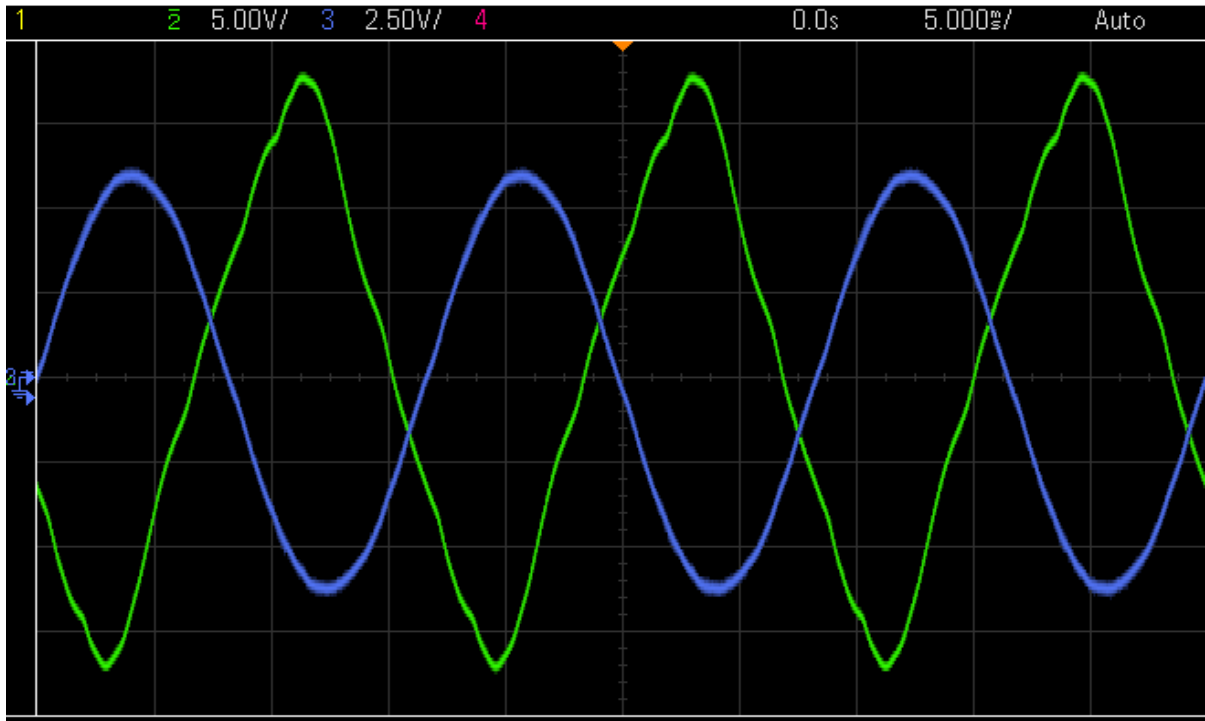


Figure 4-11: Phase Lag for for 900 $A/m$ Magnetic Field Strength

The phase lag for a field strength input at material saturation is shown in Figure 4-11.
This result has shown the output (green) lagging behind input (blue) at a phase
difference of between 130º to 150º which makes it a valid result. The irregularities on
the output signal (green) are washed out due to the material being at magnetic field
strength saturation.

Again at saturation the hysteresis response for the rods is shown in Figure 4-12. The results are valid with a concave down response and a centre peak voltage of at least $32VAC$.
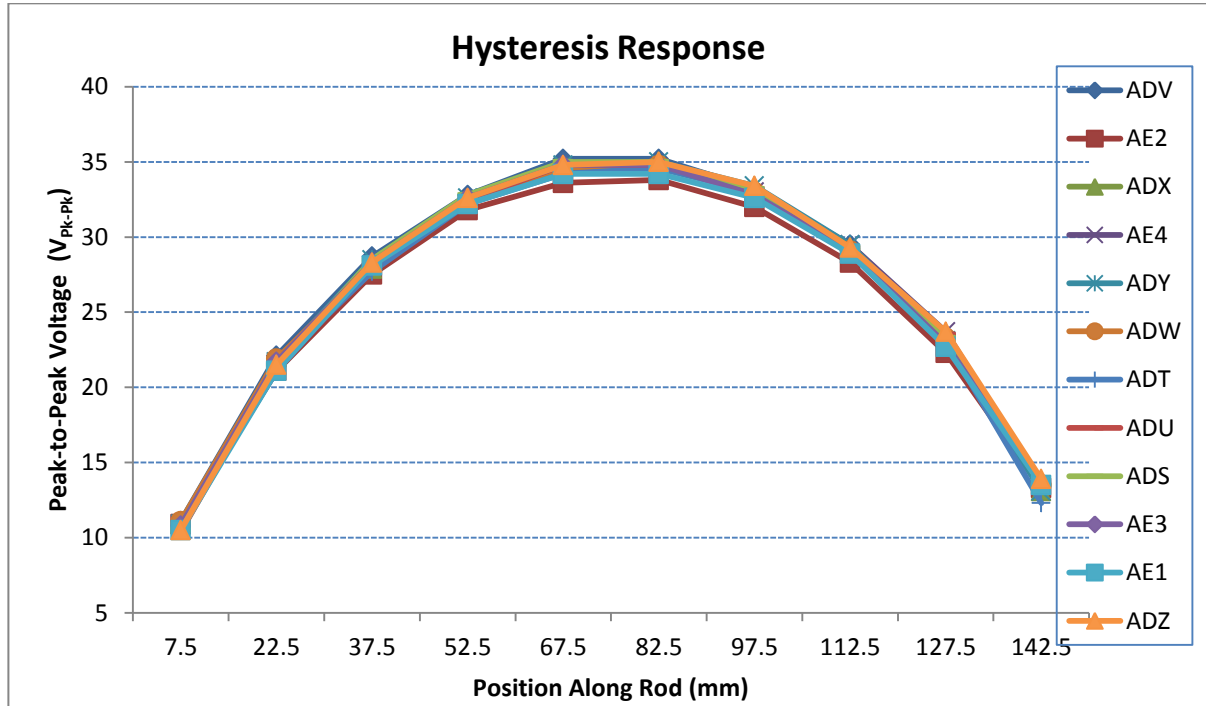


Figure 4-12: Hysteresis Response for $900\ A/m$ Magnetic Field Strength

## 4.4  Summary of Contribution

The hysteresis rod exhibits very complex behaviour which requires iteration of design to meet spacecraft requirements and careful interpretation of results during acceptance testing. The author's contribution is comprised of the following:

- Outline of hysteresis rod design for a spacecraft bus
- Hysteresis rod test fixture design and implementation
- Acceptance test plan for hysteresis rods
- Acceptance testing of $12$ hysteresis rods

## 4.5  Future Work

The current acceptance test plan only ensures that the hysteresis rods in question are of a ferromagnetic material given the phase lag and hysteresis response as a function of

position along rod. A more complete analysis would be to generate the actual $B - H$ plot as shown in Figure 4-2. The reason for this is as per equation (4.2) the energy that is absorbed from the spacecraft is a function of the area under the $B - H$ curve. Hence it would be beneficial to verify that the hysteresis rod $B - H$ curve meets the minimum energy absorption requirement. It is important to understand that variations in the $B - H$ plot can also be introduced from many sources including during the manufacturing process as an example. These variations would not be detectable using the current acceptance test plan. The developed test fixture can generate a $B - H$ curve as shown on Figure 4-13, which can provide the energy absorbed by the hysteresis rod. Work still needs to be completed in terms of calibration of the hysteresis test fixture for the $B - H$ plot generation such that the area under the curve has been validated.
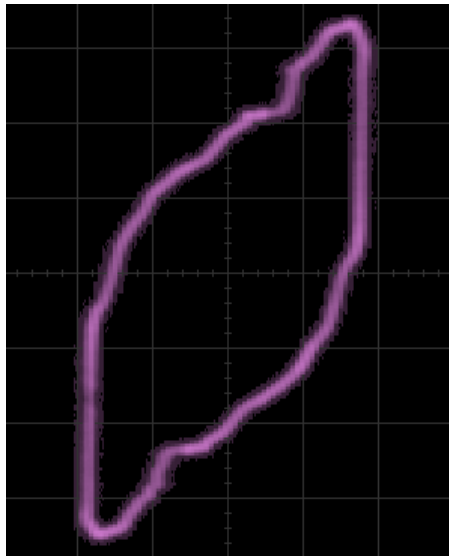


Figure 4-13: B-H Plot for Hysteresis Rod

# Chapter 5

# Attitude Hardware Emulator

The purpose of the Attitude Hardware Emulator (AHE) is to replace the need for spare attitude hardware which is a significant extra cost to nanosatellite missions. This chapter describes the emulation of attitude hardware in software with emphasis on the reaction wheel actuator and fine sun sensor. In order for the emulation to be representative of actual hardware a number of requirements must be met. These include major software states such as a bootloader and application mode. Finally the emulator must be capable of running multiple instances of the emulated hardware within a specified level of performance.

## 5.1 Requirements

The requirements for the Attitude Hardware Emulator are as follows:

- [AHE-1] Software must use Nanosatellite Protocol (NSP) for emulated hardware communication

- [AHE-2] The emulated hardware must have two software states: a bootloader and application state

- [AHE-3] Each software state must use the hardware model as a source for NSP device parameters

- [AHE-4] Up to 6 instances of an emulated hardware device must be able to operate on the same serial interface

- [AHE-5] Emulated device performance must be confirmed against experimental results

- [AHE-6] The emulator must be able to sustain communication performance of 20 *packets per second* from each instance of emulated hardware

## 5.2    Nanosatellite Communication Protocol

The Nanosatellite Protocol (NSP) provides a standardized method for device communication on-board the spacecraft.  The devices which use this protocol could consist of attitude hardware, payload and communication system just to name a few. Two important aspects of this protocol are packet integrity and communication topology, which ensure proper operation [29].

The packet integrity checks for the NSP protocol can be further broken down into Cyclic-Redundancy Check (CRC) and KISS framing, where the CRC check provides error detection within the data carried by the packet, and KISS framing is a method of adding beginning and end frames to each packet such that the start and end of packet can be detected.  If a CRC error or missing KISS framing is detected then a typical device with NSP implementation will not acknowledge the packet as good transmission and may request the same packet again.

The communication topology that allows multiple devices to communicate on the same bus uses the master-slave concept.  This is not a new concept and has previously been implemented in a number of standard communication technologies such as RS485, RS232, CAN-Bus and SPI just to name a few.  The concept works on the principle where the master is the only device that can send requests or 'speak' on the communication bus and the slave is one of many devices which will reply to a request or only 'speak' when spoken to.  Hence, only the master can initiate communications at any time while all slave devices are listening.  This ensures that the communication state of all devices that are spoken to is passive in nature and will not inhibit the operation of the master device.  The Figure 5-1 shows a typical master/slave configuration with the outlined portion that is the focus of the emulator.
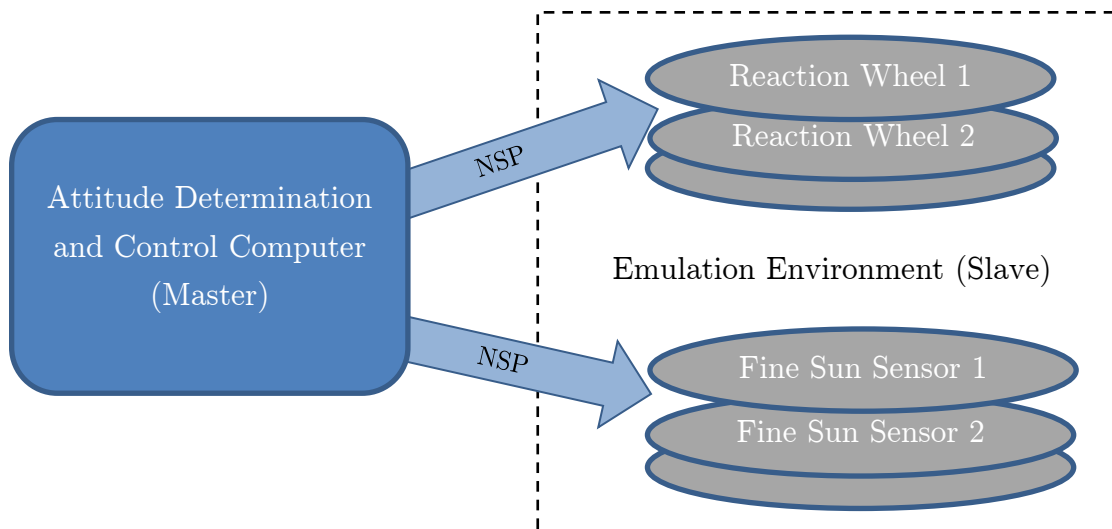


Figure 5-1: Hardware Emulation NSP Topology

## 5.3    Software States

The attitude control and determination hardware is divided into two main categories the sensors and actuators.  Both types of hardware have two fundamental software states the bootloader and application mode.  In bootloader and using the NSP protocol the hardware can provide basic functionality which includes activating the application mode, loading new application code, checking parameters and reading and writing directly to a memory address.  The application mode which can only be invoked from the bootloader mode provides complete device functionality.  Hence, it is important for the purposes of the attitude hardware emulator to distinguish between the two modes and establish how these interact in the emulation environment.

### 5.3.1.    Bootloader Mode

The bootloader mode is the most basic state that an attitude actuator or sensor can be in.  This mode is the only state that is automatically invoked post power up of device. This basic state does provide the NSP based interface but without any device functionality.  The typical interface is limited to the following:

1. Using NSP as a communication protocol
2. Loading new application code
3. Reading and writing to specific memory locations in the device
4. Performing checks of the onboard microprocessor
5. Polling telemetry that was saved while the device was in application mode
6. Limitation of not being able to operate the device without entering the application mode
7. Invoking the application mode

The implementation of the bootloader in software for a particular device consisted of items 1, 6 and 7 from above.  This is since items 2, 3, 4 and 5 are used for troubleshooting of the device which is not necessary in software emulation due to the ability to view the state of the device through the emulator.  It should be clarified at this point that the emulation environment mimics the behaviour of the device for the spacecraft FlatSat as discussed in Chapter 1, and does not provide exact emulation of the device hardware which is not necessary.

## 5.3.2.   Application Mode

The application mode is the only mode that provides full device functionality which is typically described in the Interface Control Document (ICD) for a particular device. This mode can only be entered from the bootloader mode and upon an application mode exit command it always returns to the bootloader mode. The device uses an implementation of NSP protocol for all communication. For the hardware emulator this means that the application mode must mimic the behaviour of the actual attitude hardware in application mode.

The emulation of hardware while in application mode consists of two major items, the NSP interface and the hardware model in software. The NSP interface implementation in terms of the response of the device to commands is provided at a high level, where the details of which can be obtained from the ICD for the device and are beyond the scope of this chapter. The types of application mode commands that are available are shown in Table 5-1.

Table 5-1: Device Mode Commands

| Type of Command | Typical Command | Effect of Command | Notes |
| --- | --- | --- | --- |
| Telecommand | 0x00001000 send to device | Device enters application mode | Only works in bootloader mode |
| Mode Commands | Mode: 0x16 with value of 0.02 | Commands a reaction wheel to enter torque control mode and apply a positive torque of 0.02 Nm | A list of commands are available in the Interface Control Document (ICD) for a specific device |
| Parameter Commands | Parameter: 0x14 with value of 0.1 | Commands a change in parameter 0x14 to a new value of 0.1 | |
| Mode Telemetry | 0x00 | The reply from the device contains the current mode type and value | |
| Parameter Telemetry | 0x14 | Returns the value that is stored by parameter 0x14 | |

The reaction wheel and the fine sensor each have a variety of available commands in each type of listed command category. The implementation of the NSP interface accounts for the command categories but does not implement the details of the number of available commands. This is accomplished by polling the commands directly from the software model of the device.

## 5.4 Hardware Modelling

The attitude hardware that is modelled in software consists of the reaction wheel actuator and the fine sun sensor. Both devices use a combination of a mathematical model and a characterization map to provide an appropriate response of the device in software.

### 5.4.1. Reaction Wheel Model

The reaction wheel actuator is modelled using mathematical relationships, characterization map and a software integral control loop. Each is described in more detail with emphasis on software implementation. The work in this section is based on previous work described in Chapter 3, where the characterization of the reaction wheel actuator is described.

The behaviour of the reaction wheel actuator is described by the equation (5.1), where the net torque $T_a$ is a function of the duty cycle $X_{dc}$, internal torque $T_g$ and opposing torque $T_m$. The net torque is shown by:

$$T_a = X_{dc}T_g - T_m \qquad (5.1)$$

The relationship of internal and opposing torque and motor parameters is described in Chapter 3. The duty cycle pertains to the amount of voltage being applied to the drive stages at a particular internal torque. In Chapter 3 this was assumed to be constant since the reaction wheel was always commanded at a constant torque. In this section, it is important to capture the variation in duty cycle since with variation of spacecraft bus voltage the applied voltage at the windings will change and affect reaction wheel performance as per equation (3.5), (3.6), (3.7) and (3.10) [19]. The equation (5.2) uses the characterization map of the DC motor performance in Chapter 3 as a lookup table to derive the power, torque, speed, current and voltage limitations. The stall torque is $T_{gs}$, $\alpha$ is a value of $r$ for which the internal torque $T_g$ has a maximum magnitude, $r$ is a speed based parameter as described in equation (5.2) as a

function of duty cycle, $\omega$ is the angular speed of the motor and $\omega_{NL}$ is the maximum speed at zero torque of the motor. The stall torque is described by:

$$T_g = 2T_{gs}\alpha r(\alpha^2 + r^2)^{-1}$$

$$r = 1 - \frac{\omega}{\omega_{NL}} \; for \; X_{dc} > 0$$

$$r = 1 + \frac{\omega}{\omega_{NL}} \; for \; X_{dc} < 0$$

(5.2)

The opposing friction component of the torque is described in equation (5.3). This equation is similar to the equation (3.13), the only difference being the friction component is being written in an explicit form. Where as an example for the RW0.06 reaction wheel the coulomb friction component $T_c$ is $1\,mNm$ and the viscous friction coefficient $f$ is $4\,\mu Nm/(rad/s)$. The opposing friction torque is described by:

$$T_m = T_c sgn(\omega) + f\omega$$

(5.3)

In software the described equations provide the method of coupling the integral control loop and the characterization map. For a given requested angular acceleration and assuming a rotor mass moment of inertia the software assumes that a torque is being requested. This torque is then propagated forward in time using an integral loop which is limited by the characterization map of the device. The map provides the torque, speed, voltage, current and disturbance limitations that are imposed on the integral control loop. This is accomplished by not only limiting the behaviour of the loop but also injecting the disturbances into the loop. These could be poor speed estimates, voltage changes due to bus voltage variation or other parameters which are captured by the characterization map. A high level block diagram of the implemented control behaviour between mathematical model, characterization and integral loop can be seen in Figure 5-2.
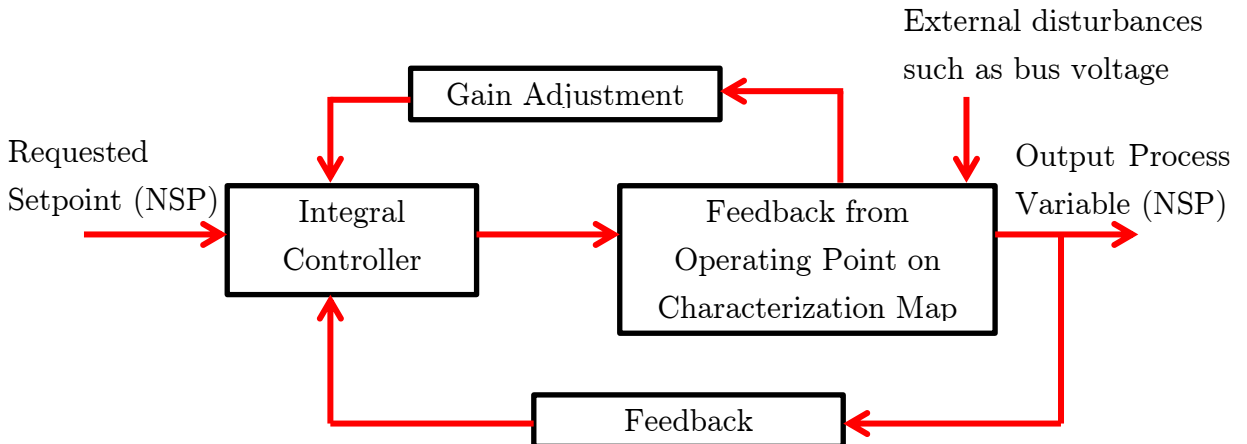


Figure 5-2: Block Diagram of Reaction Wheel Model in Software

## 5.4.2.   Fine Sun Sensor Model

The fine sun sensor is a device that is part of the attitude determination system on board the spacecraft. It is capable of providing spacecraft orientation in reference to the sun line. The sensor is limited to a two dimensional solution and is unable to provide the orientation of the spacecraft about the sun line. The device uses a complementary metal-oxide-semiconductor array (CMOS) for sensing the sun line and a microcontroller for post processing the data and detecting the centre of the ellipsoid generated by the sun line on the CMOS [30]. The modelling of the device is accomplished using a combination of the processing code that is used on-board the sensor to mimic the centre of ellipsoid determination and the characterization map which provides the CMOS response as a function of sensor orientation with respect to the sun line. Figure 5-3 provides a summary of the model.
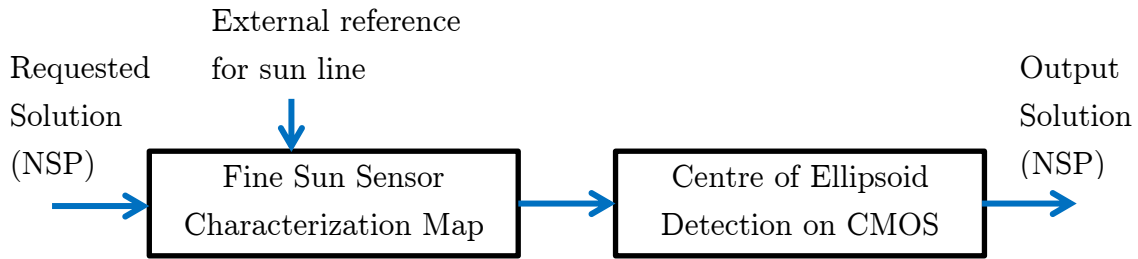


Figure 5-3: Block Diagram of Fine Sun Sensor Model in Software

The model works on the foundation described in Section 5.3 where the NSP protocol is used as the interface to the model. Given an NSP request the model will poll an external sun line reference to determine where on the CMOS the ellipsoid will be generated. The cross referencing of the sun line orientation with respect to the sensor and the characterization map are both generated during acceptance testing of the device and are beyond the scope of this thesis [30]. Figure 5-4 represents the generated characterization of the sensor CMOS at angles of incidence to the sun line. Pointing accuracy is shown as a variation of colour from red (low accuracy) to blue (high accuracy). This map is used as a look-up table for a given sun line reference where the accuracy and ellipsoid position are determined. The centre of the ellipsoid is then calculated using the method employed on the sensor. Finally the output solution is sent as a reply to the original NSP request.
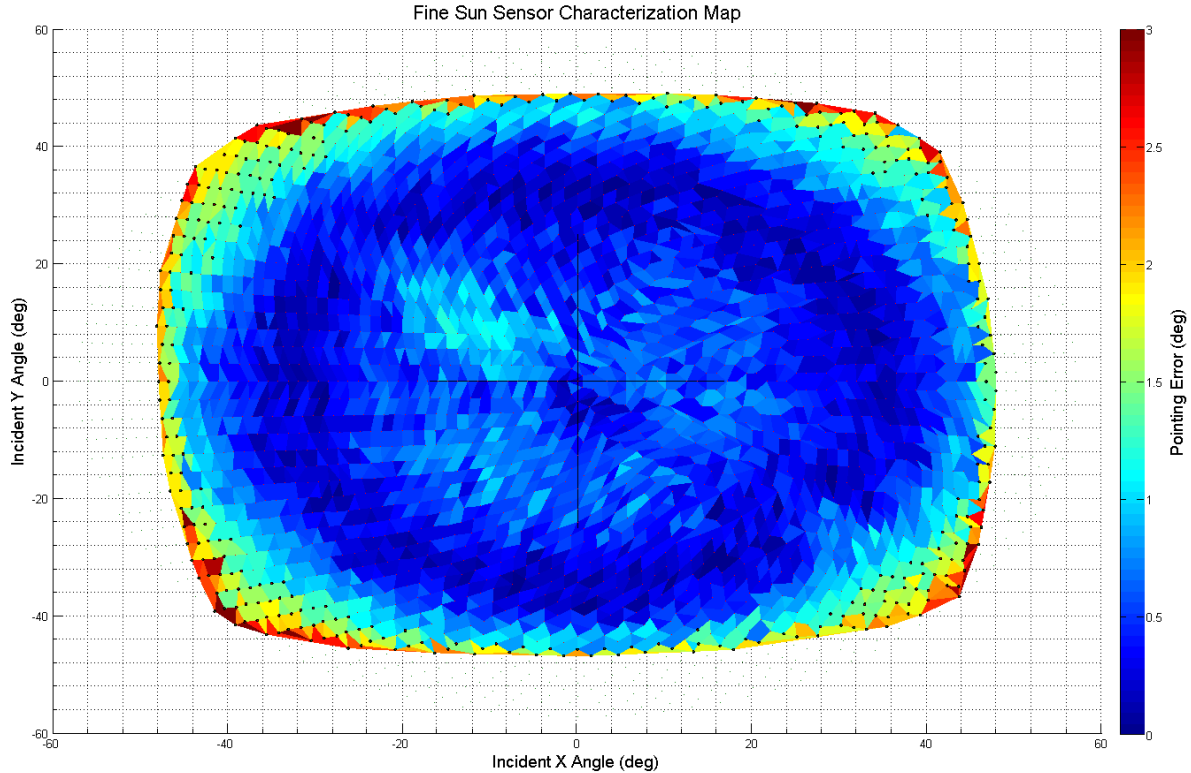
Figure 5-4: Fine Sun Sensor Characterization Map

## 5.5 Emulator Performance

At the time of writing this thesis the attitude hardware emulator performance had only been verified for the NSP Section 5.3 software states and not the hardware models in software. The verification of the NSP protocol entailed CRC, KISS and packets per second tests. The results of which had verified requirements AHE-1, AHE-2, AHE-3 and AHE-6. The detailed verification of these requirements was accomplished through the implementation of the sections described earlier in this chapter. The critical requirement AHE-4 and AHE-5 which ensures that the emulated hardware behaviour has been confirmed against experimental results had not been verified at the time of writing this thesis.

## 5.6 System Overview

The complete system topology is comprised of the attitude determination and control computer, external reference source containing items common to all systems involved such as orbit data and attitude hardware emulator and the emulator environment. The Figure 5-5 shows a high-level overview of the system.
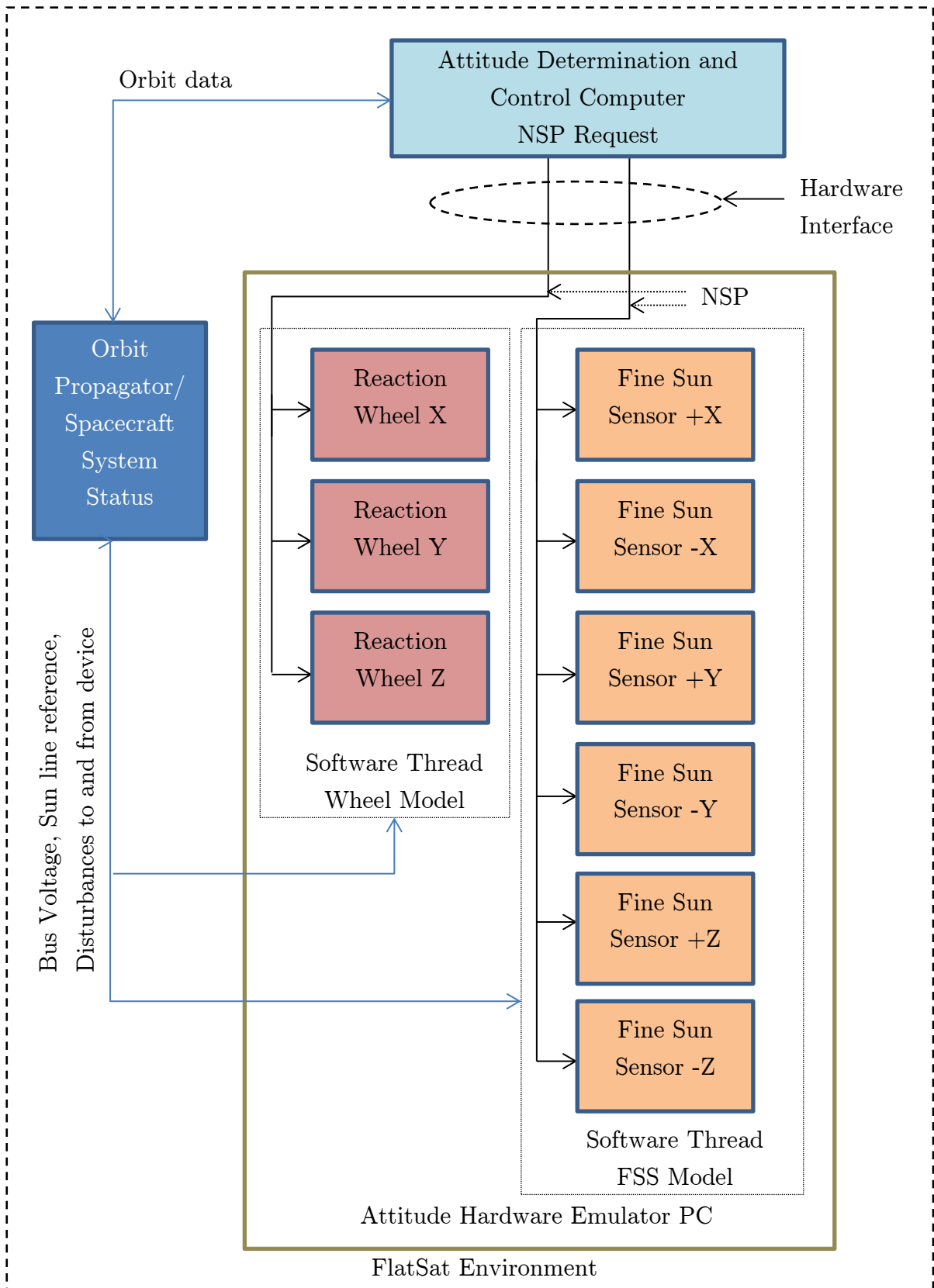
Figure 5-5: Simplified Attitude Hardware Emulator Block Diagram

## 5.7   Future Work

The work on the attitude hardware emulator thus far has verified all requirements except for the verification of model performance and operating multiple instances of the hardware models at an appropriate communication performance. It is foreseen that once the final requirements are verified this type of emulation environment will be extended to other attitude hardware. Other hardware may include magnetorquers, hysteresis rods, rate sensors, magnetometers and star trackers. This would provide for a complete emulation environment for a FlatSat setup as discussed in Chapter 1.

# Chapter 6

# Conclusions

This thesis has detailed the analysis, verification and emulation of attitude hardware for a nanosatellite scale of spacecraft. The characterization of attitude control hardware has been completed through detailed analysis and verification of performance. The results of which have been incorporated into acceptance test plans that inherently build on heritage. The test plans had been used in verification of the attitude control system requirements, which showed acceptable performance for all hardware tested. The data obtained during testing further provided input into software models which were implemented in the attitude hardware emulator. At the time of writing this thesis a number of spacecraft missions await launch that incorporated the work described herein.

The attitude control hardware that had been characterized included the reaction wheel and hysteresis rods. The characterization came as a consequence of more stringent requirements to which some of the devices had not been previously tested to. Hence, the characterization provided for a performance map of the device beyond previously tested limits. The performance had initially been established using theoretical assumptions overlaid with previously collected data, which was verified through careful testing. Both actuators acceptance tests had been modified providing an overall improvement.

The reaction wheel actuator was characterized using a single phase DC motor model with a friction model that was based on past run down data. This led to a number of discoveries when the theoretical performance prediction was confirmed experimentally. These included regenerative zones, high torque jitter zones and large torque overshoot in zero crossings both for the RW0.03 and RW0.06 reaction wheels.

The regenerative behaviour was mitigated through the use of a dummy load resistor for acceptance testing and it was also verified that the spacecraft power system can handle the regeneration.  Two software changes had been requested, first to remove or modify the software regenerative control as to reduce the torque jitter in regenerative zones and second to develop a better speed estimator at zero crossing to minimize torque overshoot.  Overall the characterization map provided areas of best performance based on which the acceptance testing was revised such that the requirements were met.  In total $25$ reaction wheels were tested meeting requirements. The testing exhibited inherent limitations which were due to taking measurements that were internal to the device and not actually measuring the physical torque jitter output of the device which is the next logical step in future testing.

The hysteresis rod acceptance testing had not been previously established at the Space Flight Laboratory.  Hence the work completed was a design process for hysteresis rods in order to develop an acceptance test such that the necessary requirements are captured. As per requirements and due to flight heritage the acceptance test had to meet two criteria which included the voltage response as a function of the length of the rod and phase lag.  In total $12$ hysteresis rods were tested and verified against the requirements.  The testing also showed that future improvements could be made mapping out the $B - H$ curve for the rod using the developed test fixture.  This could provide for an estimate of the amount of energy the hysteresis rod would absorb from one $B - H$ cycle.

The test results from characterization of the reaction wheel and a fine sun sensor had been used to develop emulation of these devices in software.  This is in an effort to reduce cost and provide an invaluable resource for ground testing.  For both devices the characterization maps were used from acceptance testing in conjunction with mathematical models that pertained to the specific performance behaviours.  At the time of writing this thesis some of the requirements had been verified and some were left to be verified at the completion of the emulation software.

The work presented in this thesis has provided an in-depth insight into the behaviour of attitude control hardware, acceptance testing and software emulation. The linkage to how crucial this is for the success of nanosatellite scale spacecraft is obvious as presented in this thesis.  Given the growing demand for these types of missions this is an area of ongoing development and research which ensures present and future mission success.

# Bibliography

[1] Herbert J. Kramer and Arthur P. Cracknell, "An overview of small satellites in remote sensing," University of Dundee, Dundee, 2008.

[2] Najmus. Ibrahim, "NEMO-AM Attitude Determination and Control Subsystem Design and Analysis," University of Toronto Institute for Aerospace Studies, Toronto, 2011.

[3] Jesse K. Eyer, Benoit P. Larouche, Robert E. Zee. Nathan G. Orr, "Precision Formation Flight: The CanX-4 and 5 dual Nanosatellite Mission," University of Toronto Institute for Aerospace Studies - Space Flight Laboratory, Toronto, 2008.

[4] W. W. Weiss, A.F.J. Moffat, R.E. Zee, S.M. Rucinski, S.W. Mochnacki, J.M. Matthews, M. Breger, R. Kuschnig, O. Koudelka, P. Orleanski, A. Pamyatnykh, A. Pigulski, C.C. Grant. A. Schwarzenberg-Czerny, "The BRITE Nano-Satellite Constellation Mission," Committee on Space Research, France, 2010.

[5] Pawel. Lukaszynski, "Research Assessment Committee Report #1," University of Toronto Institute for Aerospace Studies, Toronto, 2011.

[6] Larson J. Wiley Wertz R. James, *Space Mission Analysis and Design*, 3rd ed. New York, United States of America: Microcosm Press Inc., 2007.

[7] Michael Greene, "The Attitude Determination and Control System of the Generic Nanosatellite Bus," University of Toronto Institute for Aerospace Studies, Toronto, 2009.

[8] Bryan Johnson-Lemke, "High Performance Attitude Determination and Control for Nanosatellite Missions," University of Toronto Institute for Aerospace Studies, Toronto, 2011.

[9] Karan. Sarda, "Test Plan, Procedure and Results Report on Wheels," University of Toronto Institute of Aerospace Studies, Toronto, 2008.

[10] Christopher J. McNutt, "Modular Nanosatellites – Plug-and-Play (PnP) CubeSat," Air Force Research Laboratory, Kirtland, 2009.

[11] Sven. Krischke, Manfred. Lemke, Norbert. Muncheberg, "Nanosatellites and Micro Systems Technology – Capabilities Limitations and Applciations," Kayser-Threde GmbH, Munich, 1996.

[12] Pascale Ehrenfreund, Antonio J. Ricco, Henry Hertzfeld. Kirk Woellert, "Cubesats: Cost-effective science and technology platforms for emerging and developing nations," Space Policy Institute - The George Washington University, Washington, 2010.

[13] Ke Gong, Di Yang, Junfeng Li. Bingquan Wang, "Fine attitude control by reaction wheels using variable-structure controller," Aerospace Technology Center and Department of Electronic Engineering, Tsinghua University, China, 2003.

[14] F. Landis Markley, "Maximum Torque and Momentum Envelopes for Reaction-Wheel Arrays," NASA Goddard Space Flight Center, Greenbelt, Maryland, 2010.

[15] Oh. Dong-Ik, Cheon. Hwa-Suk, "Precision Measurements of Reaction Wheel Disturbances with Frequency Compensation Process," School of Aerospace and Mechanical Engineering, Hankuk Aviation University, Hwajun, 2005.

[16] C. M. LIAW. M. C. CHOU, "Robust Current and Torque Controls for PMSM Driven Satellite Reaction Wheel," National Tsing Hua University, 2009.

[17] Sinclair Interplanetary(Canada), "NSP Appication Software for Reaction Wheels.," Sinclair Interplanetary, Toronto, 2008.

[18] Peter C. Hughes, *Spacecraft Attitude Dynamics*. US: Dover Publications, 2004.

[19] Wertz R. James, *Spacecraft Attitude Determination and Control*. Boston, London: Kluwer Academic Publishers, 2002.

[20] French R. James Griffin D. Michael, *Space Vehicle Design* , Second Edition ed. Reston, United States : American Institute of Aeronautics and Astronautics Inc., 2004.

[21] Dr. Duane Hanselman, *Brushless Motors: Magnetic Design, Performance, and Control*. Orono: E-Man Press LLC, 2012.

[22] Electro-Craft Corporation, *DC Motors Speed Controls Servo Systems*. New Jersey: Electro-Craft Corporation, 1978.

[23] Bonin Grant, "Power System Design, Analysis, and Power Electronics Implementation," University of Toronto Institute for Aerospace Studies, Toronto, Thesis 2009.

[24] Pawel Lukaszynski, "Research Assessment Committee Report #2," University of Toronto Institute for Aerospace Studies, Toronto, 2012.

[25] Shigemune. Ohkami, Yoshiaki. Tasniwaki, "Experimental and Numerical Analysis of Reaction Wheel Disturbances," *JSME International Journal*, vol. 46, no. 2, 2003.

[26] M. Yu. Ovchinnikov and Penkov V. I., "Passive Magnetic Attitude Control System for the Munin Nanosatellite," *Cosmic Research*, vol. 40, no. 2, pp. 156-170, 2002.

[27] S. Eagleson, "NTS Attitude Subsystem Design Document," University of Toronto Institute for Aerospace Studies, Toronto, 2007.

[28] Thomas W. Flatley and Debra A. Henretty, "A Magnetic Hysteresis Model," NASA, Greenbelt, MD, 1995.

[29] Daniel D. Kekez, "Nanosatellite Protocol (NSP)," University of Toronto Institute for Aerospace Studies, Toronto, Design Document SFL-GNB-OBC-D001, 2012.

[30] Karan. Sarda, "Test Plan, Procedure and Results Report on Sun Sensors," University of Toronto Institute of Aerospace Studies , Toronto, 2008.

[31] Sainz L., Corcoles F. Pedra J., "Harmonic Modeling of Induction Motors.," Department of Electrical Engineering, Barcelona, Spain, 2005.